









Tertiary Lymphoid Tissues Are Microenvironments with Intensive Interactions between Immune Cells and Proinflammatory Parenchymal Cells in Aged Kidneys

Takahisa Yoshikawa ¹, Akiko Oguchi,^{1,2,3} Naoya Toriu,^{1,3} Yuki Sato ¹, Takashi Kobayashi ⁴, Osamu Ogawa,⁴ Hironori Haga ⁵, Satoko Sakurai ⁶, Takuya Yamamoto ^{3,6,7}, Yasuhiro Murakawa ^{2,3,8} and Motoko Yanagita ^{1,3}

Due to the number of contributing authors, the affiliations are listed at the end of this article.

ABSTRACT

Background Ectopic lymphoid structures called tertiary lymphoid tissues (TLTs) develop in several kidney diseases and are associated with poor renal prognosis. However, the mechanisms that expand TLTs and underlie exacerbation of kidney injury remain unclear.

Methods We performed single-nucleus RNA sequencing (snRNA-seq) on aged mouse kidneys with TLTs after ischemia-reperfusion injury. The results were validated using immunostaining, *in situ* hybridization of murine and human kidneys, and *in vitro* experiments.

Results Using snRNA-seq, we identified proinflammatory and profibrotic *Vcam1*⁺ injured proximal tubules (PTs) with NF κ B and IFN-inducible transcription factor activation. VCAM1⁺ PTs were preferentially localized around TLTs and drove inflammation and fibrosis via the production of multiple chemokines or cytokines. Lymphocytes within TLTs expressed *Tnf* and *Ifng* at high levels, which synergistically upregulated VCAM1 and chemokine expression in cultured PT cells. In addition, snRNA-seq also identified proinflammatory and profibrotic fibroblasts, which resided within and outside TLTs, respectively. Proinflammatory fibroblasts exhibited STAT1 activation and various chemokine or cytokine production, including CXCL9/CXCL10 and B cell-activating factor, contributing to lymphocyte recruitment and survival. IFN γ upregulated the expression of these molecules in cultured fibroblasts in a STAT1-dependent manner, indicating potential bidirectional interactions between IFN γ -producing CXCR3⁺ T cells and proinflammatory fibroblasts within TLTs. The cellular and molecular components described in this study were confirmed in human kidneys with TLTs.

Conclusions These findings suggest that TLTs potentially amplify inflammation by providing a microenvironment that allows intense interactions between renal parenchymal and immune cells. These interactions may serve as novel therapeutic targets in kidney diseases involving TLT formation.

JASN 00: 1–22, 2023. doi: <https://doi.org/10.1681/ASN.0000000000000202>

This is an open access article distributed under the terms of the [Creative Commons Attribution-Non Commercial-No Derivatives License 4.0 \(CCBY-NC-ND\)](https://creativecommons.org/licenses/by-nc-nd/4.0/), where it is permissible to download and share the work provided it is properly cited. The work cannot be changed in any way or used commercially without permission from the journal.

INTRODUCTION

Tertiary lymphoid tissues (TLTs) are ectopic lymphoid structures consisting mainly of T and B cells and functionally specialized fibroblasts. In mice and humans, they develop within nonlymphoid organs during chronic inflammation cases, such

Received: March 18, 2023 **Accepted:** July 10, 2023.

Published Online Ahead of Print: August 7, 2023.

Correspondence: Prof. Motoko Yanagita, Department of Nephrology, Graduate School of Medicine, Kyoto University, Shogoin-Kawahara-cho 54, Sakyo-ku, Kyoto 606-8507, Japan. Email: motoy@kuhp.kyoto-u.ac.jp

Copyright © 2023 The Author. Published by Wolters Kluwer Health, Inc. on behalf of the American Society of Nephrology.

as infection, autoimmune diseases, and cancers.^{1–4} TLTs have been also reported as an indicator for poor renal prognosis in various kidney diseases, such as transplanted kidneys,^{5,6} IgA nephropathy,⁷ and lupus nephritis,⁸ illustrating their clinical importance.

Previously, we demonstrated that TLTs develop in aged kidneys after injury and underlie sustained inflammation and impaired kidney regeneration.⁹ Cell-cell interactions between the two types of age-associated lymphocytes, senescence-associated T cells and age-associated B cells, *via* CD153-CD30 signaling pathway, are essential for TLT expansion. Targeting this pathway attenuates TLT formation and improves renal prognosis, suggesting the potential of TLTs as therapeutic targets.¹⁰ However, how renal parenchymal cells are affected by TLTs and contribute to TLT expansion remains unclear.

The recent development of single-cell transcriptomics has revealed heterogeneity among various kidney-composing cells, such as tubular cells,¹¹ fibroblasts,¹² and endothelial cells,¹³ in healthy and diseased kidneys and led to identification of specific cell types associated with kidney disease progression. This technology also has the potential to predict various cell-cell interactions and thus contribute toward the elucidation of the mechanisms underlying kidney disease development. Importantly, previous studies classified injured proximal tubular (PT) cells into heterogeneous populations using single-nucleus RNA sequencing (snRNA-seq) of young mouse kidneys.^{14,15} *Vcam1*⁺ PTs that increased in the late phase after kidney injury were classified as the failed repair PTs or late injured PTs with the proinflammatory and profibrotic phenotypes, which potentially contribute to CKD progression after AKI. However, such injured PTs have not yet been characterized sufficiently in aged injured kidneys with TLTs.

In this study, to elucidate the heterogeneity of renal parenchymal cells and their interactions with immune cells, we performed snRNA-seq of aged mouse kidneys with TLTs and validated the results in mice and humans. Conclusively, we demonstrate that TLTs potentially function as inflammation amplifiers by promoting the proinflammatory phenotypes of renal parenchymal cells and that their interactions with immune cells contribute to sustained inflammation and maladaptive repair.

METHODS

Animals

We purchased aged male C57BL/6J mice (12–14 months old) from Japan SLC. All mice were maintained in a specific pathogen-free animal facility at Kyoto University to minimize the effects of infection on TLT formation.¹⁶ All animal experiments were approved by the Animal Research Committee, Graduate School of Medicine, Kyoto University, and conducted in accordance with the Guide for the Care and Use of Laboratory Animals (US National Institutes of Health, Bethesda, MD).

Significance Statement

Ectopic lymphoid structures called tertiary lymphoid tissues (TLTs) develop in several kidney diseases and are associated with poor renal prognosis. However, the mechanisms underlying TLT expansion and their effect on renal regeneration remain unclear. The authors report that single-nucleus RNA sequencing and validation experiments demonstrate that TLTs potentially amplify inflammation in aged injured kidneys. Lymphocytes within TLTs promote proinflammatory phenotypes of the surrounding proximal tubules and fibroblasts within the TLTs *via* proinflammatory cytokine production. These proinflammatory parenchymal cells then interact with immune cells by chemokine or cytokine production. Such cell-cell interactions potentially increase inflammation, expand TLTs, and exacerbate kidney injury. These findings help illuminate renal TLT pathology and suggest potential therapeutic targets.

Unilateral Renal Ischemia-Reperfusion Injury Model

Unilateral ischemia-reperfusion injury (IRI) was induced by clamping the left renal pedicle for 45 minutes for a severe injury model or 18 minutes for a mild injury model. Mice were maintained at 37°C under anesthesia with 2% isoflurane inhalation. Sham surgery was performed using the same procedure without clamping.

Single-Nucleus Isolation and cDNA Library Preparation

Three 12-month-old male mice 30 days after unilateral IRI and one 12-month-old male mouse 30 days after sham surgery were separately used for snRNA-seq. The mice were euthanized under anesthesia with an intraperitoneal injection of a mixture of midazolam, butorphanol tartrate, and medetomidine hydrochloride. After perfusion with 30 ml of cold PBS *via* the left ventricle, the left kidney was harvested. The kidneys were cut along the short axis in the middle, and the half of the kidneys were snap frozen for snRNA-seq. Single-nucleus isolation was performed using the snap-frozen kidney tissues within 2 weeks after harvest, as described below. Kidney samples were minced into <2 mm pieces on a plate placed onto ice and homogenized in 2 ml of cold lysis buffer (Nuclei EZ Lysis buffer NUC-101, Sigma-Aldrich, Saint Louis, MO), protease inhibitor (cOmplete ULTRA tablet, 05892970001, Roche, Basel, Switzerland), and two types of 0.5% RNase inhibitor (Rnasin Plus, N2611, Promega, Madison, WI, and SUPERaseIn RNase Inhibitor, AM2694, Thermo Fisher Scientific, Waltham, MA) using dounce homogenizers. The homogenate was incubated for 5 minutes with an additional 2 ml of lysis buffer on ice. After incubation, the homogenate was filtered through a 40- μ m cell strainer (352340, Falcon, Corning, NY) and centrifuged at 500 \times g for 5 minutes under 4°C. The pellet was resuspended using 4 ml of cold lysis buffer, incubated for 5 minutes on ice, and centrifuged at 500 \times g for 5 minutes at 4°C. The pellet was resuspended using nuclei suspension buffer (1 \times PBS, 0.07% bovine serum albumin, 0.1% RNase inhibitor [Rnasin Plus, N2611, Promega]) and filtered through a 20- μ m cell strainer (43-50020-03, pluriSelect, Leipzig, Germany). The filtered

nuclei were counted using hemocytometers and observed with propidium iodide staining. The nuclei suspension was diluted to the appropriate concentration with additional nuclei suspension buffer and kept on ice until loading into a Chromium Controller (10X Genomics, Pleasanton, CA). The diluted nuclei suspension was loaded onto a Chromium Controller to prepare cDNA libraries in accordance with the manufacturer's instruction. We used Chromium Single Cell 3' Reagent Kits v3 (10X Genomics) for the first IRI kidney and the sham-treated control kidney and Chromium NEXT GEM Single Cell 3' Reagent Kits v3.1 (10X Genomics) for the second and the third IRI kidneys after the company's version update. Quality of the cDNA libraries were evaluated using Agilent 2200 TapeStation (Agilent, Santa Clara, CA).

snRNA-seq Data Preprocessing and Analysis

The prepared cDNA libraries were sequenced using a HiSeq 4000 sequencer (Illumina, San Diego, CA). The sequencing data were processed using the Cell Ranger pipeline version 3.1.0 (10X Genomics) with the mm10-3.0.0 Cell Ranger reference customized to count intronic reads, in accordance with the manufacturer's instructions. The downstream data analysis, including initial filtering, normalization, identification of highly variable genes, scaling, unsupervised clustering, finding markers, and integration of the datasets was performed using the R package Seurat (version 3.1.1) in accordance with the Seurat vignette.¹⁷ We analyzed each dataset separately and generated new gene expression matrices for all datasets as described below, and a graphical flowchart is displayed in Supplemental Figure 1. We filtered out the genes expressed in fewer than three nuclei and nuclei that expressed fewer than 300 genes or more than 6000 genes to exclude low-quality nuclei and possible doublets. We also excluded nuclei with a high unique molecular identifier (UMI) count of mitochondrial genes that was >0.5%. Normalization was performed using the NormalizeData function by the default logNormalize method with a scale factor of 10,000. Highly variable genes were identified using the FindVariableGenes function with the default setting. We scaled the data with the ScaleData function to regress out the variation between nuclei because of the library size and the percentage of mitochondrial genes. The data were subjected to principal component analysis (PCA) dimensional reduction using the RunPCA function. The number of PCs used for the downstream analysis was determined on the basis of the elbow point visualized by the ElbowPlot function after running the JackStraw function. The determined PCs were used to perform unsupervised clustering with the FindNeighbors and FindClusters functions and to generate Uniform Manifold Approximation and Projection (UMAP) with the RunUMAP function. All datasets for IRI kidneys included a nonspecific cluster with a low number of expressed genes and without cell type-specific markers, and after the nonspecific cluster was excluded, the retained data were reanalyzed as described above using Seurat. We then used the R package DoubletFinder (version 2.0.2) to exclude

estimated doublets, in accordance with the manufacturer's instructions.¹⁸ After removing the estimated doublets, the retained datasets were reanalyzed as described above using Seurat, and we used the R package SoupX (version 1.3.7) to exclude ambient RNA expression estimated from the expression patterns in the nuclei-free droplets with extremely low UMI counts of ten UMIs or less.¹⁹ To estimate contamination fractions, we used the autoEstCont function for the sham-treated kidney dataset and the calculateContaminationFraction function with the nonExpressedGeneList set to the B cell-specific genes, *Cd19* and *Ighd*, for IRI kidney datasets. We then generated new gene expression matrices by subtracting the estimated contamination fractions from the original datasets, using the adjustCounts function. The newly generated gene expression matrix for each kidney was used for the downstream analysis. Similar cell populations were identified across the three IRI replicates that were analyzed separately using three newly generated IRI kidney datasets (Supplemental Figure 2A). To mitigate batch effects, the three newly generated IRI datasets were integrated with the IntegrateData function using canonical correlation analysis after identifying anchors using the FindIntegrationAnchors function in Seurat.¹⁷ Each replicate was confirmed to include all cell types in the integrated IRI kidney dataset (Supplemental Figure 2, B and C). The three newly generated IRI and sham-treated control datasets and the fibroblast subsets from IRI and sham-treated kidneys were integrated in the same manner. The subset function was used to create new Seurat objects comprising the PT cell clusters or the fibroblast clusters from the sham dataset and the integrated IRI dataset for the subset analysis. To identify marker genes in each cluster, the FindAllMarkers function in Seurat was used with the following cutoff settings: min pct=0.1; and logfc. threshold=0.25. Marker genes detected in the analysis of each dataset used in this study are listed in Supplemental Table 1. The parameters and number of nuclei used in the computational analysis are listed in Supplemental Table 2. Cell type annotation was performed based on previously published canonical cell type-specific markers^{11,20–24} using single-cell RNA sequencing (scRNA-seq) online databases (Kidney Cell Explorer [https://cello.shinyapps.io/kidney_cellexplorer/]²⁵ and Kidney Interactive Transcriptomics [<http://humphreyslab.com/SingleCell/>]).²⁶

Analysis of Ligand Expression Selected from Marker Genes for the Injured PT Cluster

We selected the genes encoding ligands from the marker genes for the injured PT-1 cluster in PT subset analysis in the IRI kidney dataset on the basis of the human ligand-receptor list²⁷ and plotted the expression patterns of the selected genes across the four PT clusters as dot plots using the DotPlot function in Seurat.

Pearson Correlation Analysis

Pearson correlation coefficients were calculated between the injured PT-1 cluster in our IRI kidney dataset and PT

subpopulations in the young IRI kidney dataset in previous publication¹⁴ on the basis of the average expression profiles of marker genes for PT subpopulations in our PT subset of the IRI kidney dataset (Supplemental Table 1, IRI_PT_subset). The average expression was calculated by the AverageExpression function in Seurat. These Pearson correlation coefficients were displayed as a heatmap using the R package pheatmap (version 1.0.12).

Ligand-Receptor Analysis

To investigate cell-cell interactions, we performed three ligand-receptor analyses between the following groups: (1) the injured PT-1 cluster and each immune cell cluster, (2) the injured PT-1 cluster and the fibroblast cluster, and (3) the proinflammatory fibroblast cluster and lymphocyte clusters (T-cell and B-cell clusters) in the integrated IRI kidney dataset using CellPhoneDB (version 2.0).²⁸ The lower cutoff for the proportion of cells expressing any ligands or receptors in a specific cell type was set to 10%. In the analysis, only ligand-receptor interactions with a significant *P*-value (<0.05), including ligands listed both in the human ligand-receptor list²⁷ and in the marker gene lists of the specific clusters (Supplemental Table 1), were plotted.

Gene Regulatory Network Analysis

Gene regulatory network analysis was performed on the PT subset and the fibroblast subset in the integrated IRI kidney dataset using the R package single cell regulatory network inference and clustering (version 1.2.4) with normalized expression values from Seurat objects as input, in accordance with the manufacturer's vignette.²⁹ In brief, we identified gene sets coexpressed with transcription factors (TFs) using GENIE3. Subsequently, we removed indirect targets lacking motif support from each coexpression module with cis-regulatory motif analysis using RcisTarget. We used the mouse mm10 genome and two gene-motif rankings (ten kilobases around the transcription start site or 500 base pairs [bp] upstream and 100 bp downstream of the transcription start site), as previously described.¹⁴ The processed modules are called regulons. Finally, we scored each regulon activity in each cell and calculated each average regulon activity in each cluster. The scaled regulon activities were visualized as heatmaps using the R package pheatmap (version 1.0.12).

Pseudotime Trajectory Analysis

Pseudotime trajectory analysis was performed on the integrated PT and fibroblast subsets from sham-treated and IRI kidney datasets. We used the R package Monocle2 (version 2.12.0) with normalized expression values as input.³⁰ The combination of the marker genes identified using the FindAllMarkers function in Seurat for each cluster in the integrated PT and fibroblast dataset (Supplemental Table 1) were used for ordering of the cells. The branches, including most of the nuclei from the sham-treated kidney, were defined as the starting states of cell differentiation. In analysis of PTs, we identified differentially expressed genes over pseudotime from the marker

genes for PT subpopulations with $\min \text{pct} > 0.25$ and $\log_{2}\text{fc}$ threshold > 0.8 , using the differentialGeneTest function in Monocle2, and the expressional changes of these genes over pseudotime was displayed in a heatmap (genes with *q*-value < 0.001). In the analysis of fibroblasts, to further resolve the differentiation into different fibroblast substates, subset analysis was performed. In the subset analysis, we identified the branch-dependent genes that were significantly differentially expressed between each branch starting from the branch point to different cell states using the branched expression analysis modeling function implemented in Monocle2.

Enrichment Analysis

Enrichment analyses were performed on the reclustered PT clusters and fibroblast clusters in the integrated IRI kidney dataset using the web tool Enrichr (<https://maayanlab.cloud/Enrichr/>).^{31–33} We used marker genes for each cluster identified by the FindAllMarkers function in Seurat as input (Supplemental Table 1), and we used the Kyoto Encyclopedia of Genes and Genomes (KEGG) 2019 Mouse^{34,35} and Gene Ontology (GO) Biological Process 2018 databases.^{36,37}

Bulk RNA-Sequencing Analysis

Bulk RNA-sequencing libraries were prepared using a NEBNext Ultra II Directional RNA Library Prep Kit for Illumina (E7760, New England Biolabs, Ipswich, MA) following the manufacturer's instructions. The libraries were sequenced on a NovaSeq 6000 (Illumina) to generate 50 bp pair-end reads at a read depth of at least 15 million reads per sample. The pair-end reads were mapped to Ensembl human reference genome (GRCh38.p13), using STAR (version 2.6.0c).³⁸ The expected count and transcripts per million were calculated using RSEM (version 1.3.1).³⁹ Differential expression analyses were conducted using DESeq2 (version 4.3).⁴⁰ Scatter plots were generated using ggpubr (version 0.6.0). The scatter plots showed that names of selected genes that were upregulated or downregulated in the injured PT-1 from our snRNA-seq dataset that were identified using the FindMarkers function in Seurat (version 3.1.1) with the following cutoff settings: $\min \text{pct} = 0.1$; and $\log_{2}\text{fc}$ threshold = 0.25.

Human Kidney Specimens and TLT Identification

Samples of protocol renal biopsies from two patients 1 year after transplantation were analyzed after obtaining informed consent and with the approval of the Ethics Committee of Kyoto University Hospital (registration number: G0562). Clinical profiles of these patients are shown in Supplemental Table 3. In human transplanted kidney samples, TLTs were defined as organized lymphocyte aggregates composed of more than 60 cells (T cells or B cells) with a proliferative sign, as previously described.⁶ Lymphocyte infiltration was assessed using CD20 and CD3 ϵ immunofluorescence, and their proliferation was assessed using Ki67 immunofluorescence. This study was

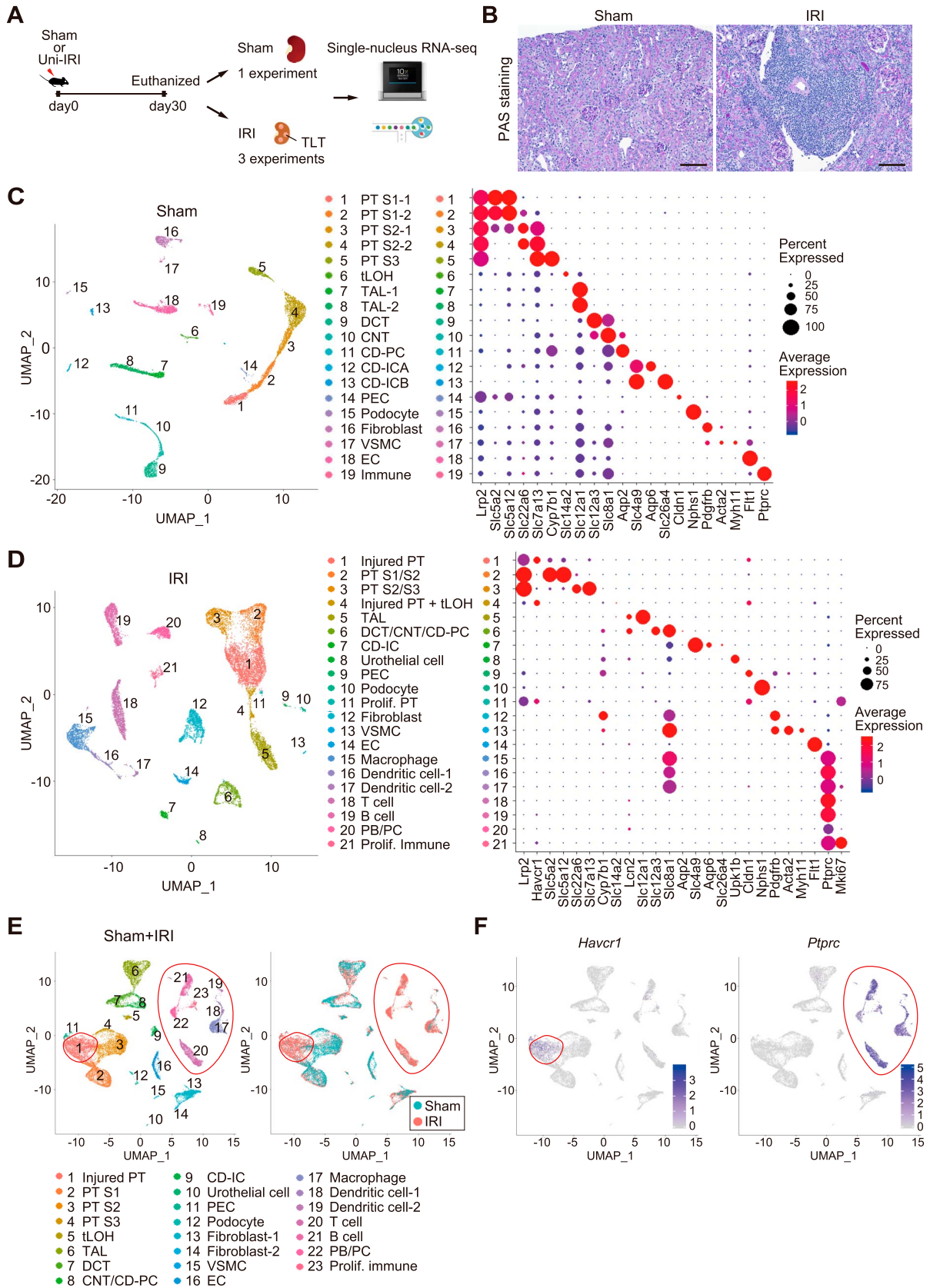


Figure 1. snRNA-seq revealed injured PT cells and various immune cells emerged in aged injured kidneys with TLTs. (A) Summary of snRNA-seq workflow. snRNA-seq was performed on individual kidneys 30 days after sham surgery or 45-minute Uni-IRI.

Figure 1. (Continued) The illustrations were used from the homepage of 10X Genomics (<https://www.10xgenomics.com/jp>) with permission. (B) PAS staining of murine kidneys 30 days after sham surgery and IRI, which were used for snRNA-seq. Scale bars=100 μ m. PAS staining, Masson-Trichrome staining, and immunofluorescence for the sham-treated and IRI kidneys are displayed in [Supplemental Figure 5](#). (C) UMAP plots of a kidney 30 days after sham surgery, which were classified into 19 clusters, and dot plots displaying gene expression patterns of representative marker genes for each cluster. (D) UMAP plots of the integrated IRI kidney dataset, which were classified into 21 clusters, and dot plots displaying expression patterns of representative marker genes for each cluster. (E) A left panel displayed UMAP plots of the integrated dataset of the sham-treated and three IRI kidneys, which were classified into 23 clusters. A right panel showed the UMAP plots separated by sample types, sham (blue dots) and IRI (red dots). Red lines encircled clusters mainly composed of the nuclei derived from the IRI kidneys (cluster 1, 17–23). (F) Feature plots showing high gene expression of *Havcr1* encoding KIM1 in cluster 1 and *Ptprc* encoding CD45, an immune cell marker, in clusters 17–23 in the integrated dataset of a sham-treated and three IRI kidneys. CD, collecting duct; CNT, connecting tubule; DCT, distal convoluted tubule; EC, endothelial cell; IC, intercalated cell; PAS, Periodic acid–Schiff; PB/PC, plasmablast/plasma cell; PC, principal cell; PEC, parietal epithelial cell; Prolif., proliferating; PT, proximal tubule; S1/S2, S1 segment/S2 segment; S2/S3, S2 segment/S3 segment; snRNA-seq, single-nucleus RNA sequencing; TAL, thick ascending limbs of the loop of Henle; tLOH, thin limbs of the loop of Henle; TLT, tertiary lymphoid tissues; UMAP, Uniform Manifold Approximation and Projection; Uni-IRI, unilateral ischemia-reperfusion injury; VSMC, vascular smooth muscle cell.

conducted in accordance with the Declaration of Helsinki. The clinical and research activities being reported are consistent with the Principles of the Declaration of Istanbul as outlined in the Declaration of Istanbul on Organ Trafficking and Transplant Tourism.

Quantification of VCAM1⁺ PT Cells

Quantification of VCAM1⁺ cells and KIM1⁺ cells in PT cells was performed on aged injured kidneys 30 days after 18-minute IRI. PT cells were defined as those stained with LTL or KIM1. Three regions of interest (ROIs), including TLTs per kidney section ($n=5$, total of 15 ROIs), were analyzed at the magnification of $\times 20$. Quantitative analysis was performed for PT cells adjacent to TLTs that were at least partially contained within the 35 μ m line from the periphery of TLTs and for PT cells not adjacent to TLTs that were outside of the line in each ROI. We also performed this analysis with a different cutoff distance, 10 μ m, from TLT borders. The representative images are shown in [Supplemental Figure 3](#).

Deletion of Stat1 Gene in C3H10T1/2 Cells by Clustered Regularly Interspaced Short Palindromic Repeats/Cas9 System

Stat1 genes were deleted from C3H10T1/2 cells using the clustered regularly interspaced short palindromic repeats/Cas9 gene-editing system, as described below.⁴¹ We designed guide RNAs (gRNA) for exon4 of *Mus musculus Stat1* with the fewest off-target sites (sequence: GGTCGCAAACGAGACATCAT) using the online tool CRISPOR (<http://crispor.tefor.net/>).⁴² In brief, pX330-GFP plasmids (kindly provided by Professor Osamu Takeuchi), which included GFP sequences and Cas9 sequences, were digested using Bbs1 and ligated together with dsDNA, including the gRNA sequence. The ligated plasmids were transfected into C3H10T1/2 cells using a lipofectamine method (Lipofectamine 3000 Transfection Kit, L3000-015, Thermo Fisher Scientific). For the control C3H10T1/2 cells, the original pX330-GFP plasmids with no gRNA sequences were transfected. After incubation, single cell sorting of GFP-positive cells, which appeared to be successfully transfected with the plasmids, into 96-well plates was

performed using BD FACS Aria Fusion (BD Bioscience, Franklin Lakes, NJ) and then each single-cell clone was expanded. After expansion, Sanger sequence and western blotting were performed to screen cells lacking the STAT1 gene and protein and to analyze the potential off-target mutations with a high Cutting Frequency Determination score calculated using the CRISPOR analysis ([Supplemental Figure 4](#)).

Statistics

Proportions of VCAM1⁺ PT cells are shown as the median and interquartile range. They were compared using the Mann-Whitney test between PT cells adjacent to TLTs and PT cells not adjacent to TLTs, defined as described above. Data for quantitative real-time PCR are presented as the mean \pm SEM, and statistical significance was determined using a one-way ANOVA followed by the Tukey-Kramer *post hoc* tests for comparisons among more than two groups. Statistical analyses were performed using GraphPad Prism for mac (version 9.50; GraphPad Software, La Jolla, CA). In these analyses, a *P*-value < 0.05 was considered significant.

RESULTS

Injured PTs and Various Immune Cells Emerge in Aged Injured Kidneys with TLTs

snRNA-seq was performed on three aged kidneys 30 days after IRI and one aged kidney after sham surgery ([Figure 1A](#)). Histological examination of IRI kidneys, but not sham-treated kidneys, revealed extensive tubular atrophy, interstitial fibrosis, and multiple cortical TLTs mainly composed of CD3 ϵ ⁺ T and B220⁺ B cells and p75 neurotrophin receptor (p75NTR)⁺ fibroblasts ([Figure 1B](#), [Supplemental Figure 5, A–C](#)).

In the sham-treated kidney dataset, 7,485 nuclei were classified into 19 clusters ([Figure 1C](#)), whereas, in the integrated dataset for the three IRI kidneys, 15,968 nuclei were classified into 21 clusters ([Figure 1D](#)). In the integrated IRI kidney dataset, there were seven independent *Ptprc*⁺ immune cell clusters (clusters 15–21 in [Figure 1D](#)), indicating

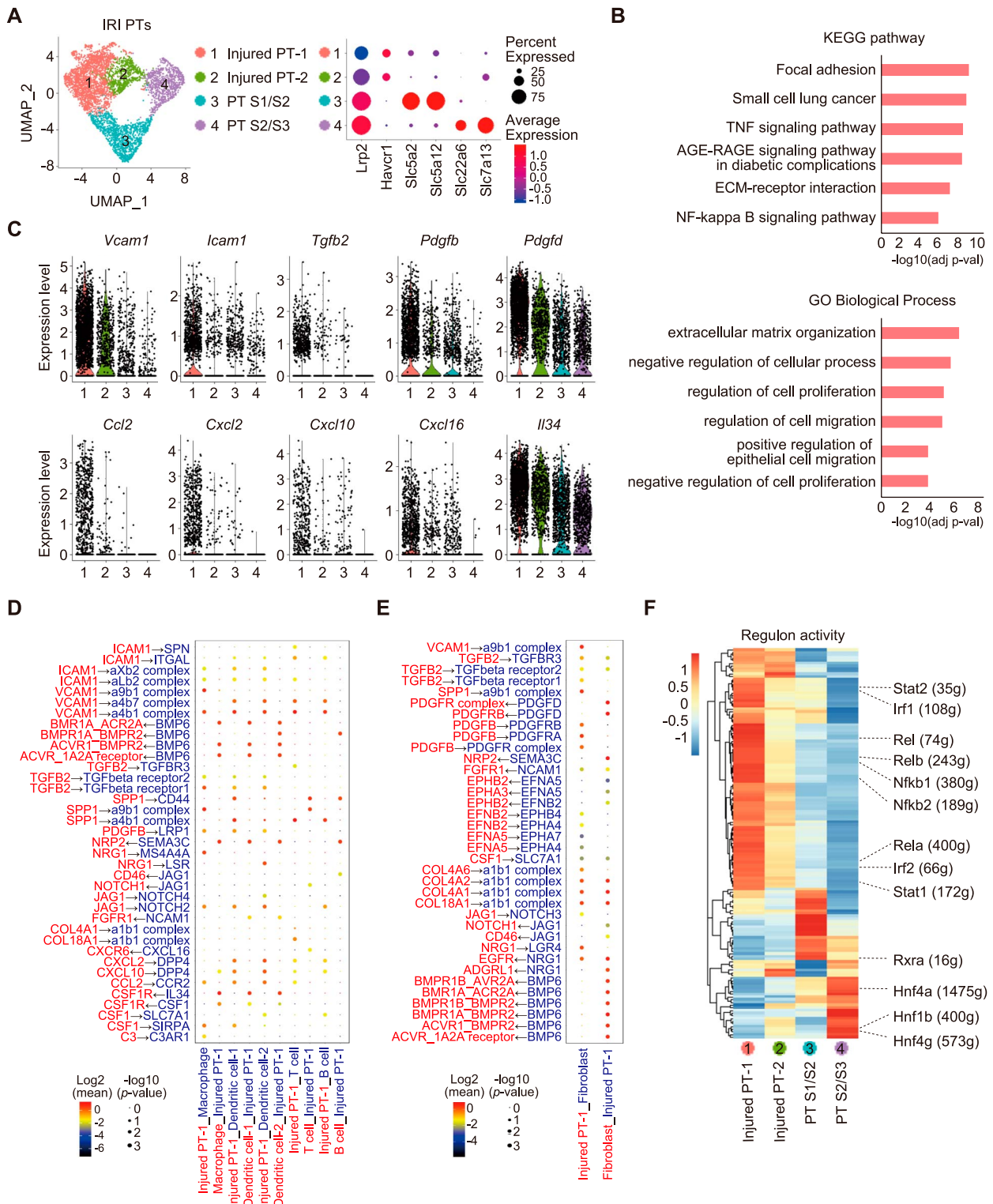


Figure 2. Subset analysis of PT clusters in the ischemia-reperfusion injury kidneys showed proinflammatory and profibrotic injured PTs interacting with immune cells and fibroblasts. (A) UMAP plots displaying the reclustering of the PT cell subset in the integrated IRI kidney dataset and dot plots showing expression patterns of the representative marker genes for each PT cluster. Clusters 1 and 2, which expressed *Havcr1* (encoding KIM1), were annotated as injured PT-1 and injured PT-2, respectively. (B) Enrichment analysis on the marker genes of injured PT-1 was performed. Top six KEGG pathways and GO terms are shown in the bar graphs. Significance was expressed as $-\log_{10}(\text{adjusted } P\text{-value})$. (C) Violin plots showing the gene expression patterns of adhesive molecules (*Vcam1* and *Icam1*), profibrotic ligands (*Tgfb2*, *Pdgfb*, and *Pdgfd*), and chemokines or cytokines (*Ccl2*, *Cxcl2*, *Cxcl10*,

Figure 2. (Continued) *Cxcl16*, and *Il34*) across the PT clusters in the IRI kidneys. (D, E) A heatmap showing selected ligand-receptor interactions between (D) injured PT-1 and each immune cell type and (E) injured PT-1 and fibroblasts in the IRI kidney dataset. The color of the cell types (red or blue) corresponds to the color of the ligands or receptors expressed by the cell types. In each ligand-receptor pair name, the molecule at the root of the arrow is a ligand and the molecule at the arrowhead is a receptor. The dot size indicates the $-\log_{10}(P\text{-value})$ calculated using CellphoneDB, and the dot color indicates the log scaled mean expression of the ligand and receptor. (F) Gene regulatory network analysis was performed on each PT cluster in aged injured kidneys. The heatmap showed the average regulon activity across the four PT clusters. Representative TFs activated in each cluster were highlighted. The number of predicted target genes was shown following each TF's name. IRI, ischemia-reperfusion injury; PT, proximal tubule; TF, transcription factor; UMAP, Uniform Manifold Approximation and Projection.

infiltration of macrophages, dendritic cells, and T, B, and plasmablasts/plasma cells (Supplemental Figure 6). In addition, three major *Lrp2*⁺ (encoding megalin) PT clusters (clusters 1–3 in Figure 1D) were identified. Subsequently, the integrated sham-treated and IRI kidney datasets demonstrated that injured PTs expressing *Havcr1* (encoding KIM1, a well-known marker of PT injury) (cluster 1) and *Ptprc*⁺ immune cells (clusters 17–23) were the major cell populations that newly emerged after IRI (Figure 1, E and F). Expression of *Lcn2* (encoding Ngal, a distal tubular injury marker) was detected in distal nephron clusters derived from the IRI kidneys (Supplemental Figure 7). In short, tubular maladaptive repair and kidney inflammation persisted in aged kidneys with TLTs, even a month after IRI.

snRNA-seq Detects Proinflammatory and Profibrotic *Vcam1*⁺ Injured PTs with Potential Interactions with Various Immune Cell Types and Fibroblasts

Three major PT clusters (clusters 1–3 in Figure 1D) in the integrated IRI kidney dataset were reanalyzed and classified into four clusters, including two *Havcr1* (encoding KIM1)⁺ injured PT clusters (clusters 1 and 2 in Figure 2A). Enrichment analysis indicated enrichment of focal adhesion and proinflammatory pathways, such as TNF and NFκB signaling pathways in injured PT-1 cells, compared with other clusters (Figure 2B, Supplemental Figure 8, A and B, Supplemental Table 4). In addition, many types of ligands, including adhesion molecules (*Vcam1* and *Icam1*), chemokines, and cytokines (*Ccl2*, *Cxcl2*, *Cxcl10*, *Cxcl16*, and *Il34*), were highly expressed in injured PT-1 cells, indicating their proinflammatory phenotype (Figure 2C, Supplemental Figure 9). Injured PT-1 cells also expressed profibrotic ligands (*Tgfb2*, *Pdgfb*, and *Pdgfd*) (Figure 2C, Supplemental Figure 9).^{43–45} Pearson correlation analysis was performed between the injured PT-1 and PT subpopulations in young IRI kidney dataset in previous publication,¹⁴ demonstrating that the injured PT-1 was the most similar to the failed repair PTs (Supplemental Figure 10). Subsequently, based on their high expression of chemokines and cytokines, we conducted ligand-receptor analysis between the *Havcr1*⁺*Vcam1*⁺ injured PT-1 cells and immune cells, detecting their cell-cell interactions via various pathways, including *Ccl2*–*Ccr2*, *Cxcl16*–*Cxcr6*, and *Vcam1*/*Icam1*–*integrin* (Figure 2D). CCL2 contributes to the chemotaxis of CCR2⁺ macrophages and dendritic and T cells⁴⁶ while CXCL16 recruits CXCR6⁺-activated T cells.⁴⁷

Although *Cxcl10* expression was detected in injured PT-1 cells, the *Cxcl10*–*Cxcr3* pathway was not detected in this ligand-receptor analysis, possibly because of the low detection sensitivity of snRNA-seq for immune cells (*Cxcr3* expression was not detected in this analysis).⁴⁸ By contrast, *Cxcr3* expression in T cells was detected in our previous scRNA-seq data for CD45⁺ immune cells in aged injured kidneys with TLTs¹⁰ (Supplemental Figure 11, A and B) and was also previously reported,^{49,50} suggesting interactions between injured PT cells and T cells via *Cxcl10*–*Cxcr3* pathway in aged injured kidneys. CXCL10 contributes to CXCR3⁺ T-cell chemotaxis and polarization into IFNγ-producing T-helper type 1 cells.^{51,52} These findings suggest that *Havcr1*⁺*Vcam1*⁺ injured PT cells may exacerbate inflammation by recruiting and activating immune cells, especially macrophages and dendritic and T cells, via multiple chemokine or cytokine production.

Furthermore, we also conducted ligand-receptor analysis between the injured PT-1 cells and fibroblasts on the basis of the expression of profibrotic ligands in injured PT-1 cells, revealing potential interactions between them via profibrotic pathways, such as the *Tgfb2*–*Tgfb* receptors and *Pdgfb*/*Pdgfd*–*Pdgf* receptors, suggesting that injured PT-1 cells may activate fibroblasts and aggravate fibrosis (Figure 2E).^{43–45}

Subsequently, we used single-cell regulatory network inference and clustering to detect the gene regulatory network in PT subpopulations in the injured kidneys and showed that activities of regulons, such as NFκB (*Nfkb1* and *Rela*) and IFN-inducible TFs (*Stat1* and *Irf1*), were upregulated especially in the injured PT-1 (Figure 2F, Supplemental Table 5).

Trajectory analysis on integrated data of the PT subsets in the sham-treated and IRI kidney datasets identified differentially expressed genes over pseudotime from healthy PTs toward injured PTs, showing expression changes of the genes (*q*-value < 0.001) in a heatmap (Supplemental Figure 12).

VCAM1⁺ Injured PTs with NFκB and IFN-Inducible TFs Activation Are Preferentially Localized around TLTs

Subsequently, we identified the localization of KIM1⁺VCAM1⁺ injured PTs in aged injured kidneys with TLTs. Immunostaining revealed that KIM1⁺VCAM1⁺ injured PTs were extensively distributed in injured kidneys after severe IRI (Figure 3A, 45 minutes IRI). In the mild IRI model (Supplemental Figure 13), approximately 84% (median) of KIM1⁺ injured PT cells also expressed VCAM1 (Figure 3A 18 minutes IRI and 3B). Moreover, PT cells adjacent to TLTs expressed VCAM1 more

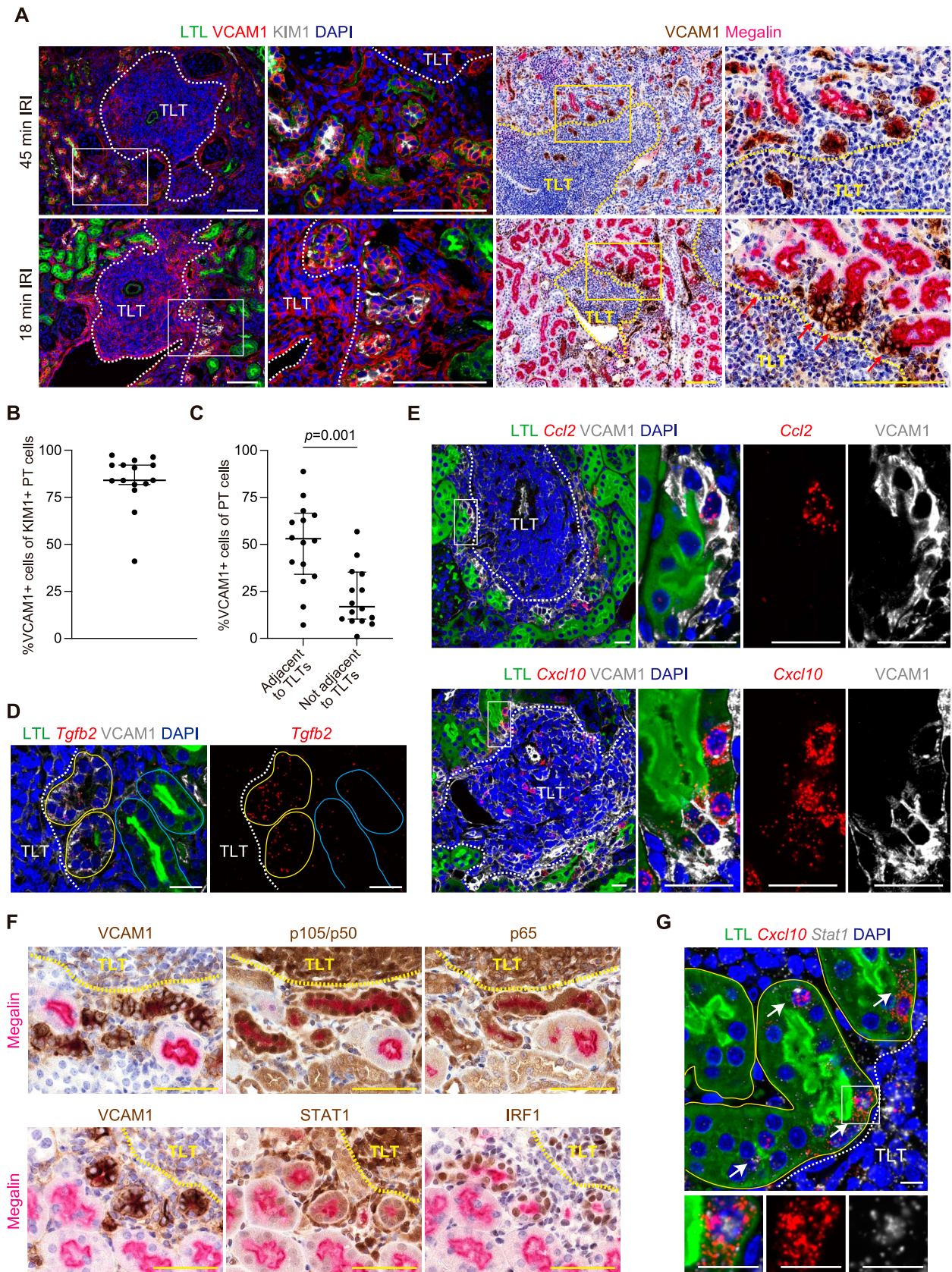


Figure 3. Proinflammatory and profibrotic VCAM1⁺ injured PTs are preferentially localized around TLTs. (A) Representative immunofluorescence images of LTL (green), VCAM1 (red), and KIM1 (gray) and immunohistochemistry images staining for VCAM1

Figure 3. (Continued) (brown) and megalin (pink) in the kidneys 30 days after 45-minute severe IRI (upper panels) and 18-minute mild IRI (lower panels). The areas enclosed by rectangles in the left panel are enlarged in the right panel in each staining. Images of severely injured kidneys showed that most of the KIM1⁺ injured PTs expressed VCAM1. In mild IRI kidneys, VCAM1⁺ PT cells were preferentially localized around TLTs. In some PTs, VCAM1 staining was observed only in the cells adjacent to TLTs in the same tubules (red arrows in the magnified image located in the lower right). Scale bars=100 μ m. (B, C) Quantification of the percentages of VCAM1⁺ PT cells among (B) all KIM1⁺ PT cells and (C) PT cells adjacent to TLTs or PT cells not adjacent to TLTs, in each ROI in mild IRI model, using three ROIs including TLTs per kidney section ($n=5$, total of 15 ROIs). Approximately 84% of KIM1⁺ injured PT cells expressed VCAM1. VCAM1⁺ PT cells were significantly more prevalent around TLTs than in the other area ($P = 0.001$). Data are shown as the median and interquartile range. Mann-Whitney test was used to analyze the difference in (C). The representative images used for counting VCAM1⁺ or KIM1⁺ PT cells are shown in Supplemental Figure 3. (D) A combination of ISH with RNAscope (*Tgfb2* [red]) and immunofluorescence (LTL [green], VCAM1 [gray], DAPI [blue]) showed more intense *Tgfb2* expression in VCAM1⁺ injured PTs (encircled by yellow solid lines) adjacent to TLTs than in VCAM1⁻ PTs (encircled by light blue solid lines) in aged injured kidney 30 days after 45-minute IRI. Scale bars=20 μ m. (E) A combination of ISH with RNAscope (*Ccl2* [upper panel, red] or *Cxcl10* [lower panel, red]) and immunofluorescence (LTL [green], VCAM1 [gray], and DAPI [blue]) for aged injured kidneys 30 days after 18-minute mild IRI showed *Ccl2* or *Cxcl10* expression in the VCAM1⁺ injured PT cells adjacent to TLTs. The areas enclosed by rectangles are magnified in the right panels. Scale bars=20 μ m. (F) Immunohistochemistry images staining for VCAM1, p105/p50, and p65 (brown), and megalin (pink) (upper panels) and VCAM1, STAT1, and IRF1 (brown) and megalin (pink) (lower panels) in serial sections of aged injured kidneys 30 days after 18-minute mild IRI. Expression and nuclear translocation of these transcription factors were upregulated in the VCAM1⁺ PTs surrounding TLTs. Scale bars=50 μ m. Immunofluorescence images for p105/p50 and STAT1 in aged injured kidneys are also shown in Supplemental Figure 15. (G) A combination of ISH (*Cxcl10* [red] and *Stat1* [gray]) and immunofluorescence (LTL [green] and DAPI [blue]) displayed high *Cxcl10* and *Stat1* expression in the same PT cells surrounding TLTs (arrows). The area enclosed by a square was magnified in the lower panels. PTs are enclosed by yellow solid lines. Scale bars=20 μ m. TLT borders are displayed as white dashed lines in immunofluorescence images and yellow dashed lines in immunohistochemistry images in (A and D–G). IRI, ischemia-reperfusion injury; ISH, *in situ* hybridization; PT, proximal tubule; ROI, region of interest; TLT, tertiary lymphoid tissue.

frequently compared with PT cells not adjacent to TLTs (Figure 3C, Supplemental Figure 3D, see Methods for the definition of PT cells adjacent to TLTs). Interestingly, in some PTs, only the cells adjacent to the TLTs in the same tubule were positive for VCAM1. Consistent with the results of the data analysis, *Tgfb2*, *Ccl2*, and *Cxcl10* expression was detected in VCAM1⁺ injured PT cells surrounding TLTs (Figure 3, D and E), confirming that these VCAM1⁺ injured PTs around TLTs could contribute to the augmentation of inflammation and fibrosis. Compared with young injured kidneys, aged kidneys with TLTs showed more VCAM1⁺ injured PTs and higher gene expression of adhesion molecules, chemokines, and cytokines expressed by them (Supplemental Figure 14), suggesting the association of TLTs with tubular maladaptive repair, sustained inflammation, and progressive fibrosis in aged kidneys. Furthermore, immunostaining and *in situ* hybridization (ISH) demonstrated intense p105/p50 (encoded by *Nfkb1*), p65 (encoded by *Rela*), STAT1, and IRF1 expression and nuclear translocation in VCAM1⁺ injured PT cells surrounding the TLTs (Figure 3F, Supplemental Figure 15, Supplemental Figure 16). *Cxcl10*, an IFN-inducible chemokine, was also highly expressed in *Stat1*-expressing PT cells surrounding the TLTs (Figure 3G). These findings suggest that NF κ B and IFN-inducible TF activation may contribute to the proinflammatory phenotype of PTs surrounding TLTs.

Increased TNF α and IFN γ Production within TLTs May Promote the Proinflammatory Phenotype of Injured PTs Surrounding TLTs in Murine and Human Kidneys

The localized activation of NF κ B and IFN-inducible TFs in the PTs surrounding TLTs suggested that cytokines produced

within TLTs affect the phenotype of the surrounding PT cells. We have previously reported that TLT size is positively correlated with TNF α and IFN γ expression levels in aged injured kidneys.⁹ Similarly, ISH for *Tnf* and *Ifng* showed intense expression within TLTs (Figure 4A). snRNA-seq and scRNA-seq of CD45⁺ immune cells in aged injured kidneys revealed that *Tnf* was expressed by several immune cell types, including T and B cells, whereas *Ifng* was exclusively expressed by T cells (Figure 4B, Supplemental Figure 11, C and D).¹⁰ In HK-2 cells, a PT cell line, *VCAM1*, *ICAM1*, *CCL2*, and *CXCL10* expression was synergistically upregulated by costimulation with TNF α and IFN γ (Figure 4C). Bulk RNA sequencing of the treated HK-2 cells also showed that these cytokines synergistically upregulated several other marker genes for the injured PT-1, including the genes encoding ligands (Figure 4, D–F, Supplemental Table 6). These results suggest that a local increase in TNF α and IFN γ production by lymphocytes within TLTs could promote the adhesive and proinflammatory phenotypes of PT cells surrounding the TLTs. Furthermore, proinflammatory injured PTs surrounding TLTs may promote inflammation and TLT expansion *via* chemokine or cytokine production.

As observed in murine kidneys, VCAM1⁺ injured PTs existed not only in the area with diffuse infiltrates of immune cells but also around TLTs (Figure 4G), and p65 and phospho-STAT1 (Tyr701) (pSTAT1) expression and nuclear translocation were upregulated in these VCAM1⁺ PTs (Figure 4H) in the transplanted human kidneys 1 year after transplantation (case 1 is a 47-year-old male patient diagnosed with chronic active T-cell-mediated rejection and case 2 is a 39-year-old female patient diagnosed with borderline lesion). More detailed patient

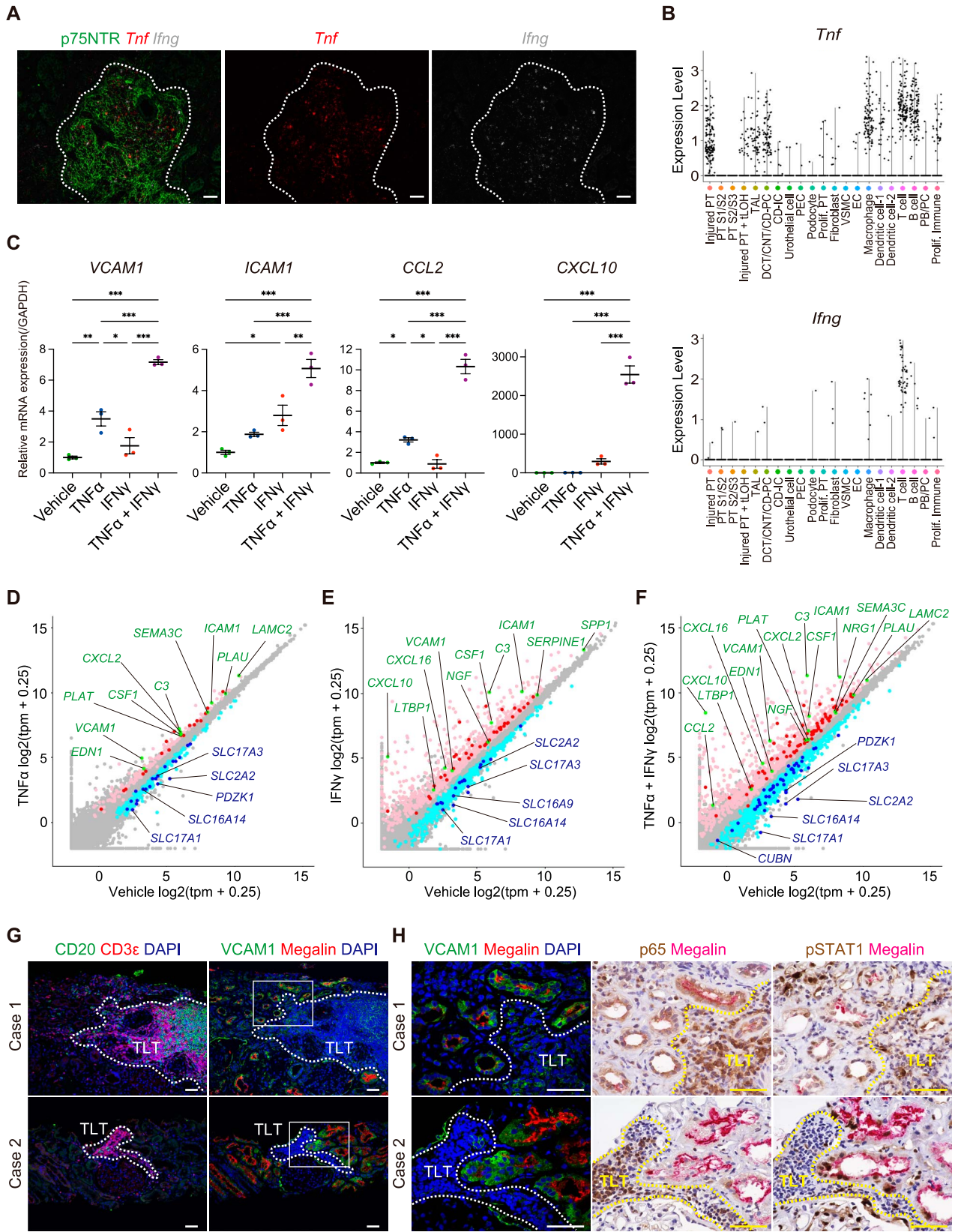


Figure 4. Increased production of TNF α and IFN γ within TLTs may promote the proinflammatory phenotype of surrounding injured PTs in murine and human kidneys. (A) A combination of ISH (*Tnf* [red] and *Ifng* [gray]) and immunofluorescence (p75NTR [green], a marker for fibroblasts within TLTs) showed the cells highly expressing *Tnf* and *Ifng* accumulated within TLTs in aged injured

Figure 4. (Continued) kidneys. Scale bars=50 μm . (B) Violin plots showing *Tnf* and *Ifng* expression patterns in the integrated IRI kidney dataset, showing that macrophages, T cells, and B cells expressed higher *Tnf* levels than the other populations and T cells expressed higher *Ifng* levels than the other populations. (C) The representative results of quantitative real-time PCR for HK2 cells, a human PT cell line, treated with vehicle (as a control), $\text{TNF}\alpha$, $\text{IFN}\gamma$, or both for 24 hours were displayed ($n=3/\text{group}$). Relative *VCAM1*, *ICAM1*, *CCL2*, and *CXCL10* mRNA expressions were shown. The expression levels were normalized to those of *GAPDH*. Values were shown as mean \pm SEM. Statistical significance was determined using a one-way ANOVA followed by the Tukey-Kramer *post hoc* test ($*P < 0.05$, $**P < 0.01$, and $***P < 0.001$). (D–F) Scatter plots showing differentially expressed genes between HK-2 cells treated with vehicle and (D) $\text{TNF}\alpha$, (E) $\text{IFN}\gamma$, or (F) both cytokines. Each axis showed the log₂ scale of average transcripts per million (tpm) with the addition of 0.25. Colored dots indicated transcripts with log₂ fold change >0.5 or < -0.5 and adjusted *P*-value < 0.05 . Genes that were significantly upregulated and downregulated in the HK-2 cells treated with the cytokines were shown as light red and light blue dots, respectively. Genes upregulated and downregulated both in injured PT-1 in our snRNA-seq dataset and in the HK-2 cells treated with the cytokines were shown as red and blue dots, respectively. Genes encoding ligands in those upregulated genes were shown as green dots and named in green characters. Representative downregulated genes of injured PT-1 were named in blue characters. (G) Representative immunofluorescence images for human transplanted kidneys from two cases. Immunofluorescence image staining for CD20 (green), CD3 ϵ (red), and DAPI (blue) displayed TLTs that consisted of aggregates of both B and T cells (left panels). Immunofluorescence images for VCAM1 (green), megalin (red), and DAPI (blue) showed VCAM1⁺ injured PTs surrounding TLTs (right panels). Scale bars=50 μm . Clinical profiles of the two cases were shown in Supplemental Table 3. (H) Magnified immunofluorescence images in the areas enclosed by rectangles in (G) staining for VCAM1 (green), megalin (red), and DAPI (blue) showed VCAM1⁺ injured PTs surrounding TLTs in human transplanted kidneys of two cases. In the same regions, immunostaining for transcription factors (p65 and pSTAT1) (brown) and megalin (pink) were shown. p65 and pSTAT1 were translocated into nuclei in the VCAM1⁺ PTs surrounding TLTs. Scale bars=50 μm . TLT borders are shown as dashed lines (A, G, and H). CD, collecting duct; CNT, connecting tubule; DCT, distal convoluted tubule; EC, endothelial cell; IC, intercalated cell; ISH, *in situ* hybridization; PB/PC, plasmablast/plasma cell; PC, principal cell; PEC, parietal epithelial cell; Prolif., proliferating; PT, proximal tubule; S1/S2, S1 segment/S2 segment; S2/S3, S2 segment/S3 segment; TAL, thick ascending limbs of the loop of Henle; tLOH, thin limbs of the loop of Henle; TLT, tertiary lymphoid tissue; VSMC, vascular smooth muscle cell.

profiles are included in Supplemental Table 3. These findings suggest that TLTs in the human kidneys may also contribute to the development of proinflammatory injured PTs surrounding them.

Phenotypic Differences between Cortical and Medullary Fibroblasts in the Sham-Treated Kidney

A subset analysis of the fibroblast clusters in the sham-treated kidney dataset (cluster 16 in Figure 1C) was performed, and 418 nuclei were classified into three clusters (Supplemental Figure 17, A and B). Cluster 1 consisted of cortical fibroblasts expressing *Dapk2*, a marker of cortical fibroblasts.⁵³ Cluster 2 was annotated as medullary fibroblasts on the basis of the high expression of *Bmpr1b*, a marker of medullary fibroblasts.¹⁴ Tenascin-C (encoded by *Tnc*), another cluster 2 marker, was intensely stained in fibroblasts in the inner medulla, as previously reported (Supplemental Figure 17, C and D).^{54,55}

snRNA-seq of the Fibroblast Subset in Aged Injured Kidneys Reveals Transcriptomics of Distinct Subpopulations, Profibrotic Fibroblasts, and Proinflammatory Fibroblasts

In the subset analysis of fibroblasts from the injured kidney dataset (cluster 12 in Figure 1D), 966 nuclei were classified into five clusters (Figure 5A). Clusters 1 and 2 were annotated as *Dapk2*⁺ cortical fibroblasts and cluster 3 as *Bmpr1b*⁺ medullary fibroblasts. In addition, two other fibroblast clusters (clusters 4 and 5) were identified. The fibroblast subpopulation with high expression of pericyte markers, such as *Cspg4* and *Mcam* (encoding NG2 and CD146, respectively),⁵⁶ was not detected possibly due to the small number of

fibroblasts (Supplemental Figure 18). Enrichment analysis of the marker genes from cluster 4 showed enrichment of GO terms related to extracellular matrix (ECM) and TGF β signaling and KEGG pathways, including focal adhesion, indicating that this cluster represented profibrotic fibroblasts (Figure 5B, Supplemental Figure 19A, Supplemental Table 7). Profibrotic fibroblasts highly expressed several genes encoding the ECM proteins, *Acta2* (encoding α SMA, a myofibroblast marker), *Tgfb*, and its receptor *Tgfr*, suggesting that their profibrotic phenotype was enhanced in an autocrine manner (Figure 5A, Supplemental Figure 20A). By contrast, enrichment analysis of marker genes from cluster 5 showed enrichment of GO terms related to the cytokine-mediated signaling pathway and IFN signaling pathway and the KEGG pathways related to inflammation, such as TNF and NF κ B signaling pathways, indicating their proinflammatory phenotype (Figure 5B, Supplemental Figure 19B, Supplemental Table 7). In the proinflammatory fibroblasts, genes encoding adhesion molecules (*Vcam1*, *Icam1*), chemokines (*Cxcl9*, *Cxcl10*, *Cxcl13*), and cytokines, including survival factors (*Tnfsf13b*, *Il15*, *Il33*), a complement (*C3*), secondary lymphoid organ (SLO) stromal markers (*Pdprn*, *Mfge8*, *Enpp2*),⁵⁷ and p75NTR (*Ngfr*, the marker for fibroblasts within TLTs),⁹ were upregulated (Figure 5A, Supplemental Figure 20B).

Subsequently, we performed gene regulatory network analysis on the fibroblast subpopulations in the IRI kidney datasets and identified several TFs that were activated in each cluster (Figure 5C, Supplemental Table 8). Among the detected TFs, *Runx1*, which induces fibroblast-to-myofibroblast transition,⁵⁸ and *Creb3l2*, which contributes to hepatic fibrosis,⁵⁹ were

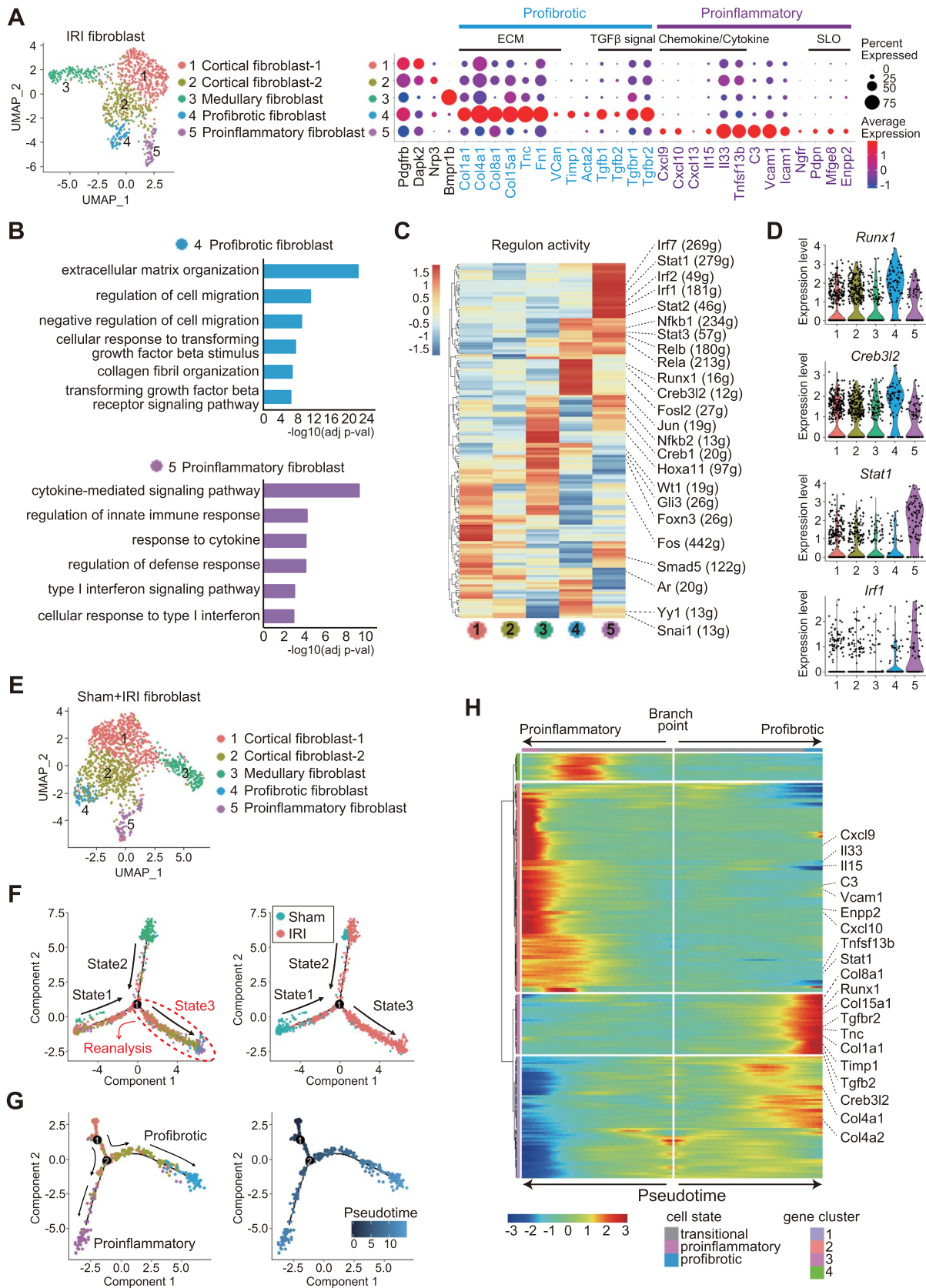


Figure 5. Analysis of fibroblasts in aged injured kidneys revealed transcriptomics of profibrotic fibroblasts and proinflammatory fibroblasts. (A) UMAP plots displaying five clusters in the fibroblast subset in the integrated IRI kidney dataset and dot plots showing

Figure 5. (Continued) expression patterns of the representative marker genes for each fibroblast cluster. The marker gene names for the profibrotic and proinflammatory fibroblast clusters are displayed in light blue and purple characters, respectively. The categories of the genes are shown above the dot plot (ECM, extracellular matrix; SLO, secondary lymphoid organ). Expression patterns of these marker genes are also shown in violin plots in [Supplemental Figure 20](#). (B) Top six GO terms significantly enriched in the profibrotic (cluster 4) and proinflammatory (cluster 5) fibroblast clusters in aged injured kidneys. Significance was shown as $-\log_{10}(\text{adjusted } P\text{-value})$. The KEGG pathways enriched in these fibroblast clusters are shown in [Supplemental Figure 19](#). (C) Gene regulatory network analysis was performed on the fibroblast clusters in aged injured kidneys. A heatmap displayed the average regulon activities in each of the five fibroblast clusters. The representative TFs were highlighted on the right of the heatmaps. The number of predicted target genes was shown following each TF's name. (D) Violin plots showing expression patterns of the selected genes encoding TFs (*Runx1*, *Creb3l2*, *Stat1*, and *Irf1*) across five fibroblast clusters. (E) UMAP plots showed that the integrated data from fibroblast subsets of sham-treated and IRI kidney datasets was classified into five clusters. (F) Pseudotime trajectory analysis was performed on the integrated fibroblast dataset using Monocle2. The trajectory plots were colored by cluster identity (left panel) and by sample type, sham (blue dots), and IRI (red dots) (right panel). All cells were divided into three cell states. States 1 and 2 were defined as the roots of fibroblast differentiation after kidney injury because they included most of the nuclei derived from the sham-treated kidney dataset. The nuclei included in the state 3 (encircled by red dashed lines) were reanalyzed (G). (G) Reanalysis of the nuclei included in the state 3 of the trajectory plots in (F). The trajectory tree bifurcated into two branches along the distinct fibroblast subtypes from the branch point (node number 2). Right trajectory plots show the pseudotime along the trajectory tree depending on the shade of blue. (H) A heatmap showing gene expression changes of the differentially expressed genes identified by branched expression analysis modeling ($q\text{-value} < 0.001$) between two fibroblast subtypes, proinflammatory, and profibrotic fibroblasts. The pseudotime starting point in the middle of the heatmap was the branch point (node number 2) in (G). Representative gene names are highlighted. IRI, ischemia-reperfusion injury; TF, transcription factor; UMAP, Uniform Manifold Approximation and Projection.

strongly expressed and activated in profibrotic fibroblasts (cluster 4) ([Figure 5, C and D](#)). By contrast, several IFN-inducible TFs (*Stat1*, *Stat2*, and *Irf1*) were specifically activated in proinflammatory fibroblasts (cluster 5) ([Figure 5, C and D](#)).

Furthermore, fibroblast datasets from sham-treated and IRI kidneys were integrated ([Figure 5E](#)), and pseudotime trajectory analysis of the integrated dataset demonstrated that most of the sham-treated kidney-derived nuclei were in states 1 and 2 of the trajectory plots ([Figure 5F](#)), indicating that the cell states shifted from these states toward state 3 after kidney injury. Subsequently, the subset in state 3 in [Figure 5F](#) was reanalyzed, resulting in two different branches for profibrotic and proinflammatory fibroblasts ([Figure 5G](#)). Branched expression analysis modeling detected significantly differentially expressed genes during differentiation into the two distinct cell types ([Supplemental Table 9](#)), and the expressional transition of these genes over pseudotime is shown in a heatmap (genes with $q\text{-value} < 0.001$) ([Figure 5H](#)). Genes encoding ECM, TGF β , and TGF β receptors were upregulated only along the branch to the profibrotic fibroblast; however, genes encoding chemokines or cytokines and SLO stromal markers were upregulated especially along the branch to the proinflammatory fibroblasts ([Figure 5H, Supplemental Figure 21, A and B](#)). The TF expression included in the activated regulons detected by gene regulatory network analysis (*Runx1*, *Creb3l2*, *Stat1*, *Stat2*, and *Irf1*) was also specifically upregulated in each fibroblast subpopulation, suggesting their association with phenotypic changes ([Supplemental Figure 21C](#)). These results show markedly different changes in gene expression between profibrotic and proinflammatory fibroblasts in aged injured kidneys.

Profibrotic Fibroblasts and Proinflammatory Fibroblasts Show Distinct Localization Outside and within TLTs

Subsequently, immunostaining and ISH were performed to localize each fibroblast subpopulation in aged injured kidneys with TLTs. Immunostaining revealed ECM (type 1 collagen, tenascin-C, and fibronectin) accumulation outside but not within TLTs ([Figure 6A](#)) and RUNX1 expression in αSMA^+ myofibroblasts around TLTs ([Figure 6B](#)), suggesting that profibrotic fibroblasts have a unique localization outside TLTs. By contrast, immunostaining demonstrated that the expression of CXCL9, CXCL10, IL33, and C3 was upregulated in fibroblasts within the TLTs ([Figure 6C](#)). ISH also revealed that *Tnfsf13b*, which encodes B cell-activating factor (BAFF), was highly expressed in fibroblasts within the TLTs ([Figure 6D](#)). SLO stromal markers, such as podoplanin and MFGE8, were also expressed in fibroblasts within the TLTs ([Figure 6E](#)). These results indicated that proinflammatory fibroblasts were localized within the TLTs. In summary, fibroblasts with distinct phenotypes have a unique localization within and outside TLTs in aged injured kidneys.

Proinflammatory Fibroblasts Contribute to Lymphocyte Recruitment, Survival, and Proliferation within TLTs via Chemokine or Cytokine Production

Ligand-receptor analysis between the proinflammatory fibroblasts and lymphocytes was conducted on the basis of their proximity within TLTs ([Supplemental Figure 5C](#)) and detected cell-cell interactions between proinflammatory fibroblasts and B cells via *Vcam1/Icam1-integrin*, *Cxcl13-Cxcr5*, and *Tnfsf13b* (BAFF)-*Tnfrsf13b* (BAFF receptor) pathways ([Figure 6F](#)). CXCL13 plays a crucial role in CXCR5 $^+$ B-cell recruitment,⁶⁰

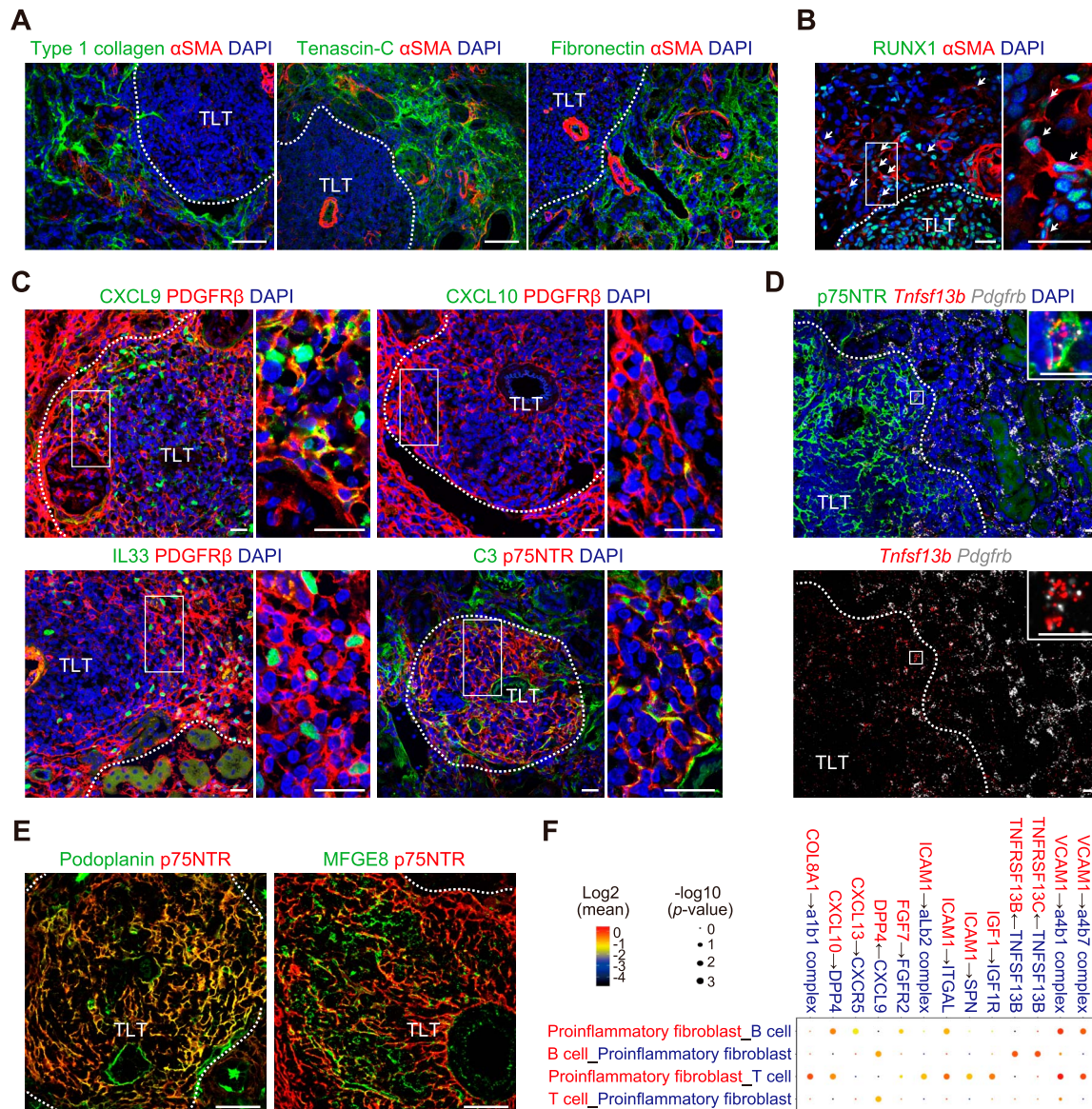


Figure 6. Distinct localization of profibrotic fibroblasts and proinflammatory fibroblasts outside and within TLTs. (A) Immunofluorescence images staining for ECM proteins (type 1 collagen, tenascin-C, and fibronectin) (green), α SMA (red), and DAPI (blue) showed that these ECM accumulated in the interstitial space outside TLTs. Scale bars=50 μ m. (B) Immunofluorescence images staining for RUNX1 (green), α SMA (red), and DAPI (blue) showed that RUNX1 was expressed in the nuclei of α SMA⁺ myofibroblasts (arrows) around TLTs in aged injured kidneys. A magnified view of the areas enclosed by a rectangle in the left panel is shown in the right panel. Scale bars=20 μ m. (C) Representative immunofluorescence images staining for the selected markers for proinflammatory fibroblasts (CXCL9, CXCL10, IL33, and C3 [green], PDGFR β [red], p75NTR [red], and DAPI [blue]) showed that these markers were expressed in the fibroblasts within TLTs. Magnified views of the area enclosed by rectangles in the left panels are shown in the right panels. Scale bars=20 μ m. (D) A combined immunofluorescence (p75NTR [green] and DAPI [blue]) and *in situ* hybridization (*Tnfsf13b* [red] and *Pdgfrb* [gray]) showed that fibroblasts within TLTs expressed *Tnfsf13b* more intensely than fibroblasts in the other area. The areas enclosed by squares are displayed in a magnified view in the upper right of the panels, and they show that *Tnfsf13b* and *Pdgfrb* are expressed in the same p75NTR⁺ fibroblast. Scale bars=10 μ m. (E) Immunofluorescence images staining for markers of secondary lymphoid organ stromal cells (podoplanin and MFGE8) (green) and p75NTR (red) in TLTs. Podoplanin and MFGE8 expression merged with p75NTR expression in the fibroblasts within TLTs. Scale bars=50 μ m. (F) A heatmap showing selected ligand-receptor interactions between the proinflammatory fibroblasts and lymphocytes (T and B cells) in aged injured kidneys. The cell type color (red or blue) corresponds to the colors of the ligands and receptors expressed by the cell types. In the ligand-receptor pair name, the molecule at the root of the arrow is a ligand and the molecule at the arrowhead is a receptor. The dot size indicates $-\log_{10}(P\text{-value})$ calculated using CellPhoneDB, and the dot color indicates the log scaled mean expression of the ligand and receptor. TLT borders are shown as dashed lines (A–E). ECM, extracellular matrix; TLT, tertiary lymphoid tissue.

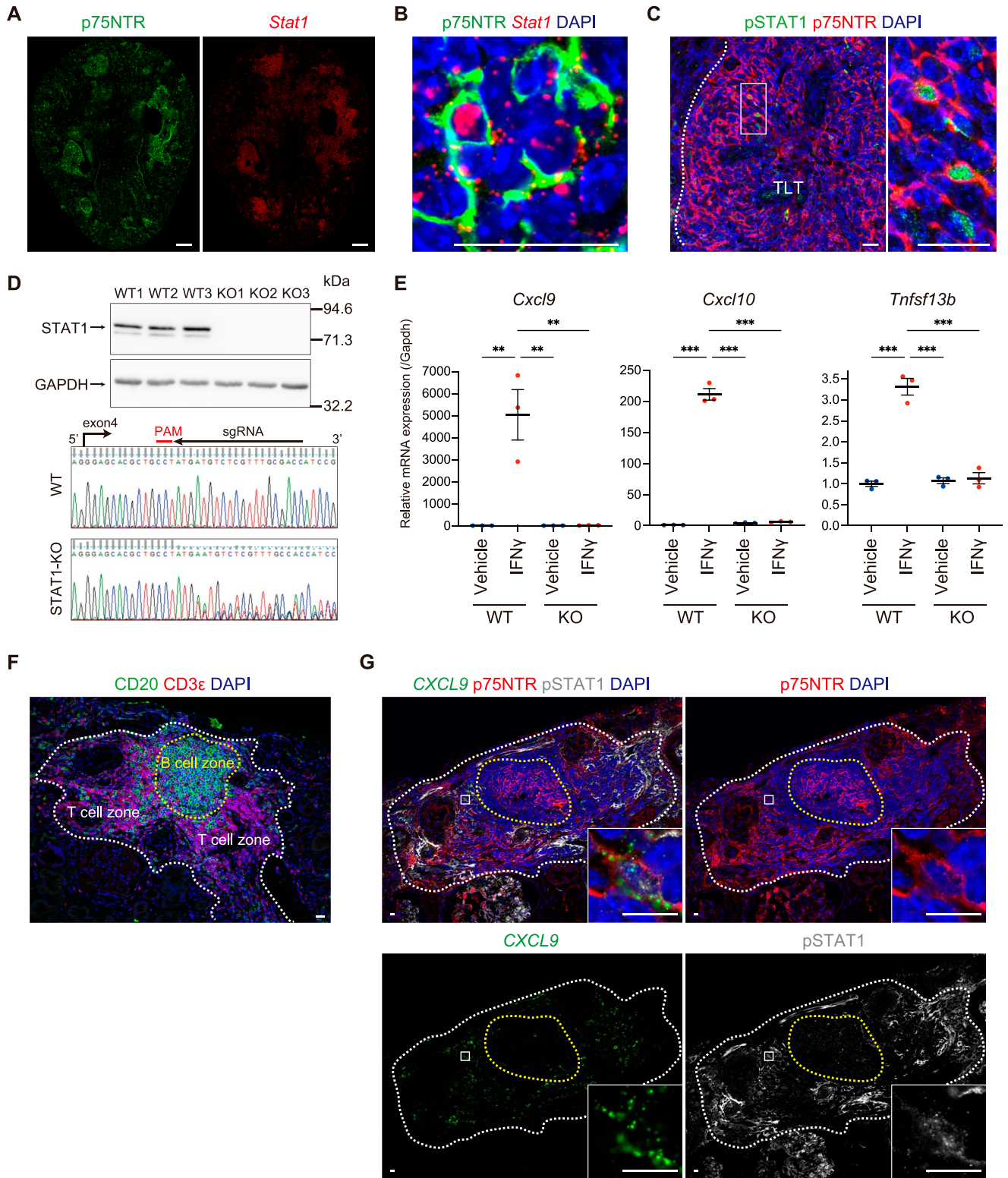


Figure 7. IFN γ /STAT1 signaling potentially promotes the proinflammatory phenotype of the fibroblasts within TLTs in murine and human kidneys. (A, B) A combination of immunofluorescence (p75NTR [green]) and ISH (*Stat1* [red]) showed high *Stat1* expression within TLT areas indicated by the presence of p75NTR⁺ fibroblasts (A) in low magnification in murine aged injured kidneys (Scale bars=300 μ m). (B) The magnified image within TLTs showed that p75NTR⁺ fibroblasts expressed *Stat1* (Scale bars=20 μ m). (C) Immunofluorescence images staining for pSTAT1 (green), p75NTR (red), and DAPI (blue) showed that pSTAT1 was expressed in the nuclei of the fibroblasts within TLTs in murine aged injured kidneys. TLT borders are displayed as dashed lines. A magnified view

Figure 7. (Continued) of the areas enclosed by a rectangle in the left panel is shown in the right panel. Scale bars=20 μm . (D) Western blotting for STAT1 and GAPDH in WT and STAT1 KO C3H10T1/2 cells showed complete loss of STAT1 protein in all KO cells. Sanger sequences for a part of *Stat1* exon4 in representative WT cells and STAT1-KO cells showed double peaks starting from the downstream of PAM sequence only in STAT1-KO cells, indicating successful DNA deletions at the target sequence (red line, PAM sequence; black arrow, sgRNA sequence). (E) Representative relative *Cxcl9*, *Cxcl10*, and *Tnfsf13b* mRNA expression levels in WT and STAT1-KO C3H10T1/2 treated with vehicle or IFN γ for 24 hours ($n=3/\text{group}$). The expression levels were normalized to those of *Gapdh*. Values are shown as the mean \pm SEM. Statistical significance was determined using a one-way ANOVA followed by the Tukey-Kramer *post hoc* test (** $P < 0.01$, *** $P < 0.001$). (F) Immunofluorescence images of TLTs in a human transplanted kidney (Case 1 in Supplemental Table 3). The immunofluorescence image staining for CD20 (green), CD3 ϵ (red), and DAPI (blue) displayed the B-cell zone (encircled by yellow dashed lines) and the T-cell zone in the TLT surrounded by white dashed lines. Scale bars=20 μm . (G) A combination of immunofluorescence (p75NTR [red], pSTAT1 [gray], and DAPI [blue]) and ISH (CXCL9 [green]) showed high CXCL9 and pSTAT1 expression in the T-cell zone outside the B-cell zone (encircled by yellow dashed lines) in TLTs (encircled by white dashed lines) in the human transplanted kidney. The area enclosed by a solid square is magnified at the right lower bottom of each image, showing a p75NTR $^{+}$ fibroblast expressing CXCL9 with pSTAT1 nuclear translocation. Scale bars=10 μm . ISH, *in situ* hybridization; KO, knockout; PAM, protospacer adjacent motif; WT, wild type.

and BAFF contributes to B-cell survival and proliferation,^{61,62} indicating that proinflammatory fibroblasts within TLTs contribute to B-cell recruitment, retention, survival, and proliferation. In addition, cell-cell interactions could occur between proinflammatory fibroblasts and T cells *via* the CXCL9/CXCL10-CXCR3 pathway, which contributes to T-cell recruitment and retention on the basis of CXCL9/CXCL10 expression in fibroblasts within TLTs and CXCR3 expression in T cells (Supplemental Figure 11B).^{10,51,52} Furthermore, aged injured kidneys with TLTs 30 days after 18-minutes IRI showed higher gene expression of the chemokines and cytokines expressed by the proinflammatory fibroblasts than young injured kidneys (Supplemental Figure 22), indicating that TLTs potentially promote inflammation *via* abovementioned cell-cell interactions uniquely in aged injured kidneys.

IFN γ /STAT1 Signaling Potentially Promotes the Proinflammatory Phenotype of Fibroblasts within TLTs in Murine and Human Kidneys

We focused on STAT1 as a TF associated with the proinflammatory phenotype of fibroblasts within TLTs because gene regulatory network analysis showed that the *Stat1* regulon was activated specifically in proinflammatory fibroblasts. Consistently, ISH demonstrated strong *Stat1* expression in fibroblasts within TLTs (Figure 7, A and B), and immunostaining showed pSTAT1 nuclear translocation in fibroblasts within TLTs (Figure 7C).

Subsequently, we used cultured fibroblasts and found that *Cxcl9*, *Cxcl10*, and *Tnfsf13b* upregulation by IFN γ was abolished in STAT1-KO fibroblasts (Figure 7, D and E), indicating that IFN γ /STAT1 signaling promotes the proinflammatory phenotype of fibroblasts. As shown by scRNA-seq,¹⁰ *Cxcr3* $^{+}$ T cells highly expressed *Ifng* (Supplemental Figure 11, B and D). Therefore, CXCR3 $^{+}$ T cells may upregulate CXCL9/CXCL10 production by fibroblasts within TLTs *via* IFN γ production, leading to further T-cell recruitment.

In TLTs in human transplanted kidneys, p75NTR $^{+}$ fibroblasts expressing *Cxcl9* with pSTAT1 nuclear translocation

were detected in the T-cell zones (Figure 7, F and G). This finding indicates that proinflammatory fibroblasts with activated STAT1 and proinflammatory chemokine production also exist within human TLTs, contributing to TLT maintenance and expansion in human kidneys.

DISCUSSION

Here, we characterized heterogeneous cell populations among renal parenchymal cells in aged injured kidneys with TLTs and identified proinflammatory PT cells and fibroblasts. Bidirectional interactions between these proinflammatory renal parenchymal cells and immune cells within and outside TLTs have the potential to promote inflammation, TLT expansion, and kidney injury.

VCAM1 $^{+}$ PT cells were recently reported as failed repair PTs or late injured PTs with proinflammatory and profibrotic phenotypes.^{14,15} To the best of our knowledge, we, for the first time, demonstrated unique localization of VCAM1 $^{+}$ injured PTs surrounding TLTs and the potential contribution of TLTs to their proinflammatory phenotypes *via* cytokine production. Previous studies indicated that NF κ B might contribute to the maintenance of VCAM1 $^{+}$ PTs in both mice and humans.^{14,63} Our study demonstrated that NF κ B, as well as IFN-inducible TFs, such as STAT1 and IRF1, were activated in VCAM1 $^{+}$ PTs around TLTs. Furthermore, IFN γ and TNF α synergistically induced adhesive and proinflammatory phenotypes in cultured PT cells, suggesting that these cytokines, which are excessively produced by lymphocytes within TLTs, may directly promote the proinflammatory phenotype of VCAM1 $^{+}$ PTs surrounding TLTs. Several previous reports showing the direct cytotoxic effects of TNF α and IFN γ suggest that these cytokines may also directly induce maladaptive repair and phenotypic changes in PT cells surrounding TLTs.^{64–66} Conversely, these proinflammatory VCAM1 $^{+}$ PTs have the potential to recruit, retain, and activate immune cells *via* various cytokine or chemokine production, increasing inflammation and expanding TLTs (Figure 8A).

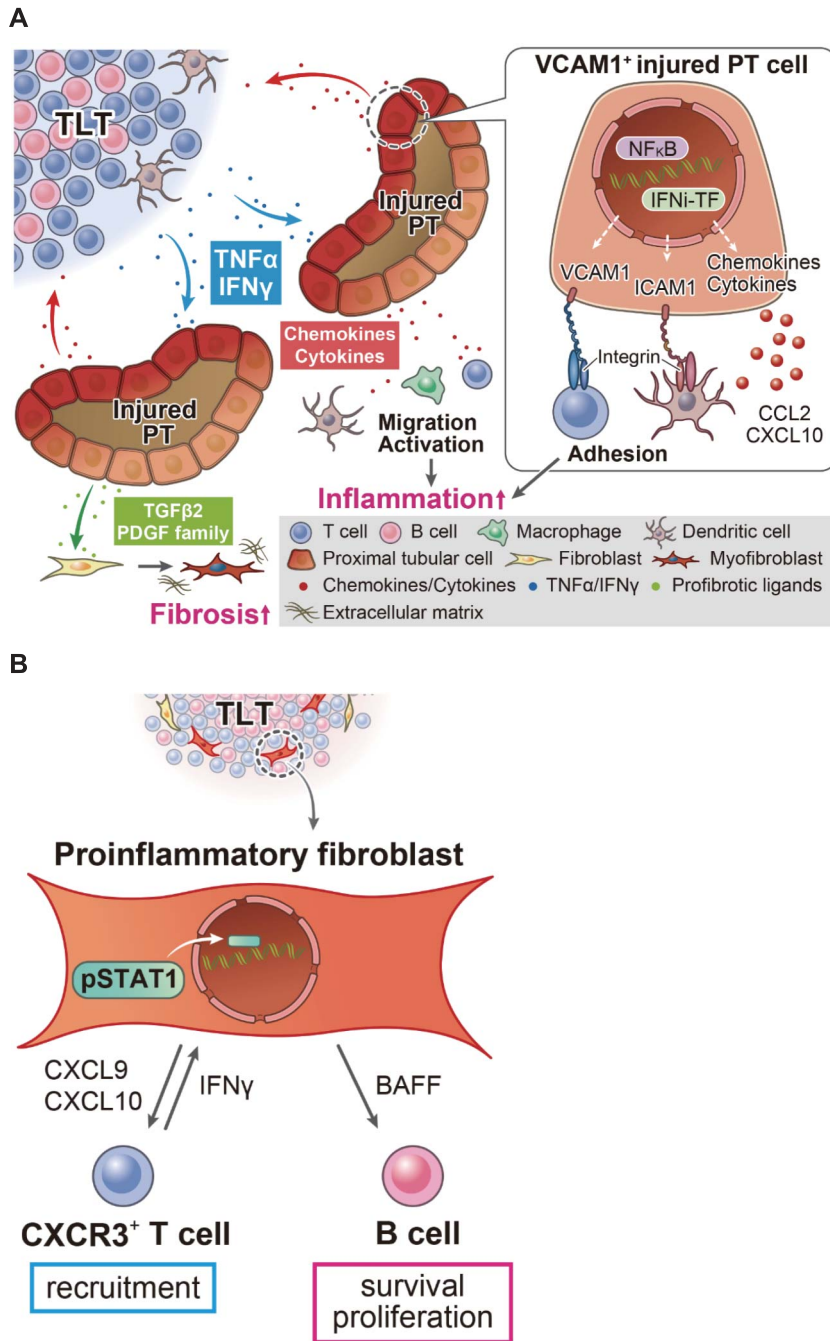


Figure 8. Schemes showing cell-cell interactions between immune cells and renal parenchymal cells in aged injured kidneys with TLTs. (A) A scheme showing cell-cell interactions between PT cells and immune cells in the microenvironment around TLTs. VCAM1⁺ injured PTs are preferentially localized around TLTs. Proinflammatory cytokines, TNF α and IFN γ , are excessively produced by immune cells within TLTs and potentially promote the adhesive and proinflammatory phenotype of the surrounding PT cells. These VCAM1⁺ injured PT cells with activated NF κ B and IFN γ -inducible transcription factors recruit and activate macrophages and dendritic and T cells via the production of proinflammatory cytokines or chemokines, such as CCL2 and CXCL10, which may further promote inflammation and TLT expansion. VCAM1⁺ injured PTs further activate fibroblasts via TGF β 2 and PDGF production, resulting in fibrosis around TLTs. (B) A scheme showing the interactions between proinflammatory fibroblasts and lymphocytes within TLTs. IFN γ produced by CXCR3⁺ T cells promotes the proinflammatory phenotype of the fibroblasts within TLTs in a STAT1-dependent manner. The STAT1-activated fibroblasts contribute to CXCR3⁺ T-cell recruitment and retention by producing CXCL9 and CXCL10 and also contribute to B-cell survival and proliferation by producing B cell-activating factor. These interactions further promote TLT expansion. PT, proximal tubule; TLT, tertiary lymphoid tissue.

Subset analysis of fibroblasts revealed heterogeneous subpopulations, including proinflammatory and profibrotic fibroblasts, which reside within and outside TLTs, respectively, in aged injured kidneys. Our study demonstrated that proinflammatory fibroblasts within TLTs could contribute to the recruitment, retention, survival, and proliferation of lymphocytes *via* cytokine or chemokine production. Subsequently, we found that IFN- γ -inducible TFs, including STAT1, were highly activated in proinflammatory fibroblasts within TLTs in murine and human kidneys. These results and our *in vitro* experiments suggest that IFN γ may promote the proinflammatory phenotype of fibroblasts within TLTs in a STAT1-dependent manner. Previous reports have demonstrated that IFN γ -responsive fibroblasts drive the pathology of murine vitiligo through the recruitment of CD8⁺ T cells *via* the production of CXCL9 and CXCL10⁶⁷ and that STAT1 was identified as a master regulator in fibroblast-like synoviocytes from patients with rheumatoid arthritis.⁶⁸ These findings support the important role of IFN γ /STAT1 signaling in determining fibroblast phenotypes. In addition, reanalysis of our previous scRNA-seq data showed high *Ifng* expression in *Cxcr3*⁺ T cells,¹⁰ which may increase CXCL9/CXCL10 and BAFF production by proinflammatory fibroblasts within TLTs *via* IFN γ production. The proinflammatory loop between T cells and fibroblasts within TLTs may contribute to TLT expansion in the kidneys (Figure 8B).

Treatments targeting TLT-associated proinflammatory pathways in aged injured kidneys remain to be developed. Our study suggests that anti-TNF α agents, such as etanercept, adalimumab, and infliximab⁶⁹ and IFN γ /STAT1 signaling pathway inhibitor, including Janus kinase 1/Janus kinase 2 inhibitors, such as baricitinib and ruxolitinib,^{70,71} may have the potential to prevent progressive injury and TLT expansion in aged injured kidneys *via* reducing the effects of these cytokines produced within TLTs on renal parenchymal cells. However, further studies are needed to confirm the effect of these drugs.

Our study had some limitations. We classified TLT-associated proinflammatory fibroblasts into a single population. However, TLT-associated fibroblasts may comprise heterogeneous subpopulations with distinct functions^{9,72}; further analysis is warranted to reveal their heterogeneity. Another limitation is posed by the low sensitivity of snRNA-seq for immune cells.⁴⁸ We used snRNA-seq because it is better suited for fibroblast analyses.²⁶ Therefore, for immune cell analysis, we reanalyzed the scRNA-seq data used in our previous study to support the present data.¹⁰ In addition, we did not detect endothelial cell subtypes with proinflammatory phenotypes in the IRI kidneys possibly due to their small number (data not shown). However, endothelial cells were recently reported to play important roles in TLT formation,⁷³ and additional studies are needed to elucidate their contributions to TLT formation in aged injured kidneys. Furthermore, lack of time-course assessment of TLTs may limit the conclusion that they amplify inflammation and contribute to maladaptive repair

for a long duration. For instance, regulatory TLTs, which are called regulatory T cell-rich organized lymphoid structures, were reported to contribute to allograft acceptance in the animal kidney transplantation model,⁷⁴ suggesting the context-dependent pathogenicity of TLTs.⁷⁵

In conclusion, TLTs potentially promote the proinflammatory phenotypes of PT cells and fibroblasts by producing proinflammatory cytokines in aged injured kidneys. Conversely, proinflammatory parenchymal cells exacerbate inflammation by recruiting and activating immune cells. TLTs have the potential to function as inflammation amplifiers in aged injured kidneys by providing microenvironments that allow renal parenchymal and immune cells to interact with each other intensely. Targeting these interactions may inhibit TLT expansion and attenuate inflammation, leading to an improved renal prognosis.

DISCLOSURES

T. Kobayashi reports Consultancy: Astellas Pharma, Janssen Pharma; Research Funding: Astellas Pharma, Chugai Pharmaceutical, MSD; and Honoraria: Astellas Pharma, Bayer, Janssen Pharma, and MSD. Y. Murakawa reports the following: Employer: RIKEN; Ownership Interest: Revorf; and Research Funding: K.K. DNAFORM, and Revorf. Y. Sato reports Employer: Mitsubishi Tanabe Pharmaceutical company. M. Yanagita received research grants from Boehringer Ingelheim and Mitsubishi Tanabe Pharma. M. Yanagita also reports Honoraria: Astellas, Chugai, Kyowa Kirin, and others for lecture honoraria; and Speakers Bureau: AstraZeneca, Astellas, Kyowa Kirin, and others for lecture honoraria. T. Yoshikawa reports Honoraria: Kyowa Kirin. All remaining authors have nothing to disclose.

FUNDING

This research was supported by the Japan Agency for Medical Research and Development (AMED) under Grant Number AMED-CREST 22ek0310020, 22gm1210009, 22zf0127003, 21gm5010002, and 21lm0203006; and the Japan Society for the Promotion of Science under KAKENHI Grant-in-Aids for Scientific Research B (20H03697).

ACKNOWLEDGMENTS

We would like to thank Professor Osamu Takeuchi at Kyoto University for providing pX330-GFP plasmids. We also thank Professor Seishi Ogawa at Kyoto University for allowing us to use their machines for snRNA-seq and Dr. Yuhei Kirita and Professor Benjamin D. Humphreys at Washington University School of Medicine for their valuable advice on snRNA-seq analysis. Additionally, we thank the Single-Cell Genome Information Analysis Core (SignAC) at WPI-ASHBi, Kyoto University, for their support. This work was partly supported by the World Premier International Research Center Initiative (WPI), MEXT, Japan. Part of this work appeared as an abstract at the annual meeting of the American Society of Nephrology.

AUTHOR CONTRIBUTIONS

Conceptualization: Yuki Sato, Motoko Yanagita, Takahisa Yoshikawa.

Data curation: Motoko Yanagita.

Formal analysis: Yasuhiro Murakawa, Akiko Oguchi, Satoko Sakurai, Naoya Toriu, Takuya Yamamoto, Motoko Yanagita, Takahisa Yoshikawa.

Funding acquisition: Motoko Yanagita.

Investigation: Naoya Toriu, Takahisa Yoshikawa.

Project administration: Motoko Yanagita.

Resources: Takashi Kobayashi, Osamu Ogawa, Hironori Haga.

Supervision: Motoko Yanagita.

Visualization: Naoya Toriu, Motoko Yanagita, Takahisa Yoshikawa.

Writing – original draft: Yuki Sato, Takahisa Yoshikawa.

Writing – review & editing: Motoko Yanagita.

DATA SHARING STATEMENT

The snRNA-seq data in this study are available in the DNA Data Bank of Japan (DDBJ) Sequence Read Archive (DRA; <https://www.ddbj.nig.ac.jp/dra/index-e.html>) under accession number DRA015783. The raw and filtered feature barcode matrix files generated by Cell Ranger are available in the DDBJ Gene Expression Archive (GEA; <https://www.ddbj.nig.ac.jp/gea/index-e.html>) under accession number E-GEAD-595. Bulk RNA-sequencing data of HK-2 cells are available in DRA under accession number DRA016510.

SUPPLEMENTAL MATERIAL

This article contains the following supplemental material online at <http://links.lww.com/JSN/E477>, <http://links.lww.com/JSN/E478>, <http://links.lww.com/JSN/E479>, <http://links.lww.com/JSN/E480>, <http://links.lww.com/JSN/E481>, <http://links.lww.com/JSN/E489>, <http://links.lww.com/JSN/E482>, <http://links.lww.com/JSN/E483>, <http://links.lww.com/JSN/E484>, <http://links.lww.com/JSN/E485>, <http://links.lww.com/JSN/E486>.

Supplemental Methods

Supplemental Figure 1. Workflow of computational analysis for each dataset.

Supplemental Figure 2. Analysis on each dataset of the three ischemia-reperfusion injury (IRI) kidneys.

Supplemental Figure 3. Representative images used to count VCAM1⁺ or KIM1⁺ proximal tubular (PT) cells in injured kidneys.

Supplemental Figure 4. Sanger sequence analysis of off-targets of wild-type and STAT1-KO C3H10T1/2 cells.

Supplemental Figure 5. Histology of mouse kidneys 30 days after sham surgery and 45-minute IRI.

Supplemental Figure 6. Expression patterns of well-known marker genes across immune cells in the IRI kidneys.

Supplemental Figure 7. Injured distal nephrons with upregulated *Lcn2* expression in the IRI kidneys.

Supplemental Figure 8. Enrichment analysis of the reclustered PT clusters in the IRI kidney dataset.

Supplemental Figure 9. Expression patterns of the genes encoding ligands highly expressed in the injured PT-1 across the four PT clusters.

Supplemental Figure 10. Pearson correlation analysis between the injured PT-1 in our analysis and PT subpopulations in previous publication.

Supplemental Figure 11. Expression patterns of *Cxcr3*, *Tnf*, and *Ifng* in immune cells in aged injured kidneys with tertiary lymphoid tissues (TLTs) on the basis of single-cell RNA-sequencing dataset.

Supplemental Figure 12. Trajectory analysis of PT subsets.

Supplemental Figure 13. Histology of aged injured kidneys 30 days after 18-minute mild IRI.

Supplemental Figure 14. Comparison of the expression of injured PT markers between aged and young injured kidneys.

Supplemental Figure 15. Immunofluorescence images for transcription factors, p65 and STAT1, in aged injured kidneys with TLTs.

Supplemental Figure 16. *In situ* hybridization images showing high *Stat1* expression within TLTs and their surroundings.

Supplemental Figure 17. Analysis of fibroblasts in the sham-treated kidney.

Supplemental Figure 18. Expression levels of pericyte markers across fibroblast subpopulations in the IRI kidney dataset.

Supplemental Figure 19. KEGG pathways enriched in the fibroblast subpopulations in aged injured kidneys.

Supplemental Figure 20. Expression patterns of selected marker genes from the profibrotic and proinflammatory fibroblasts in aged injured kidneys.

Supplemental Figure 21. Gene expression kinetics during fibroblast differentiation in aged injured kidneys was determined using pseudotime trajectory analysis.

Supplemental Figure 22. Comparison of the expression of proinflammatory fibroblast markers between aged and young injured kidneys.

Supplemental Table 1. Marker gene lists for each dataset (Excel).

Supplemental Table 2. Parameters and the number of nuclei used in the analysis (Excel).

Supplemental Table 3. Clinical profiles of two cases after kidney transplantation (Excel).

Supplemental Table 4. Enrichment analysis results for PT clusters in aged injured kidneys (Excel).

Supplemental Table 5. Regulon activity across the PT clusters in aged injured kidneys (Excel).

Supplemental Table 6. Differentially expressed genes (DEG) lists of HK-2 cells treated with vehicle, TNF α , and IFN γ (Excel).

Supplemental Table 7. Enrichment analysis results for fibroblast clusters in aged injured kidneys (Excel).

Supplemental Table 8. Regulon activity across the fibroblast clusters in aged injured kidneys (Excel).

Supplemental Table 9. Result of branched expression analysis modeling (BEAM) analysis on the fibroblast subset in aged injured kidneys (Excel).

Supplemental Table 10. Primers for quantitative real-time PCR (Excel).

References for Supplemental Information

REFERENCES

- Luo S, Zhu R, Yu T, Fan H, Hu Y, Mohanta SK. Chronic inflammation: a common promoter in tertiary lymphoid organ neogenesis. *Front Immunol.* 2019;10:2938. doi:10.3389/fimmu.2019.02938
- Bombardieri M, Lewis M, Pitzalis C. Ectopic lymphoid neogenesis in rheumatic autoimmune diseases. *Nat Rev Rheumatol.* 2017;13(3):141–154. doi:10.1038/nrrheum.2016.217
- Sautès-Fridman C, Petitprez F, Calderaro J, Fridman WH. Tertiary lymphoid structures in the era of cancer immunotherapy. *Nat Rev Cancer.* 2019;19(6):307–325. doi:10.1038/s41568-019-0144-6
- Sato Y, Tamura M, Yanagita M. Tertiary lymphoid tissues: a regional hub for kidney inflammation. *Nephrol Dial Transplant.* 2021;38(1):26–33. doi:10.1093/ndt/gfab212
- Sarwal M, Chua MS, Kambham N, Hsieh SC, Satterwhite T, Masek M. Molecular heterogeneity in acute renal allograft rejection identified by DNA microarray profiling. *N Engl J Med.* 2003;349(2):125–138. doi:10.1056/NEJMoa035588
- Lee YH, Sato Y, Saito M, Fukuma S, Saito M, Yamamoto S. Advanced tertiary lymphoid tissues in protocol biopsies are associated with progressive graft dysfunction in kidney transplant recipients. *J Am Soc Nephrol.* 2022;33(1):186–200. doi:10.1681/ASN.2021050715
- Pei G, Zeng R, Han M, Liao P, Zhou X, Li Y. Renal interstitial infiltration and tertiary lymphoid organ neogenesis in IgA nephropathy. *Clin J Am Soc Nephrol.* 2014;9(2):255–264. doi:10.2215/CJN.01150113
- Shen Y, Sun CY, Wu FX, Chen Y, Dai M, Yan YC. Association of intrarenal B-Cell infiltrates with clinical outcome in lupus nephritis: a study of 192 cases. *Clin Dev Immunol.* 2012;2012:967584. doi:10.1155/2012/967584

9. Sato Y, Mii A, Hamazaki Y, Fujita H, Nakata H, Masuda K. Heterogeneous fibroblasts underlie age-dependent tertiary lymphoid tissues in the kidney. *JCI Insight*. 2016;1(11):e87680. doi:10.1172/jci.insight.87680
10. Sato Y, Oguchi A, Fukushima Y, Masuda K, Torii N, Taniguchi K. CD153/CD30 signaling promotes age-dependent tertiary lymphoid tissue expansion and kidney injury. *J Clin Invest*. 2022;132(2):e146071. doi:10.1172/JCI146071
11. Park J, Shrestha R, Qiu C, Kondo A, Huang S, Werth M. Single-cell transcriptomics of the mouse kidney reveals potential cellular targets of kidney disease. *Science*. 2018;360(6390):758–763. doi:10.1126/science.aar2131
12. Kuppe C, Ibrahim MM, Kranz J, Zhang X, Ziegler S, Perales-Patón J. Decoding myofibroblast origins in human kidney fibrosis. *Nature*. 2021;589(7841):281–286. doi:10.1038/s41586-020-2941-1
13. Dumas SJ, Meta E, Borri M, Goveia J, Rohlenova K, Concinha NV. Single-cell RNA sequencing reveals renal endothelium heterogeneity and metabolic adaptation to water deprivation. *J Am Soc Nephrol*. 2020;31(1):118–138. doi:10.1681/ASN.2019080832
14. Kirita Y, Wu H, Uchimura K, Wilson PC, Humphreys BD. Cell profiling of mouse acute kidney injury reveals conserved cellular responses to injury. *Proc Natl Acad Sci U S A*. 2020;117(27):15874–15883. doi:10.1073/pnas.2005477117
15. Gerhardt LMS, Liu J, Koppitch K, Cippà PE, McMahon AP. Single-nuclear transcriptomics reveals diversity of proximal tubule cell states in a dynamic response to acute kidney injury. *Proc Natl Acad Sci U S A*. 2021;118(27):e2026684118. doi:10.1073/pnas.2026684118
16. Sato Y, Boor P, Fukuma S, et al. Developmental stages of tertiary lymphoid tissue reflect local injury and inflammation in mouse and human kidneys. *Kidney Int*. 2020;98:448–463. doi:10.1016/j.kint.2020.02.023
17. Stuart T, Butler A, Hoffman P, Hafemeister C, Papalexi E, Mauck WM. Comprehensive integration of single-cell data. *Cell*. 2019;177(7):1888–1902.e21. doi:10.1016/j.cell.2019.05.031
18. McGinnis CS, Murrow LM, Gartner ZJ. DoubletFinder: doublet detection in single-cell RNA sequencing data using artificial nearest neighbors. *Cell Syst*. 2019;8(4):329–337.e4. doi:10.1016/j.cels.2019.03.003
19. Young MD, Behjati S. SoupX removes ambient RNA contamination from droplet-based single-cell RNA sequencing data. *Gigascience*. 2020;9(12):giaa151. doi:10.1093/gigascience/giaa151
20. Chen L, Clark JZ, Nelson JW, Kaissling B, Ellison DH, Knepper MA. Renal-tubule epithelial cell nomenclature for single-cell RNA-sequencing studies. *J Am Soc Nephrol*. 2019;30(8):1358–1364. doi:10.1681/ASN.2019040415
21. Rogers NM, Ferenbach DA, Isenberg JS, Thomson AW, Hughes J. Dendritic cells and macrophages in the kidney: a spectrum of good and evil. *Nat Rev Nephrol*. 2014;10(11):625–643. doi:10.1038/nmeph.2014.170
22. Zimmerman KA, Bentley MR, Lever JM, Li Z, Crossman DK, Song CJ. Single-cell RNA sequencing identifies candidate renal resident macrophage gene expression signatures across species. *J Am Soc Nephrol*. 2019;30(5):767–781. doi:10.1681/ASN.2018090931
23. Elyahu Y, Hekselman I, Eizenberg-Magar I, Berner O, Strominger I, Schiller M. Aging promotes reorganization of the CD4 T cell landscape toward extreme regulatory and effector phenotypes. *Sci Adv*. 2019;5(8):eaaw8330. doi:10.1126/sciadv.aaw8330
24. Suan D, Sundling C, Brink R. Plasma cell and memory B cell differentiation from the germinal center. *Curr Opin Immunol*. 2017;45:97–102. doi:10.1016/j.coi.2017.03.006
25. Ransick A, Lindström NO, Liu J, Zhu Q, Guo JJ, Alvarado GF. Single-cell profiling reveals sex, lineage, and regional diversity in the mouse kidney. *Dev Cell*. 2019;51(3):399–413.e7. doi:10.1016/j.devcel.2019.10.005
26. Wu H, Kirita Y, Donnelly EL, Humphreys BD. Advantages of single-nucleus over single-cell RNA sequencing of adult kidney: rare cell types and novel cell states revealed in fibrosis. *J Am Soc Nephrol*. 2019;30(1):23–32. doi:10.1681/ASN.2018090912
27. Ramilowski JA, Goldberg T, Harshbarger J, Kloppmann E, Lizio M, Satagopam VP. A draft network of ligand-receptor-mediated multicellular signalling in human. *Nat Commun*. 2015;6(1):7866. doi:10.1038/ncomms8866
28. Efreanova M, Vento-Tormo M, Teichmann SA, Vento-Tormo R. Cell-PhoneDB: inferring cell–cell communication from combined expression of multi-subunit ligand–receptor complexes. *Nat Protoc*. 2020;15(4):1484–1506. doi:10.1038/s41596-020-0292-x
29. Aibar S, González-Blas CB, Moerman T, Huynh-Thu VA, Imrichova H, Hulselmans G. SCENIC: single-cell regulatory network inference and clustering. *Nat Methods*. 2017;14(11):1083–1086. doi:10.1038/nmeth.4463
30. Qiu X, Hill A, Packer J, Lin D, Ma YA, Trapnell C. Single-cell mRNA quantification and differential analysis with Census. *Nat Methods*. 2017;14(3):309–315. doi:10.1038/nmeth.4150
31. Chen EY, Tan CM, Kou Y, Duan Q, Wang Z, Meirelles GV. Enrichr: interactive and collaborative HTML5 gene list enrichment analysis tool. *BMC Bioinform*. 2013;14(1):128. doi:10.1186/1471-2105-14-128
32. Kuleshov MV, Jones MR, Rouillard AD, Fernandez NF, Duan Q, Wang Z. Enrichr: a comprehensive gene set enrichment analysis web server 2016 update. *Nucleic Acids Res*. 2016;44(W1):W90–W97. doi:10.1093/nar/gkw377
33. Xie Z, Bailey A, Kuleshov MV, Clarke DJB, Evangelista JE, Jenkins SL. Gene set knowledge discovery with Enrichr. *Curr Protoc*. 2021;1(3):e90. doi:10.1002/cpz.1.90
34. Kanehisa M, Goto S. KEGG: kyoto encyclopedia of genes and genomes. *Nucleic Acids Res*. 2000;28(1):27–30. doi:10.1093/nar/28.1.27
35. Kanehisa M, Furumichi M, Sato Y, Ishiguro-Watanabe M, Tanabe M. KEGG: integrating viruses and cellular organisms. *Nucleic Acids Res*. 2021;49(D1):D545–D551. doi:10.1093/nar/gkaa970
36. Ashburner M, Ball CA, Blake JA, Botstein D, Butler H, Cherry JM. Gene Ontology: tool for the unification of biology. *Nat Genet*. 2000;25(1):25–29. doi:10.1038/75556
37. Carbon S, Douglass E, Good BM, et al. The Gene Ontology resource: enriching a GOld mine. *Nucleic Acids Res*. 2021;49(D1):D325–D334. doi:10.1093/nar/gkaa1113
38. Dobin A, Davis CA, Schlesinger F, Drenkow J, Zaleski C, Jha S. STAR: ultrafast universal RNA-seq aligner. *Bioinformatics*. 2013;29(1):15–21. doi:10.1093/bioinformatics/bts635
39. Li B, Dewey CN. RSEM: accurate transcript quantification from RNA-Seq data with or without a reference genome. *BMC Bioinform*. 2011;12(1):323. doi:10.1186/1471-2105-12-323
40. Love MI, Huber W, Anders S. Moderated estimation of fold change and dispersion for RNA-seq data with DESeq2. *Genome Biol*. 2014;15(12):550. doi:10.1186/s13059-014-0550-8
41. Mashiko D, Fujihara Y, Satouh Y, Miyata H, Isotani A, Ikawa M. Generation of mutant mice by pronuclear injection of circular plasmid expressing Cas9 and single guided RNA. *Sci Rep*. 2013;3(1):3355. doi:10.1038/srep03355
42. Concordat JP, Haeussler M. CRISPOR: intuitive guide selection for CRISPR/Cas9 genome editing experiments and screens. *Nucleic Acids Res*. 2018;46(W1):W242–W245. doi:10.1093/nar/gky354
43. Sun T, Huang Z, Liang WC, Yin J, Lin WY, Wu J. TGFβ2 and TGFβ3 isoforms drive fibrotic disease pathogenesis. *Sci Transl Med*. 2021;13(605):eabe0407. doi:10.1126/scitranslmed.abe0407
44. Tang WW, Ulich TR, Lacey DL, Hill DC, Qi M, Kaufman SA. Platelet-derived growth factor-BB induces renal tubulointerstitial myofibroblast formation and tubulointerstitial fibrosis. *Am J Pathol*. 1996;148(4):1169–1180. PMID: 8644858.
45. Buhl EM, Djurdjaj S, Babickova J, Klinkhammer BM, Folestad E, Borkham-Kamphorst E. The role of PDGF-D in healthy and fibrotic kidneys. *Kidney Int*. 2016;89(4):848–861. doi:10.1016/j.kint.2015.12.037
46. Xu L, Sharkey D, Cantley LG. Tubular GM-CSF promotes late MCP-1/CCR2-mediated fibrosis and inflammation after ischemia/reperfusion injury. *J Am Soc Nephrol*. 2019;30(10):1825–1840. doi:10.1681/ASN.2019010068
47. Matloubian M, David A, Engel S, Ryan JE, Cyster JG. A transmembrane CXC chemokine is a ligand for HIV-coreceptor Bonzo. *Nat Immunol*. 2000;1(4):298–304. doi:10.1038/79738

48. O'Sullivan ED, Mylonas KJ, Hughes J, Ferenbach DA. Complementary roles for single-nucleus and single-cell RNA sequencing in kidney disease research. *J Am Soc Nephrol*. 2019;30(4):712–713. doi:10.1681/ASN.2019020112
49. Panzer U, Steinmetz OM, Reinking RR, Meyer TN, Fehr S, Schneider A. Compartment-specific expression and function of the chemokine IP-10/CXCL10 in a model of renal endothelial microvascular injury. *J Am Soc Nephrol*. 2006;17(2):454–464. doi:10.1681/ASN.2005040364
50. Karin N. CXCR3 ligands in cancer and autoimmunity, chemoattraction of effector T cells, and beyond. *Front Immunol*. 2020;11:976. doi:10.3389/fimmu.2020.00976
51. Salomon I, Netzer N, Wildbaum G, Schiff-Zuck S, Maor G, Karin N. Targeting the function of IFN-gamma-inducible protein 10 suppresses ongoing adjuvant arthritis. *J Immunol*. 2002;169(5):2685–2693. doi:10.4049/jimmunol.169.5.2685
52. Dufour JH, Dziejman M, Liu MT, Leung JH, Lane TE, Luster AD. IFN-gamma-inducible protein 10 (IP-10; CXCL10)-deficient mice reveal a role for IP-10 in effector T cell generation and trafficking. *J Immunol*. 2002;168(7):3195–3204. doi:10.4049/jimmunol.168.7.3195
53. Guay JA, Wojchowski DM, Fang J, Oxburgh L. Death associated protein kinase 2 is expressed in cortical interstitial cells of the mouse kidney. *BMC Res Notes*. 2014;7(1):345. doi:10.1186/1756-0500-7-345
54. Truong LD, Foster SV, Barrios R, D'agati V, Verani RR, Gonzalez JM. Tenascin is an ubiquitous extracellular matrix protein of human renal interstitium in normal and pathologic conditions. *Nephron*. 1996;72(4):579–586. doi:10.1159/000188943
55. He W, Xie Q, Wang Y, Chen J, Zhao M, Davis LS. Generation of a tenascin-C-CreER2 knockin mouse line for conditional DNA recombination in renal medullary interstitial cells. *PLoS One*. 2013;8(11):e79839. doi:10.1371/journal.pone.0079839
56. Shaw IW, O'Sullivan ED, Pisco AO, Borthwick G, Gallagher KM, Péault B. Aging modulates the effects of ischemic injury upon mesenchymal cells within the renal interstitium and microvasculature. *Stem Cells Transl Med*. 2021;10(8):1232–1248. doi:10.1002/sctm.20-0392
57. Cheng HW, Onder L, Novkovic M, Sonesson C, Lütge M, Pikor N. Origin and differentiation trajectories of fibroblastic reticular cells in the splenic white pulp. *Nat Commun*. 2019;10(1):1739. doi:10.1038/s41467-019-09728-3
58. Li Z, Kuppe C, Ziegler S, Cheng M, Kabgani N, Menzel S. Chromatin-accessibility estimation from single-cell ATAC-seq data with scOpen. *Nat Commun*. 2021;12(1):6386. doi:10.1038/s41467-021-26530-2
59. Tomoishi S, Fukushima S, Shinohara K, Katada T, Saito K. CREB3L2-mediated expression of Sec23A/Sec24D is involved in hepatic stellate cell activation through ER-Golgi transport. *Sci Rep*. 2017;7(1):7992. doi:10.1038/s41598-017-08703-6
60. Legler DF, Loetscher M, Roos RS, Clark-Lewis I, Baggiolini M, Moser B. B cell-attracting chemokine 1, a human CXC chemokine expressed in lymphoid tissues, selectively attracts B lymphocytes via BLR1/CXCR5. *J Exp Med*. 1998;187(4):655–660. doi:10.1084/jem.187.4.655
61. Thompson JS, Bixler SA, Qian F, Vora K, Scott ML, Cachero TG. BAFF-R, a newly identified TNF receptor that specifically interacts with BAFF. *Science*. 2001;293(5537):2108–2111. doi:10.1126/science.1061965
62. Schneider P, Mackay F, Steiner V, Hofmann K, Bodmer JL, Holler N. BAFF, a novel ligand of the tumor necrosis factor family, stimulates B cell growth. *J Exp Med*. 1999;189(11):1747–1756. doi:10.1084/jem.189.11.1747
63. Muto Y, Wilson PC, Ledru N, Wu H, Dimke H, Waikar SS. Single cell transcriptional and chromatin accessibility profiling redefine cellular heterogeneity in the adult human kidney. *Nat Commun*. 2021;12(1):2190. doi:10.1038/s41467-021-22368-w
64. Casemayou A, Fournel A, Bagattin A, Schanstra J, Belliere J, Decramer S. Hepatocyte nuclear factor-1 β controls mitochondrial respiration in renal tubular cells. *J Am Soc Nephrol*. 2017;28(11):3205–3217. doi:10.1681/ASN.2016050508
65. Eriguchi Y, Nakamura K, Yokoi Y, Sugimoto R, Takahashi S, Hashimoto D. Essential role of IFN- γ in T cell-associated intestinal inflammation. *JCI Insight*. 2018;3(18):e121886. doi:10.1172/jci.insight.121886
66. Karki R, Sharma BR, Tuladhar S, Williams EP, Zalduondo L, Samir P. Synergism of TNF- α and IFN- γ triggers inflammatory cell death, tissue damage, and mortality in SARS-CoV-2 infection and cytokine shock syndromes. *Cell*. 2021;184(1):149–168.e17. doi:10.1016/j.cell.2020.11.025
67. Xu Z, Chen D, Hu Y, Jiang K, Huang H, Du Y. Anatomically distinct fibroblast subsets determine skin autoimmune patterns. *Nature*. 2022;601(7891):118–124. doi:10.1038/s41586-021-04221-8
68. Zerrouk N, Miagoux Q, Dispot A, Elati M, Niarakis A. Identification of putative master regulators in rheumatoid arthritis synovial fibroblasts using gene expression data and network inference. *Sci Rep*. 2020;10(1):16236. doi:10.1038/s41598-020-73147-4
69. van Schouwenburg PA, Rispens T, Wolbink GJ. Immunogenicity of anti-TNF biologic therapies for rheumatoid arthritis. *Nat Rev Rheumatol*. 2013;9(3):164–172. doi:10.1038/nrrheum.2013.4
70. Winthrop KL. The emerging safety profile of JAK inhibitors in rheumatic disease. *Nat Rev Rheumatol*. 2017;13(5):320. doi:10.1038/nrrheum.2017.51
71. Qi F, Liu F, Gao L. Janus kinase inhibitors in the treatment of vitiligo: a review. *Front Immunol*. 2021;12:790125. doi:10.3389/fimmu.2021.790125
72. Nayar S, Campos J, Smith CG, Iannizzotto V, Gardner DH, Mourcin F. Immunofibroblasts are pivotal drivers of tertiary lymphoid structure formation and local pathology. *Proc Natl Acad Sci U S A*. 2019;116(27):13490–13497. doi:10.1073/pnas.1905301116
73. Fleig S, Kapanadze T, Bernier-Latmani J, Lill JK, Wyss T, Gamrekelashvili J. Loss of vascular endothelial notch signaling promotes spontaneous formation of tertiary lymphoid structures. *Nat Commun*. 2022;13(1):2022. doi:10.1038/s41467-022-29701-x
74. Rosales IA, Yang C, Farkash EA, Ashry T, Ge J, Aljabban I. Novel intra-graft regulatory lymphoid structures in kidney allograft tolerance. *Am J Transplant*. 2022;22(3):705–716. doi:10.1111/ajt.16880
75. Sato Y, Silina K, van den Broek M, Hirahara K, Yanagita M. The roles of tertiary lymphoid structures in chronic diseases. *Nat Rev Nephrol*. 2023;19(8):525–537. doi:10.1038/s41581-023-00706-z

AFFILIATIONS

¹Department of Nephrology, Graduate School of Medicine, Kyoto University, Kyoto, Japan

²RIKEN Center for Integrative Medical Sciences, Yokohama, Kanagawa, Japan

³Institute for the Advanced Study of Human Biology (WPI-ASHBi), Kyoto University, Kyoto, Japan

⁴Department of Urology, Graduate School of Medicine, Kyoto University, Kyoto, Japan

⁵Department of Diagnostic Pathology, Graduate School of Medicine, Kyoto University, Kyoto, Japan

⁶Department of Life Science Frontiers, Center for iPS Cell Research and Application (CiRA), Kyoto University, Kyoto, Japan

⁷Medical-risk Avoidance based on iPS Cells Team, RIKEN Center for Advanced Intelligence Project (AIP), Kyoto, Japan

⁸IFOM-ETS, Milan, Italy

Supplemental Information for the Study:

Tertiary lymphoid tissues are microenvironments with intensive interactions between immune cells and proinflammatory parenchymal cells in aged kidneys

Takahisa Yoshikawa¹, Akiko Oguchi^{1,2,3}, Naoya Toriu^{1,3}, Yuki Sato¹, Takashi Kobayashi⁴, Osamu Ogawa⁴, Hironori Haga⁵, Satoko Sakurai⁶, Takuya Yamamoto^{3,6,7}, Yasuhiro Murakawa^{2,3,8}, Motoko Yanagita^{1,3*}

¹Department of Nephrology, ⁴Department of Urology, ⁵Department of Diagnostic Pathology, Graduate School of Medicine, Kyoto University, Kyoto, Japan

²RIKEN Center for Integrative Medical Sciences, Yokohama, Kanagawa, Japan

³Institute for the Advanced Study of Human Biology (WPI-ASHBi), Kyoto University, Kyoto, Japan

⁶Department of Life Science Frontiers, Center for iPS Cell Research and Application (CiRA), Kyoto University, Kyoto, Japan

⁷Medical-risk Avoidance based on iPS Cells Team, RIKEN Center for Advanced Intelligence Project (AIP), Kyoto, Japan

⁸IFOM-ETS, Milan, Italy

*To whom correspondence should be addressed:

Motoko Yanagita: Department of Nephrology, Graduate School of Medicine, Kyoto University, Shogoin-Kawahara-cho 54, Sakyo-ku, Kyoto 606-8507, Japan

E-mail: motoy@kuhp.kyoto-u.ac.jp, Tel: +81-75-751-3860, Fax: +81-75-751-3859

Supplemental Material Table of Contents

Supplemental Methods

Supplemental Figures 1–22

Supplemental Figure 1. Workflow of computational analysis for each dataset.

Supplemental Figure 2. Analysis on each dataset of the three ischemia–reperfusion injury (IRI) kidneys.

Supplemental Figure 3. Representative images used to count VCAM1⁺ or KIM1⁺ proximal tubular (PT) cells in injured kidneys.

Supplemental Figure 4. Sanger sequence analysis of off-targets of wild-type and STAT1-KO C3H10T1/2 cells.

Supplemental Figure 5. Histology of mouse kidneys 30 days after sham surgery and 45-minute IRI.

Supplemental Figure 6. Expression patterns of well-known marker genes across immune cells in the IRI kidneys.

Supplemental Figure 7. Injured distal nephrons with upregulated *Lcn2* expression in the IRI kidneys.

Supplemental Figure 8. Enrichment analysis of the reclustered PT clusters in the IRI kidney dataset.

Supplemental Figure 9. Expression patterns of the genes encoding ligands highly expressed in the injured PT-1 across the four PT clusters.

Supplemental Figure 10. Pearson correlation analysis between the injured PT-1 in our analysis and PT subpopulations in previous publication.

Supplemental Figure 11. Expression patterns of *Cxcr3*, *Tnf*, and *Ifng* in immune cells in aged injured kidneys with tertiary lymphoid tissues (TLTs) based on single-cell RNA-sequencing dataset.

Supplemental Figure 12. Trajectory analysis of PT subsets.

Supplemental Figure 13. Histology of aged injured kidneys 30 days after 18-minute mild IRI.

Supplemental Figure 14. Comparison of the expression of injured PT markers between aged and young injured kidneys.

Supplemental Figure 15. Immunofluorescence images for transcription factors, p65 and STAT1, in aged injured kidneys with TLTs.

Supplemental Figure 16. *In situ* hybridization images showing high *Stat1* expression within TLTs and their surroundings.

Supplemental Figure 17. Analysis of fibroblasts in the sham-treated kidney.

Supplemental Figure 18. Expression levels of pericyte markers across fibroblast subpopulations in the IRI kidney dataset.

Supplemental Figure 19. KEGG pathways enriched in the fibroblast subpopulations in aged injured kidneys.

Supplemental Figure 20. Expression patterns of selected marker genes from the profibrotic and proinflammatory fibroblasts in aged injured kidneys.

Supplemental Figure 21. Gene expression kinetics during fibroblast differentiation in aged injured kidneys was determined using pseudotime trajectory analysis.

Supplemental Figure 22. Comparison of the expression of proinflammatory fibroblast markers between aged and young injured kidneys.

Supplemental Tables 1–10 (Microsoft Excel format)

Supplemental Table 1. Marker gene lists for each dataset.

Supplemental Table 2. Parameters and the number of nuclei used in the analysis.

Supplemental Table 3. Clinical profiles of two cases after kidney transplantation.

Supplemental Table 4. Enrichment analysis results for PT clusters in aged injured kidneys.

Supplemental Table 5. Regulon activity across the PT clusters in aged injured kidneys. Supplemental

Table 6. Differentially expressed genes (DEG) lists of HK-2 cells treated with vehicle, TNF α , and IFN γ .

Supplemental Table 7. Enrichment analysis results for fibroblast clusters in aged injured kidneys.

Supplemental Table 8. Regulon activity across the fibroblast clusters in aged injured kidneys.

Supplemental Table 9. Result of branched expression analysis modeling (BEAM) analysis on the

fibroblast subset in aged injured kidneys.

Supplemental Table 10. Primers for quantitative real-time PCR.

References for Supplemental Information

Supplemental Methods

Renal histochemistry

The mouse kidneys were harvested and cut along the short axis. They were then fixed in 4% paraformaldehyde or 10% neutralized formaldehyde for histological analysis. The kidneys fixed with 10% neutralized formaldehyde were sectioned at 4.0- μ m thickness and stained with periodic acid-Schiff (PAS) and Masson's trichrome (MT). The human kidneys were fixed by formalin, embedded by paraffin, sectioned at 4.0- μ m thickness.

Immunofluorescence

Immunofluorescence studies of mouse and human kidneys were performed as previously described.¹ Briefly, the kidneys were fixed in 4% paraformaldehyde (PFA) for 6 hours, incubated in 20% sucrose in PBS for 6 hours, and incubated in 30% sucrose in PBS overnight at 4°C. The kidneys were embedded in optimum cutting temperature (OCT) compound (Tissue-Tek O.C.T. Compound, 4853, Sakura Finetek, Tokyo, Japan) and cryosectioned at 6.0- μ m thickness and mounted on slides glasses (MAS-01, 83-1881, MATSUNAMI, Osaka, Japan). Formaldehyde-fixed and paraffin-embedded kidney samples were sectioned at a 4.0- μ m thickness and used for immunofluorescence analysis. The sections were deparaffinized with xylene and rehydrated with ethanol. Antigen retrieval at 15 minutes at 110°C with the citrate buffer or 10 minutes at 95°C with Dako Target Retrieval Solution, pH 9 (S2367, Dako, Glostrup, Denmark) was performed for deparaffinized and rehydrated sections. These sections were blocked with 5% serum appropriate for secondary antibodies for 1 hour at room temperature and then incubated with primary antibodies for overnight at 4°C. The following antibodies were used for immunofluorescence staining for mouse kidneys: rat anti-B220 (557390, BD PharMingen, San Diego, CA, USA, 1/200), Armenian hamster anti-CD3 ϵ (550275, BD PharMingen, 1/200), goat anti-p75 neurotrophin receptor (p75NTR) (AF1157, R&D Systems, Minneapolis, MN, USA, 1/200), rat anti-KIM1 (14-5861-82, eBioscience, San Diego, CA, USA, 1/200), goat anti-VCAM1 (AF643, R&D Systems, 1/200), goat anti-CXCL9 (AF-492-NA, R&D Systems, 1/200), goat anti-CXCL10 (AF-466-NA, R&D Systems, 1/100), rabbit anti-p105/p50 (13586, Cell Signaling

Technology [CST], Danvers, MA, USA, 1/1000), rabbit anti-STAT1 (9172, CST, 1/500), rabbit anti-phospho-STAT1 (Tyr701) (9167, CST, 1/200), rabbit anti-Tenascin C (ab108930, abcam, Cambridge, UK, 1/200), goat anti-FOXP2 (ab1307, abcam, 1/1000), goat anti-PDGFR β (AF1042, R&D Systems, 1/200), rat anti-PDGFR β (14-1402-82, eBioscience, 1/200), goat anti-Type 1 collagen (1310-01, Southern Biotech, Birmingham, AL, USA, 1/200), rabbit anti-Fibronectin (F3648, Sigma-Aldrich, Saint Louis, MO, USA, 1/200), Cy3-conjugated mouse anti α -smooth muscle actin (α SMA) (C6198, Sigma-Aldrich, 1/1000), goat anti-IL33 (AF3626, R&D Systems, 1/8000), rat anti-C3 (1/200), Syrian hamster anti-Podoplanin (14-5381-82, eBioscience, 1/1000), Armenian hamster anti-milk fat globule EGF and factor V/VIII domain containing (MFGE8) (D199-3, Medical & Biological Laboratories [MBL], Tokyo, Japan, 1/200), and rabbit anti-RUNX1 (ab92336, abcam, 1/200). Alexa Fluor 647-conjugated Phalloidin (A22287, Invitrogen, Waltham, MA, USA, 1/500) or Fluorescein-Lotus Tetragonolobus Lectin (LTL) (FL-1321-2, Vector Laboratories, Burlingame, CA, USA, 1/200) was used to stain the PT cells. The following antibodies were used for immunofluorescence staining of human kidneys: rabbit anti-CD3 ϵ (ab5690, abcam, 1/100), mouse anti-CD20 (14-0202-82, eBioscience, 1/200), rabbit anti-Ki67 (ab16667, abcam, 1/200), mouse anti-CD21 (MA5-11417, Invitrogen, 1/100), mouse anti-megalin (sc515772, Santa Cruz, Dallas, TX, USA, 1/200), rabbit anti-VCAM1 (ab134047, abcam, 1/200), goat anti-p75NTR (AF1157, R&D Systems, 1/200), and rabbit anti-phospho-STAT1 (Tyr701) (9167, CST, 1/200). The sections were incubated with secondary antibody including Alexa Fluor 488-, Alexa Fluor 546-, Alexa Fluor 594-, and Cy3-conjugated for 1 hour at room temperature in the dark, counterstained with DAPI, and mounted in mounting medium (Fluoromount, K024, Diagnostic BioSystems, Pleasanton, CA, USA). All of the immunofluorescence samples were analyzed using a confocal microscope (FV1000-D, OLYMPUS, Tokyo, Japan) or an all-in-one fluorescence microscope (BZ-X710, KEYENCE, Osaka, Japan).

Immunohistochemistry

For immunohistochemistry of mouse and human kidneys, formaldehyde-fixed and paraffin-embedded sections were deparaffinized and rehydrated, as described above, for immunofluorescence. After

rehydration, endogenous peroxidase was blocked with 3% H₂O₂, and antigen retrieval was performed as described above for immunofluorescence. The sections were stained with the following primary antibodies: rabbit anti-VCAM1 (39036, CST, 1/200), mouse anti-megalin (sc515772, Santa Cruz, 1/200), rabbit anti-p105/p50 (13586, CST, 1/1000), rabbit anti-p65 (8242, CST, 1/1000), rabbit anti-STAT1 (9172, CST, 1/500), rabbit anti-IRF1 (8478, CST, 1/100), and rabbit anti-phospho-STAT1 (Tyr701) (9167, CST, 1/200). Antibody labeling was detected using a Histofine Simple Stain MAX-PO(R) (414341, NICHIREI BIOSCIENCES, Tokyo, Japan) and a Diaminobenzidine (DAB) Substrate Kit (SK-4100, Vector Laboratories) for rabbit primary antibodies and a Histofine Simple Stain AP(M) (414241, NICHIREI BIOSCIENCES) and an ImmPACT Vector Red Substrate Kit (SK-5105, Vector Laboratories) for mouse primary antibodies. Sections were counterstained using Mayer's Hematoxylin Solution (131-09665, FUJIFILM Wako Pure Chemical Corporation, Osaka, Japan) and mounted in malinol (20091, MUTO PURE CHEMICALS, Tokyo, Japan).

RNAscope *in situ* hybridization

In situ hybridization was performed using an RNAscope Multiplex Fluorescent Assay V2 (323100; Advanced Cell Diagnostics [ACD], Newark, CA, USA) on murine and human kidney samples fixed with 4% paraformaldehyde for 24 hours, embedded in OCT, and cryosectioned at a 10- μ m thickness or fixed with 10% neutralized formaldehyde for 24 hours, embedded in paraffin, and sectioned at a 4.0- μ m thickness, according to the manufacturer's instructions. The following RNAscope Target Probes were used (all from ACD): Mm-Ccl2 (311791), Mm-Cxcl10 (408921), Mm-Tgfb2 (406181), Mm-Stat1 (479611-C2), Mm-Tnf (481321-C2), Mm-Ifng (311391-C3), Mm-Tnfsf13b (414891), Mm-Pdgfrb (411381-C2), and Hs-CXCL9 (440161).

Reanalysis on single-cell RNA-sequencing dataset for CD45⁺ immune cells in aged injured kidneys with TLTs

We reused the single-cell RNA-sequencing Seurat object of CD45⁺ immune cells in aged injured kidneys with TLTs 45 days after a 45-minute ischemia–reperfusion injury (IRI) that we previously

reported.² We showed Uniform Manifold Approximation and Projection (UMAP) plots, gene expression patterns of representative marker genes for each cluster using dot plots, and *Cxcr3*, *Tnf*, and *Ifng* expression patterns using violin plots.

Cell culture experiments

HK2 cells, a human PT cell line, were purchased from the American Type Culture Collection (ATCC, Manassas, VA, USA), and C3H10T1/2 cells, mouse embryonic fibroblasts, were purchased from the Health Science Research Resources Bank (HSRRB, Osaka, Japan). HK2 cells were cultured with DMEM/Ham's F-12 (11581-15, Nacalai Tesque, Kyoto, Japan) supplemented with 10% FBS (FBS Standard, CCP-BS-BR-500, Cosmo Bio, Tokyo, Japan) and penicillin-streptomycin (26253-84, Nacalai Tesque). The cells were treated with recombinant murine TNF α (315-01A, Peprotech, Cranbury, NJ, USA), IFN γ (315-05, Peprotech), or both in DMEM/2.0% FBS for 24 hours at 37°C, and harvested. RNA from the cells was subjected to quantitative real-time PCR analysis. C3H10T1/2 cells were cultured with DMEM (high glucose) (08458-45, Nacalai Tesque) supplemented with 10% FBS and penicillin-streptomycin. They were treated with recombinant murine IFN γ in DMEM/0.5% FBS for 24 hours at 37°C after incubation with DMEM/0.5% FBS for 12 hours, and then harvested. Their RNA was subjected to quantitative real-time PCR analysis and bulk RNA-sequencing, and their protein was subjected to western blotting (WB) analysis.

Western blotting

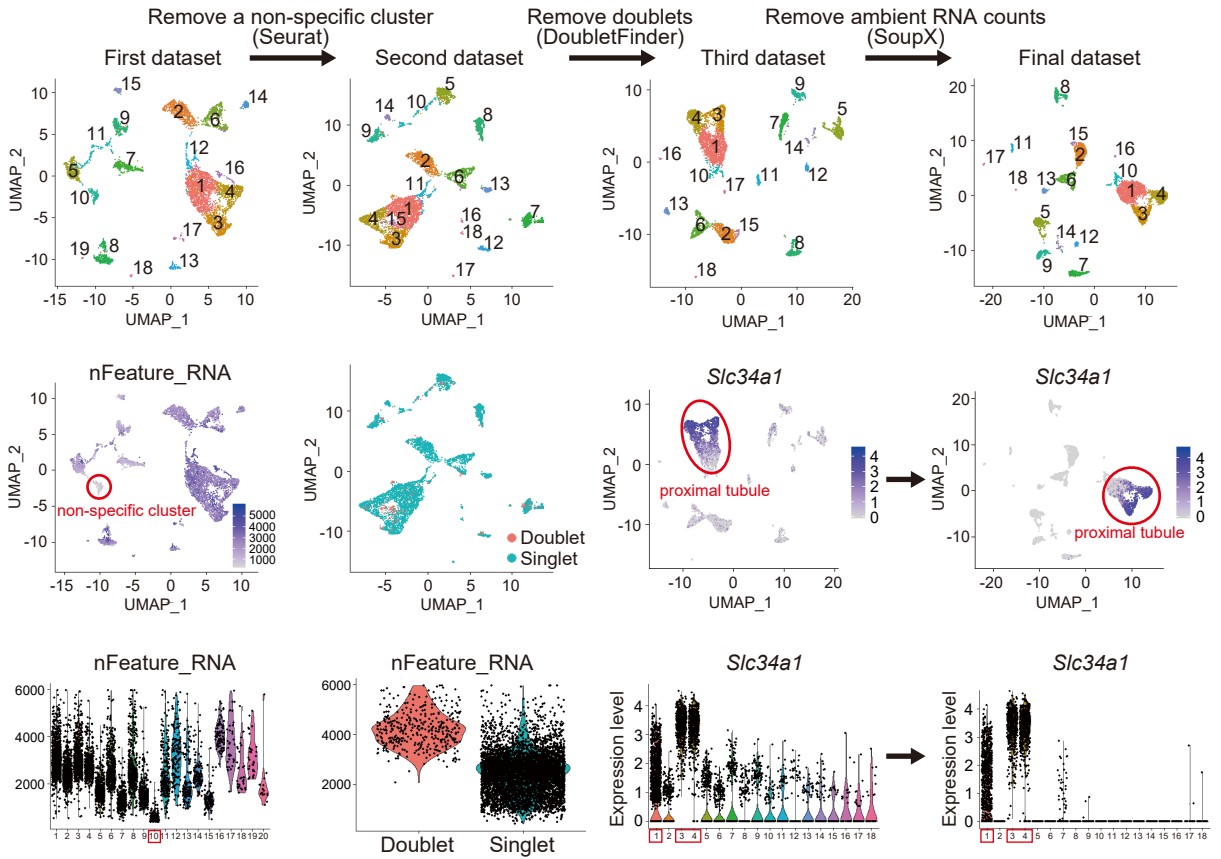
Proteins were extracted from C3H10T1/2 cells and WB was performed to screen cells lacking STAT1 protein. Briefly, cells were suspended in RIPA buffer (50 mM Tris-HCl [pH 7.5] [35434-21, Nacalai Tesque], 150 mM NaCl [31320-05, Nacalai Tesque], 1% Nonidet P-40 [145-09701, FUJIFILM Wako Pure Chemical Corporation], and 0.25% sodium dodecyl sulfate [SDS] [191-07145, FUJIFILM Wako Pure Chemical Corporation]), rotated for one hour at 4°C, and centrifuged. After centrifugation, the supernatants were used as total cell lysates. Twenty μ g of each sample was applied to SDS-polyacrylamide gel electrophoresis. STAT1 immunoblotting was performed using rabbit anti-STAT1

antibody (9172S, CST, 1/1000). Equal protein loading was confirmed by GAPDH immunoblotting using mouse anti-GAPDH antibody (10R-G109A, Fitzgerald, Acton, MA, USA, 1/4000). The following secondary antibodies were used: horseradish peroxidase (HRP)-linked goat anti-rabbit antibody (7074S, CST, 1/2000) and HRP-linked horse anti-mouse antibody (7076S, CST, 1/5000). The WB bands were captured using a LAS500mini (GE Healthcare, Chicago, IL, USA).

Quantitative real-time PCR

RNA extraction and real-time PCR were performed as described previously.¹ Specific primers were designed using the online tool Primer3Plus (<https://www.bioinformatics.nl/cgi-bin/primer3plus/primer3plus.cgi>), and the specificity was confirmed using Primer-BLAST (<https://www.ncbi.nlm.nih.gov/tools/primer-blast/>). The primer sequences are listed in Supplemental Table 10. Expression levels were normalized to those of mouse *Gapdh* or human *GAPDH*.

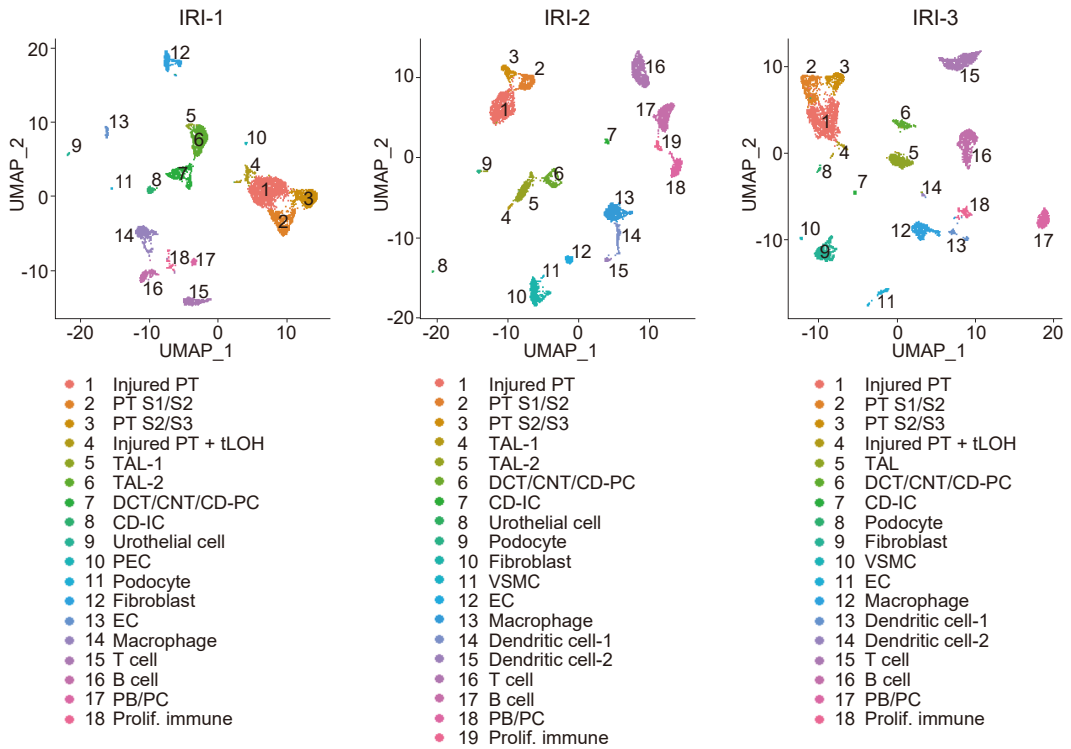
Supplemental Figure 1



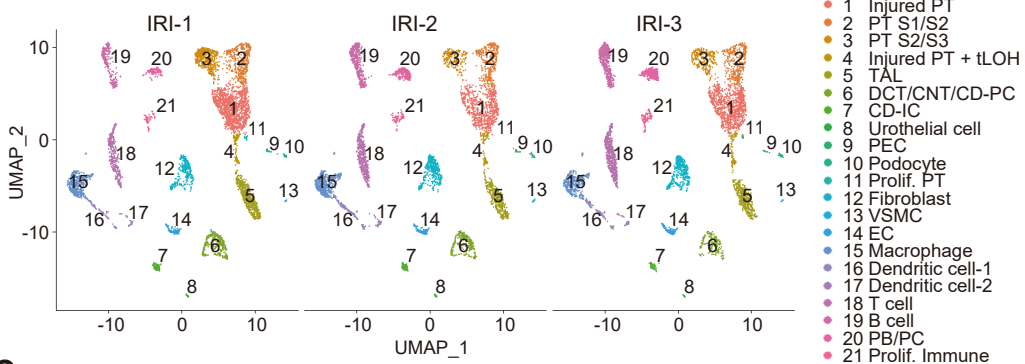
Supplemental Figure 1. Workflow of computational analysis for each dataset. First, the Cell Ranger output “filtered feature matrix” was processed as described in the **Methods** section. The second dataset was generated by removing the non-specific cluster (enclosed with red lines) with the low number of features and without cell type-specific markers from the first dataset using the “subset” function in Seurat. The third dataset was generated by removing estimated doublets from the second dataset using the R package “DoubletFinder”. The final dataset was generated by subtracting ambient RNA counts from the third dataset using the R package “SoupX”. For example, expression of *Slc34a1*, a PT cell marker, was detected in multiple clusters other than PT clusters (cluster 1, 3, and 4 encircled by led lines) in the third dataset. After subtraction of the ambient RNA counts, *Slc34a1* expression was mostly confined to PT clusters in the final dataset. The detailed process for the computational analysis is described in **Methods** section.

Supplemental Figure 2

A



B



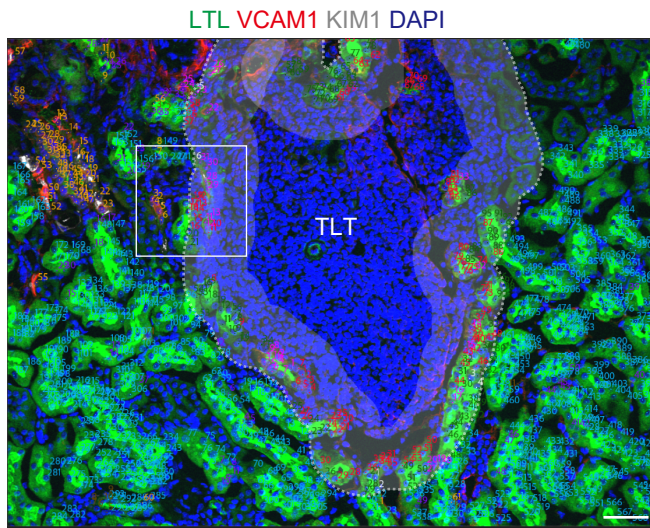
C

Cluster	IRI-1	IRI-2	IRI-3
1	1335	705	994
2	487	353	382
3	488	192	250
4	121	96	116
5	617	365	416
6	415	245	167
7	118	83	60
8	34	22	19
9	33	18	20
10	33	47	56
11	31	2	19
12	315	446	418
13	17	26	26
14	125	143	164
15	415	497	337
16	79	168	168
17	57	69	70
18	380	586	666
19	269	500	597
20	121	338	365
21	60	87	120
total	5550	4988	5430

Supplemental Figure 2. Analysis on each dataset of the three ischemia–reperfusion injury kidneys. (A) Uniform Manifold Approximation and Projection (UMAP) plots for each ischemia–reperfusion injury (IRI) kidney dataset that was analyzed without integration. All datasets included similar cell types. (B) UMAP plots of the integrated IRI kidney dataset separated by the sample of origin (IRI-1, IRI-2, and IRI-3). (C) Tables displaying the number of nuclei included in each cluster in each IRI kidney sample (IRI-1, IRI-2, and IRI-3) in the integrated IRI kidney dataset. Each replicate included all cell types with some differences in the proportions. PT, proximal tubule; S1/S2, S1 segment/S2 segment; S2/S3, S2 segment/S3 segment; tLOH, thin limbs of the loop of Henle; TAL, thick ascending limbs of the loop of Henle; DCT, distal convoluted tubule; CNT, connecting tubule; CD, collecting duct; PC, principal cell; IC, intercalated cell; PEC, parietal epithelial cell; EC, endothelial cell; VSMC, vascular smooth muscle cell; PB/PC, plasmablast/plasma cell; Prolif., proliferating

Supplemental Figure 3

A



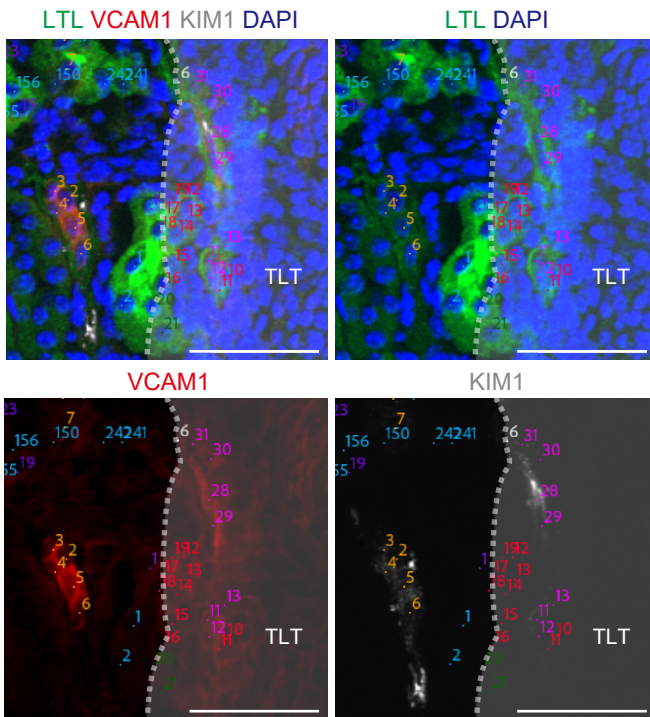
B

	Counts
TLT+KIM1+VCAM1+	33
TLT+KIM1+VCAM1-	6
TLT+KIM1-VCAM1+	88
TLT+KIM1-VCAM1-	99
TLT+ (total)	226

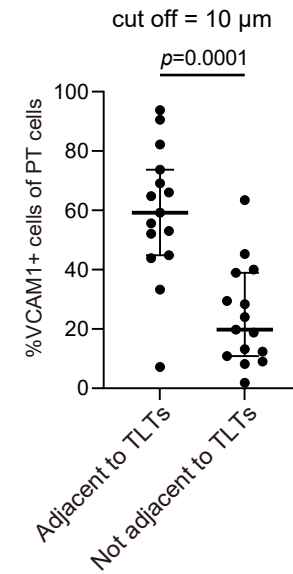
	Counts
TLT-KIM1+VCAM1+	61
TLT-KIM1+VCAM1-	12
TLT-KIM1-VCAM1+	50
TLT-KIM1-VCAM1-	580
TLT- (total)	703

TLT+: PT cells adjacent to TLTs
TLT-: PT cells not adjacent to TLTs

C

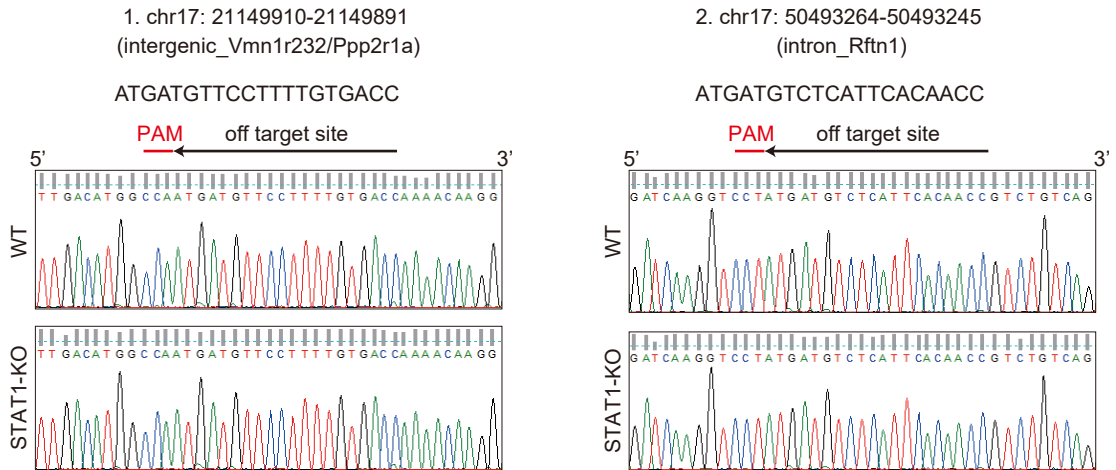


D



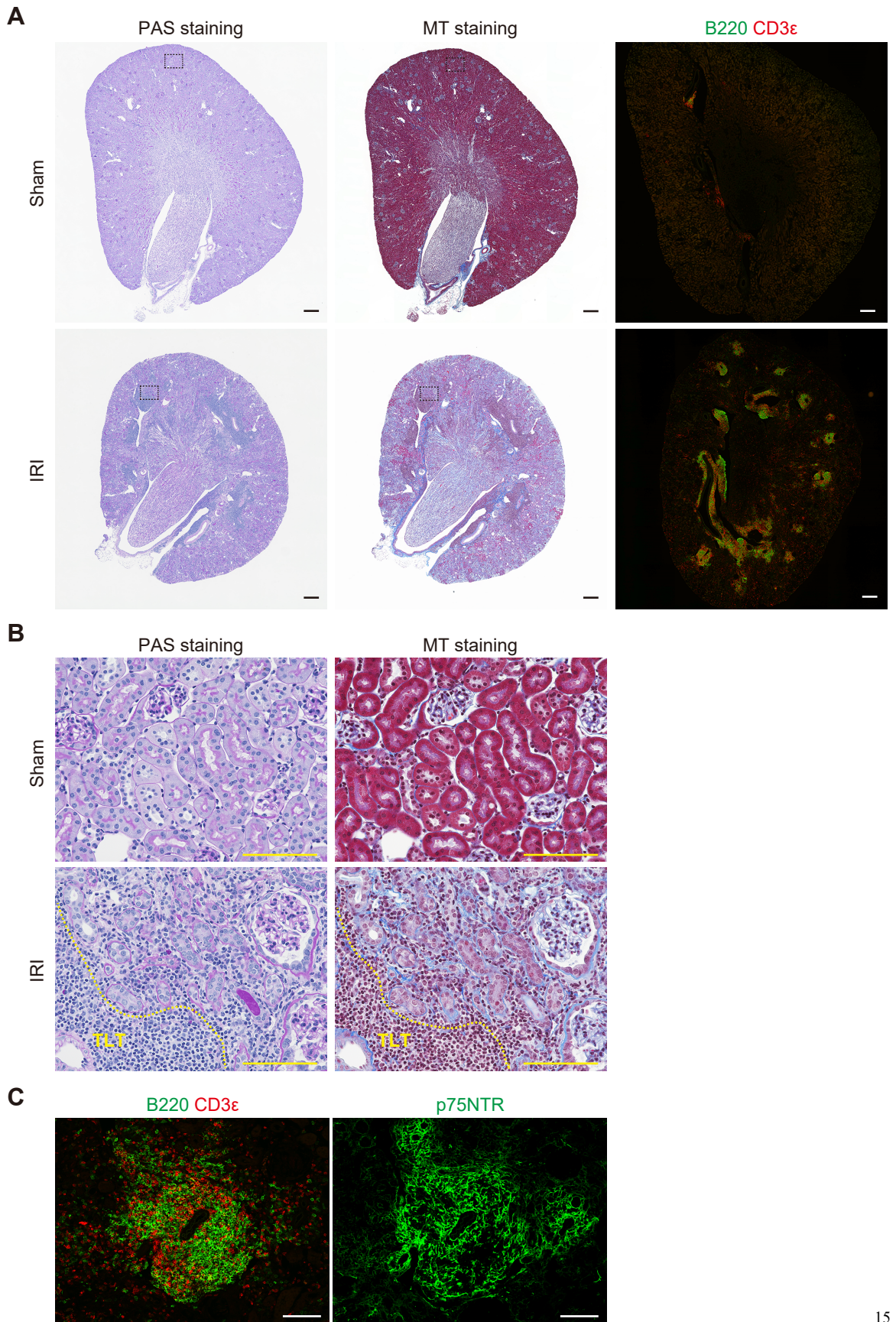
Supplemental Figure 3. Representative images used to count VCAM1⁺ or KIM1⁺ PT cells in injured kidneys. (A–C) Immunofluorescence images of PTs stained using LTL (green), VCAM1 (red), KIM1 (gray), and DAPI (blue). (A) All PT cells were classified into eight types based on whether they were adjacent to TLTs (within 35 μm from the TLT boundaries, the area within the outer dashed line of the translucent band) and the staining pattern for VCAM1 and KIM1. They were counted using colored numbers based on their classification. (B) Tables showing the number of PT cells in each classification in the representative image in (A). (C) Magnified images of the area enclosed with a square in (A). Scale = 50 μm. (D) Quantification of the percentages of VCAM1⁺ PT cells among “PT cells adjacent to TLTs” or “PT cells not adjacent to TLTs” with setting the cutoff distance from TLT borders to 10 μm, in each region of interest (ROI) in mild IRI model, using three ROIs including TLTs per kidney section (n = 5, total of 15 ROIs). With this cutoff, VCAM1⁺ PT cells were also significantly more prevalent around TLTs than in the other area (p = 0.0001). Data are shown as the median and interquartile range. Mann–Whitney test was used to analyze the difference.

Supplemental Figure 4



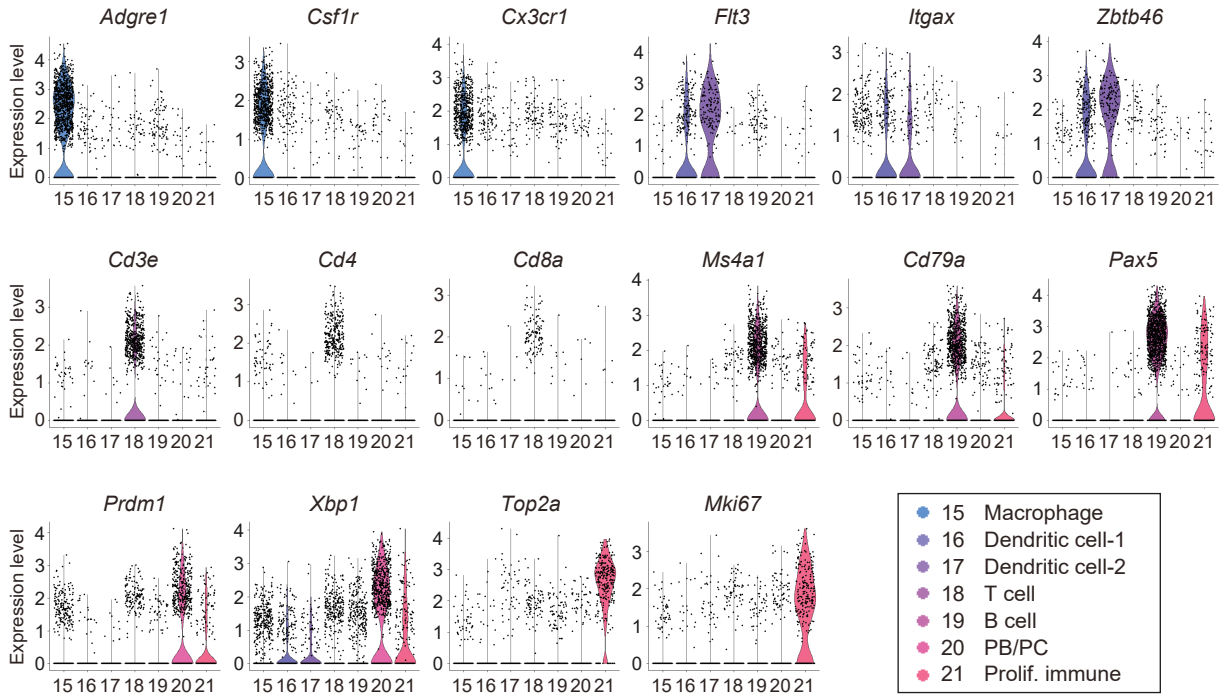
Supplemental Figure 4. Sanger sequence analysis of off-targets of wild-type and STAT1-knockout C3H10T1/2 cells. Sanger sequence analysis on the two representative potential off target sites with the highest Cutting Frequency Determination (CFD) scores calculated by CRISPOR demonstrated no mutation in STAT1-knockout (KO) C3H10T1/2 cells (1; intergenic_Vmn1r232/Ppp2r1a, 2; intron_Rftn1).³ (red line, protospacer adjacent motif (PAM) sequence; black arrow, off target site sequence)

Supplemental Figure 5



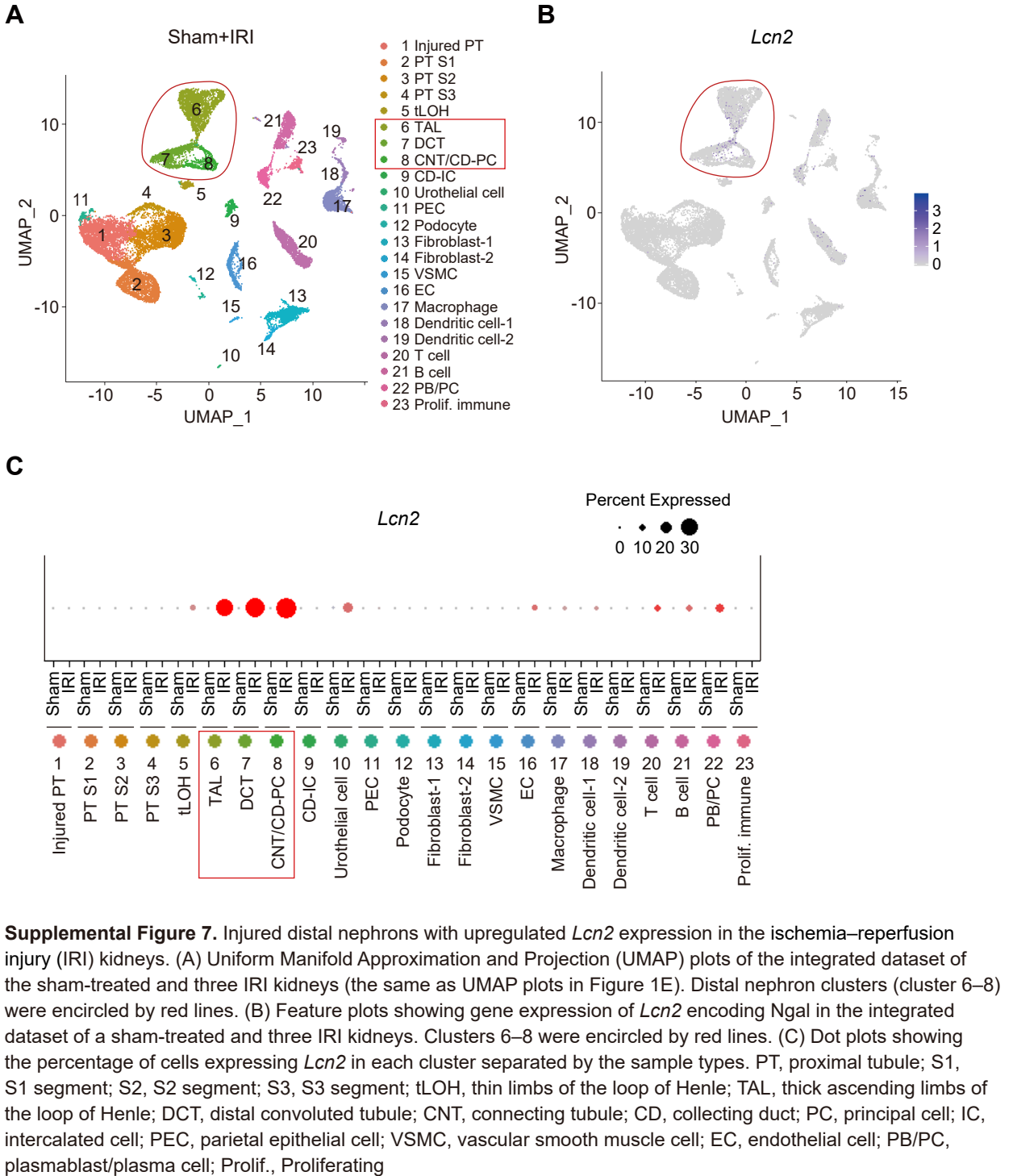
Supplemental Figure 5. Histology of mouse kidneys 30 days after sham surgery and 45-minute ischemia–reperfusion injury (IRI). (A) Periodic acid–Schiff (PAS) staining, Masson–Trichrome (MT) staining, and immunofluorescence staining for B220 (green) and CD3 ϵ (red) of a murine kidney 30 days after sham surgery and IRI, which was used for snRNA-seq. The kidney after IRI showed multiple TLTs and extensive fibrosis. Scale bars = 300 μ m. (B) The areas enclosed by dashed lines in (A) were magnified. Tubular atrophy and interstitial fibrosis were identified in aged injured kidneys after IRI. TLT borders were shown as yellow dashed lines. Scale bars = 100 μ m. (C) Representative immunofluorescence images of TLTs staining for B220 (green) and CD3 ϵ (red), markers for B cells and T cells, respectively, and for p75 neurotrophin receptor (p75NTR) (green), a marker for fibroblasts within TLTs. Scale bars = 100 μ m.

Supplemental Figure 6



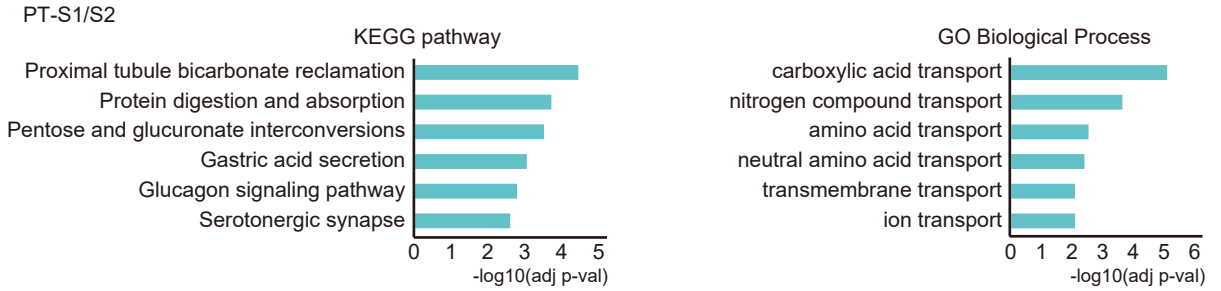
Supplemental Figure 6. Expression patterns of well-known marker genes across immune cells in the ischemia–reperfusion injury (IRI) kidneys. Violin plots showing expression patterns of the well-known marker genes for each immune cell type across immune cell clusters in the IRI kidney dataset (cluster 15–21 in Figure 1D). *Adgre1*, *Csf1r*, and *Cx3cr1* are used as macrophage markers, *Flt3*, *Itgax*, and *Zbtb46* as dendritic cell markers, *Cd3e*, *Cd4*, and *Cd8a* as T cell markers, *Ms4a1*, *Cd79a*, and *Pax5* as B cell markers, *Prdm1* and *Xbp1* as plasmablast/plasma cell (PB/PC) markers, and *Top2a* and *Mki67* as proliferating (Prolif.) cell markers.

Supplemental Figure 7

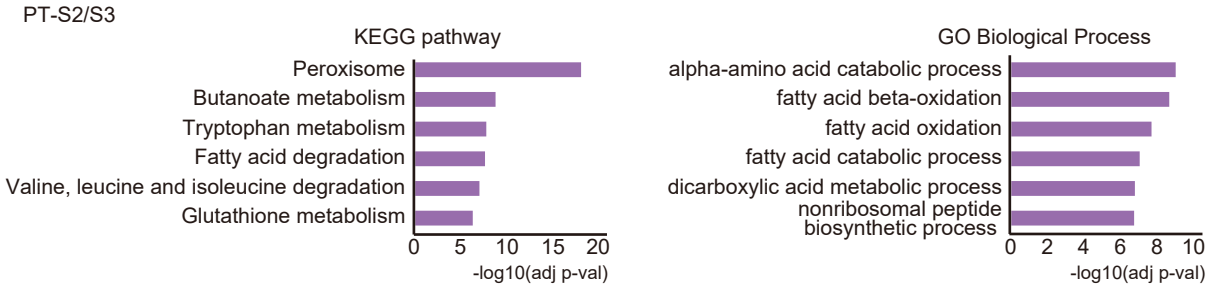


Supplemental Figure 8

A

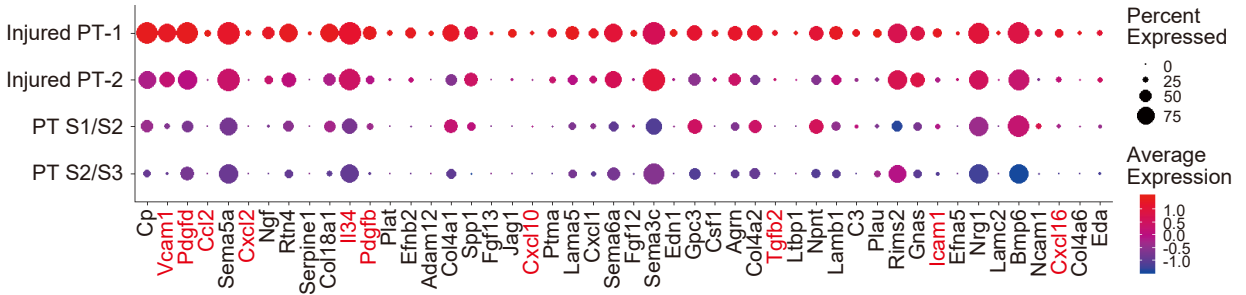


B



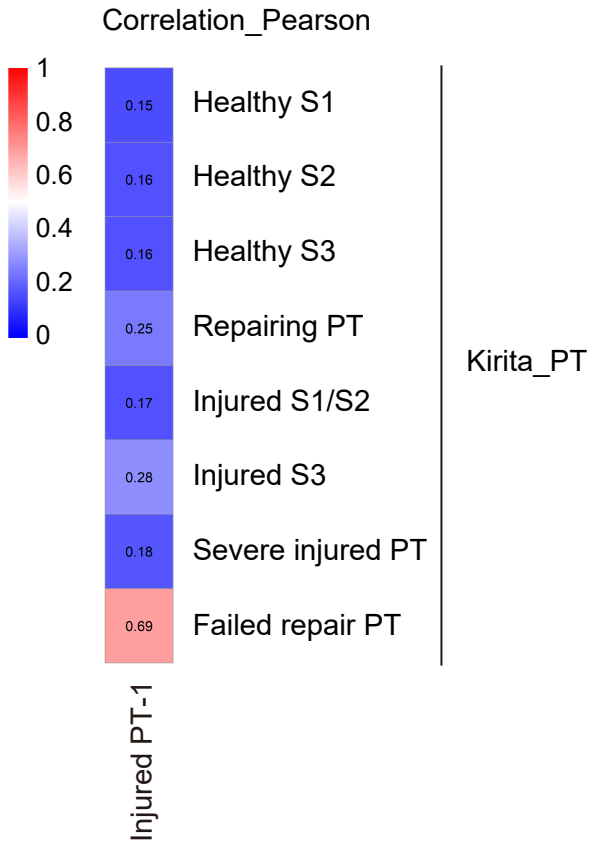
Supplemental Figure 8. Enrichment analysis of the reclustered PT clusters in the ischemia–reperfusion injury kidney dataset. (A, B) Enrichment analysis on the marker genes of (A) PT-S1/S2 and (B) PT-S2/S3 clusters in the PT subset in the integrated ischemia–reperfusion injury (IRI) kidney dataset was performed. Top six KEGG pathways and GO terms are shown in the bar graphs. Significance was expressed as $-\log_{10}(\text{adjusted } p\text{-value})$. PT, proximal tubule; S1/S2, S1 segment/S2 segment; S2/S3, S2 segment/S3 segment

Supplemental Figure 9



Supplemental Figure 9. Expression patterns of the genes encoding ligands highly expressed in the injured PT-1. Dot plots showing expression patterns of the genes encoding ligands highly expressed in injured PT-1 across the four PT clusters in the ischemia–reperfusion injury kidney dataset. Expression patterns of the genes that are shown in red characters are also shown in the violin plots in Figure 2C.

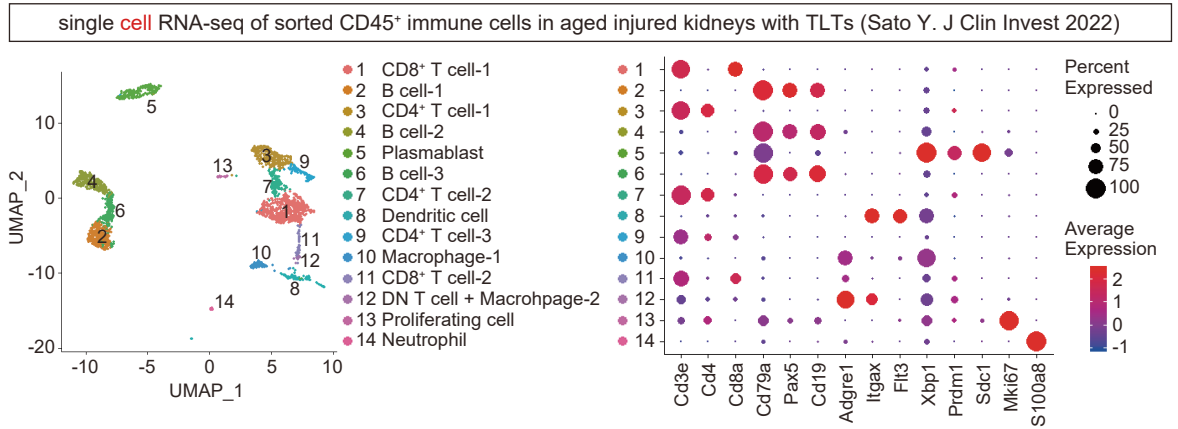
Supplemental Figure 10



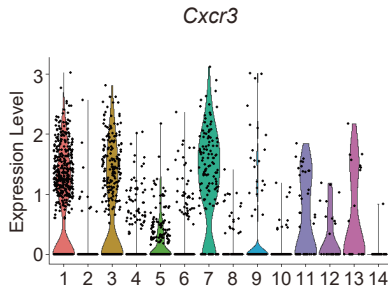
Supplemental Figure 10. Pearson correlation analysis between the injured PT-1 in our analysis and PT subpopulations in previous publication. The heatmap showed Pearson correlation coefficient calculated between injured PT-1 and seven PT subpopulations in previous publication by Kirita et al.⁴ (Kirita_PT), based on the average expression profiles of marker genes for PT subpopulations in our data. Injured PT-1 in our data was shown to be the most similar to “Failed repair PT” in Kirita_PT. PT, proximal tubule; S1, S1 segment; S2, S2 segment; S3, S3 segment

Supplemental Figure 11

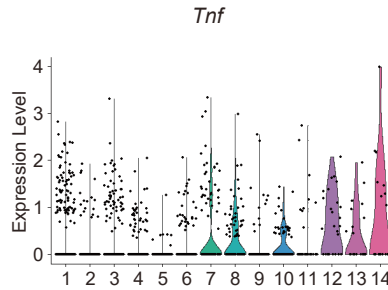
A



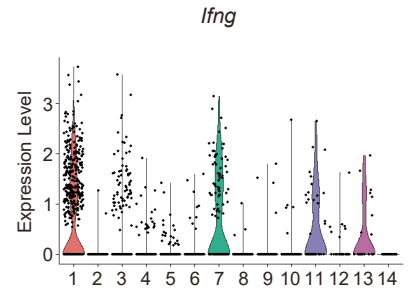
B



C

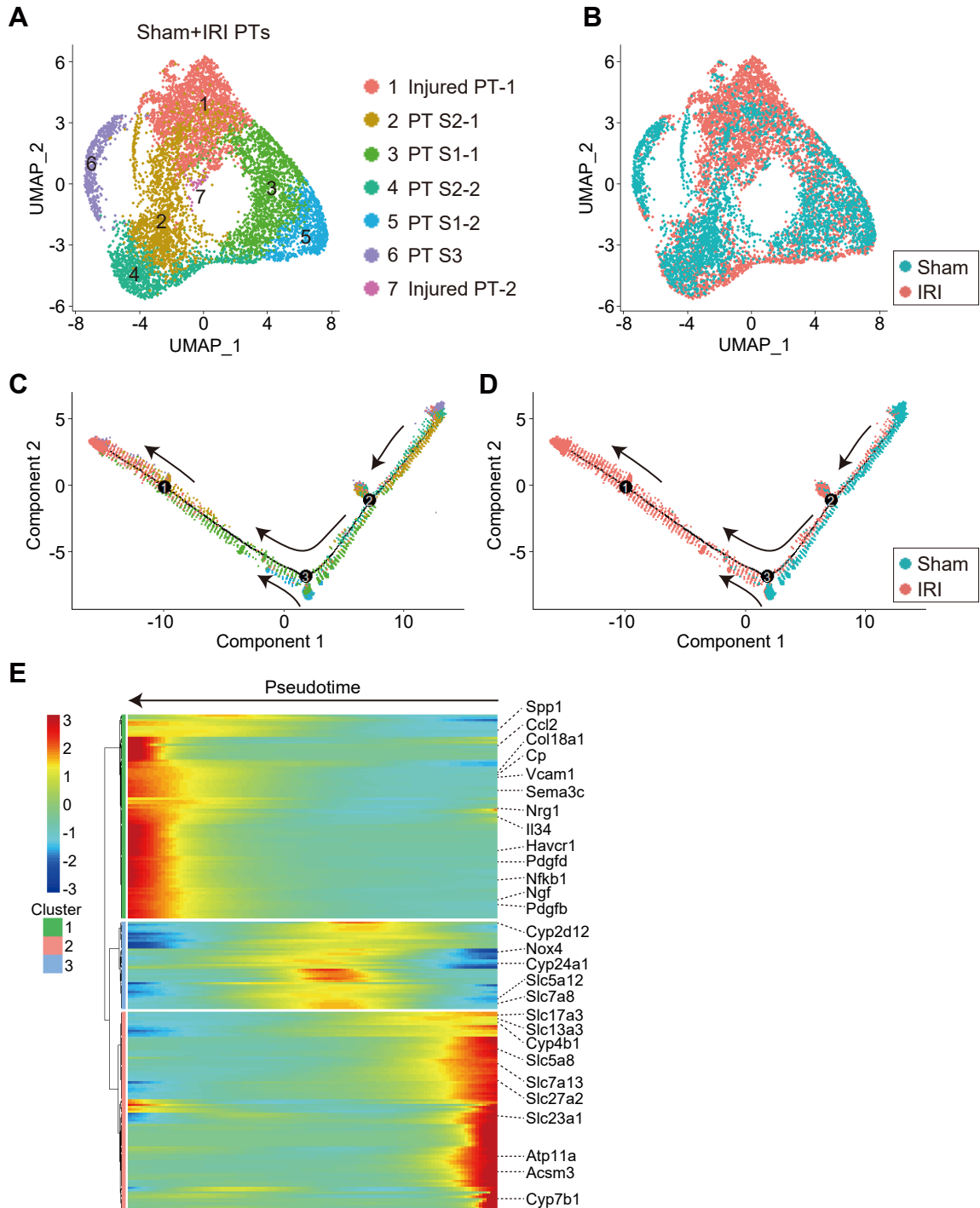


D



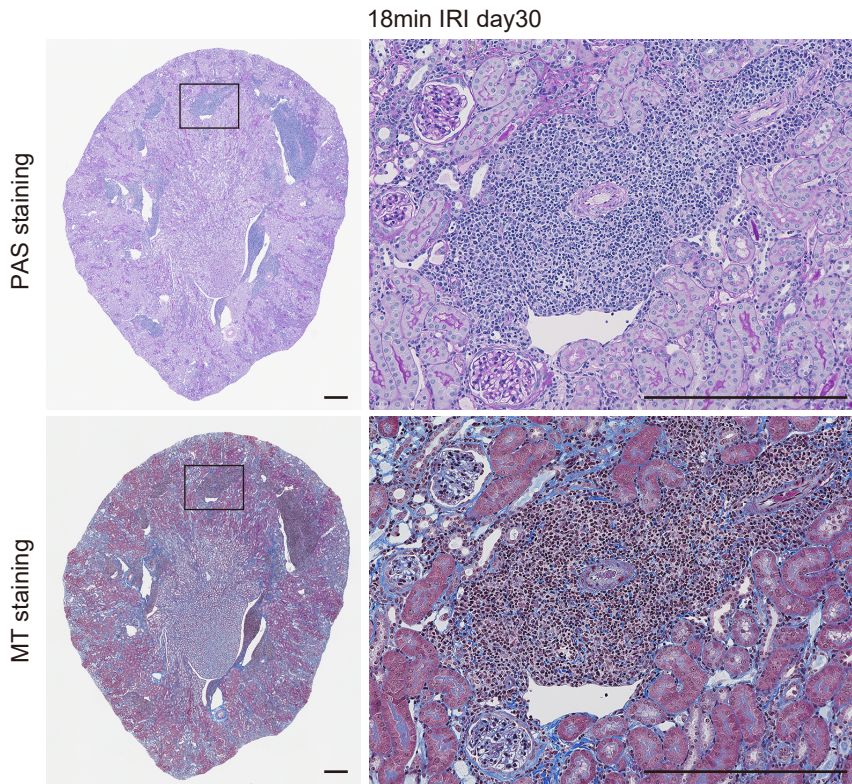
Supplemental Figure 11. Expression patterns of *Cxcr3*, *Tnf*, and *Ifng* in immune cells in aged injured kidneys with TLTs based on scRNA-seq dataset. (A) Uniform Manifold Approximation and Projection (UMAP) plots displaying the clustering of the sorted CD45⁺ immune cells in aged injured kidneys with TLTs and dot plots displaying expression patterns of the representative marker genes for each cluster based on scRNA-seq dataset that we previously reported.² (B–D) Violin plots showing gene expression patterns of (B) *Cxcr3*, (C) *Tnf*, and (D) *Ifng* in immune cells in the aged injured kidneys with TLTs detected by scRNA-seq dataset.² DN double negative

Supplemental Figure 12



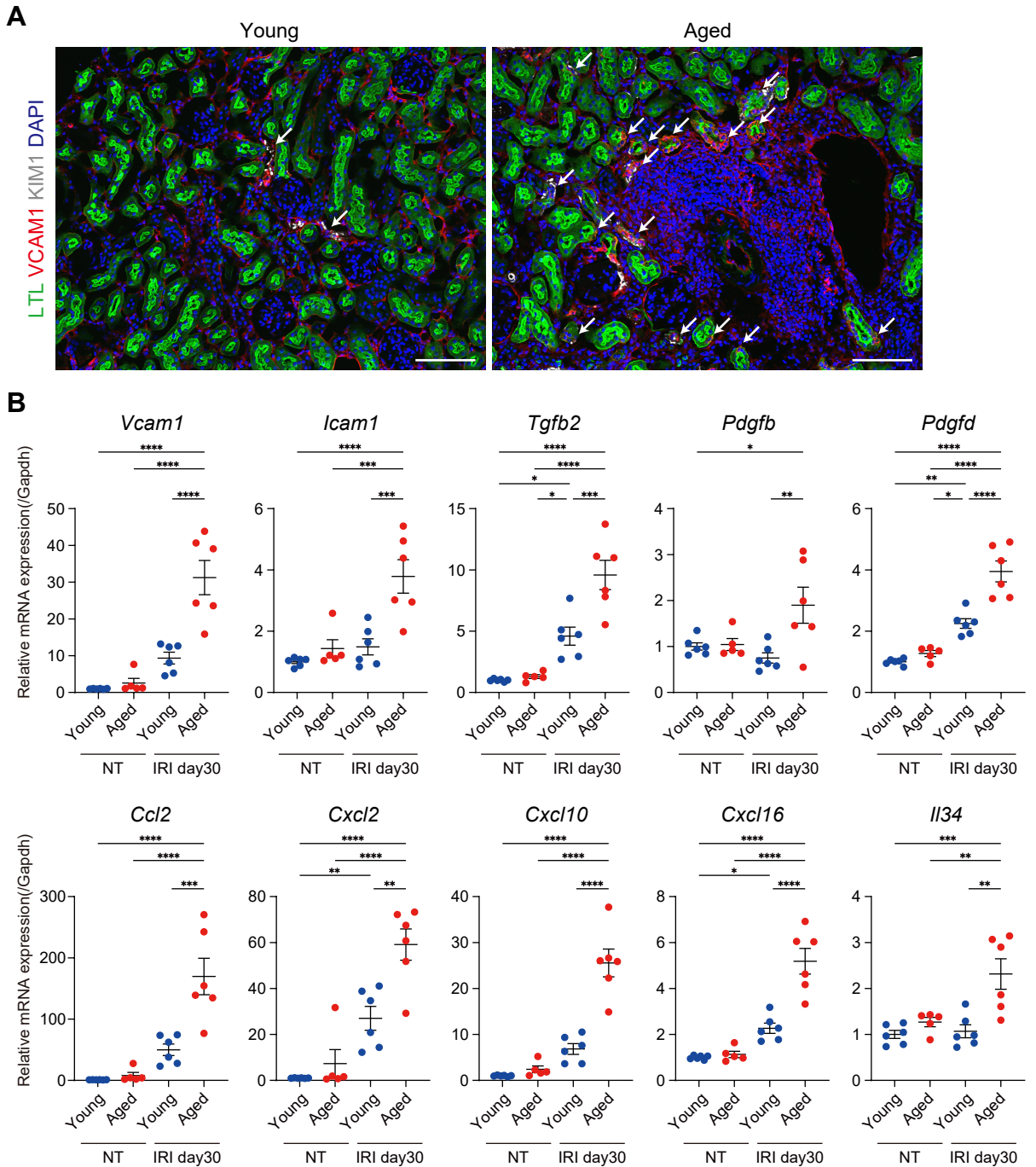
Supplemental Figure 12. Trajectory analysis of PT subsets. (A) Uniform Manifold Approximation and Projection (UMAP) plots showed that the integrated data of PT subsets in sham-treated and ischemia–reperfusion injury (IRI) kidney datasets was classified into seven clusters. (B) The UMAP plots were colored by sample types, sham (blue dots) and IRI (red dots). (C) Pseudotime trajectory analysis was performed on the integrated PT dataset using Monocle2. (D) The trajectory plots were colored by sample types, sham (blue dots) and IRI (red dots). (E) A heatmap showing gene expression changes of the representative marker genes for PT subpopulations, demonstrating that injured PT marker genes were upregulated with the downregulation of healthy PT marker genes along pseudotime.

Supplemental Figure 13



Supplemental Figure 13. Histology of aged injured kidneys 30 days after 18-minute mild ischemia–reperfusion injury. Periodic acid–Schiff (PAS) staining and Masson–Trichrome (MT) staining of murine kidneys 30 days after 18-minute mild ischemia–reperfusion injury (IRI). The right panels show the magnified images for the regions enclosed by rectangles in the left panels. Scale bars = 300 μ m.

Supplemental Figure 14

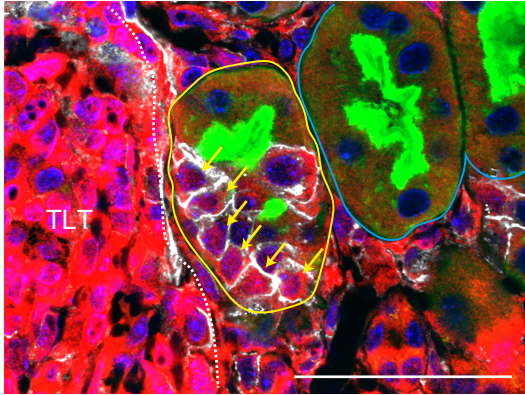


Supplemental Figure 14. Comparison of the expression of injured PT markers between aged and young injured kidneys. (A) Representative immunofluorescence images of LTL (green), VCAM1 (red), KIM1 (gray), and DAPI (blue) in young and aged injured kidneys 30 days after 18-min ischemia–reperfusion injury (IRI). VCAM1⁺ injured PTs (arrows) were more abundant in aged kidneys than young kidneys. Interstitial cells also expressed VCAM1. Scale bars = 100 μ m. (B) Results of quantitative real-time PCR for young and aged non-treated (NT) kidneys and injured kidneys 30 days after 18-min IRI (n = 5–6/group). Relative mRNA expressions of injured PT markers were shown. The expression levels were normalized to those of *Gapdh*. Values were shown as mean \pm standard error (SE). Statistical significance was determined using a one-way analysis of variance (ANOVA) followed by the Tukey–Kramer post-hoc test (* p < 0.05, ** p < 0.01, *** p < 0.001, and **** p < 0.0001).

Supplemental Figure 15

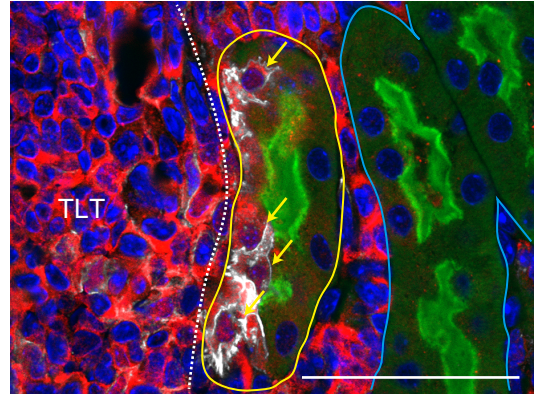
A

LTL p105/p50 VCAM1 DAPI



B

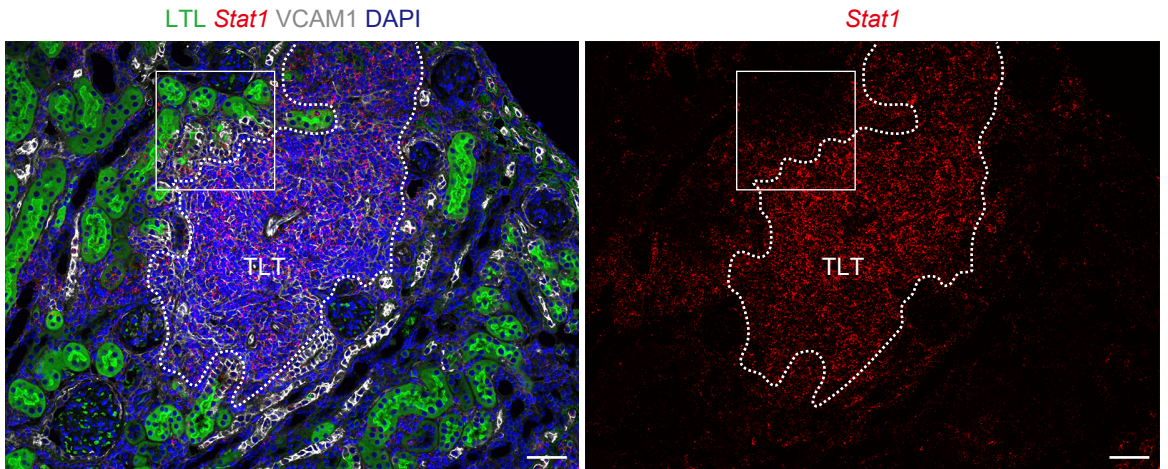
LTL STAT1 VCAM1 DAPI



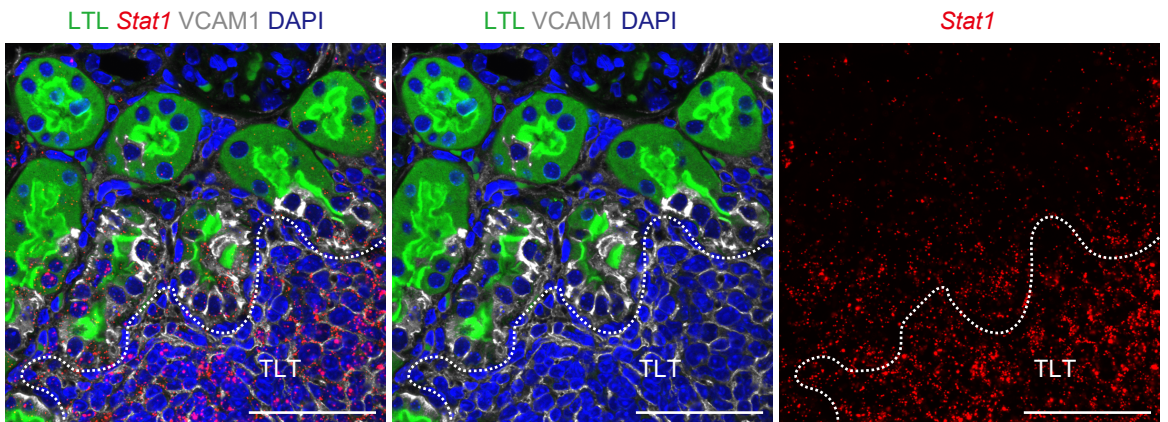
Supplemental Figure 15. Immunofluorescence images for transcription factors, p65 and STAT1, in aged injured kidneys with TLTs. (A, B) Immunofluorescence images of LTL (green), (A) p105/p50 (red), (B) STAT1 (red), VCAM1 (gray), and DAPI (blue) in the mild IRI kidneys. The VCAM1⁺ injured PT cells with upregulated expressions of p105/p50 and STAT1 adjacent to TLTs are shown by yellow arrows. The VCAM1⁺ PTs and VCAM1⁻ PTs are enclosed by yellow and light blue solid lines, respectively. TLT borders are shown as white dashed lines. Scale bars = 50 μ m.

Supplemental Figure 16

A

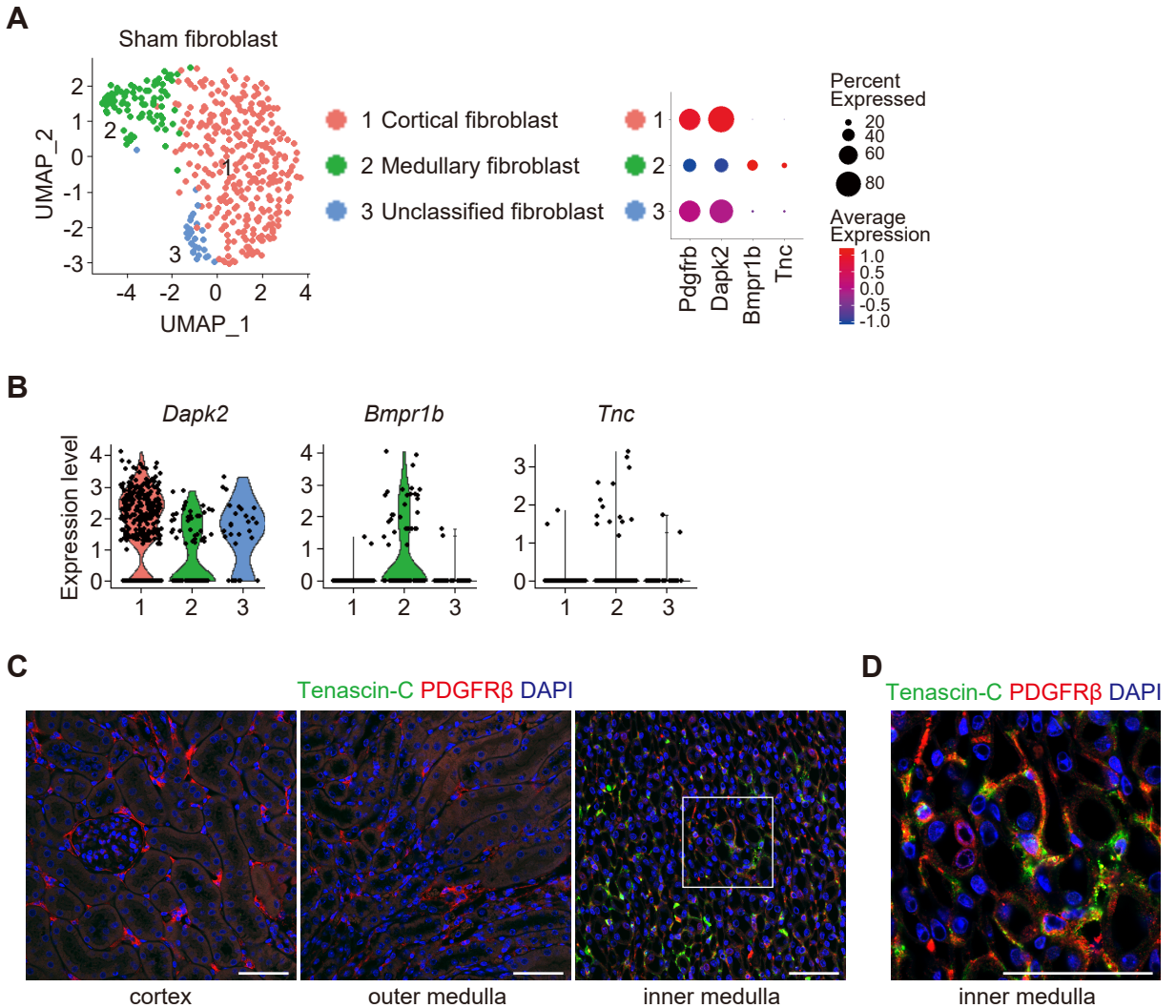


B



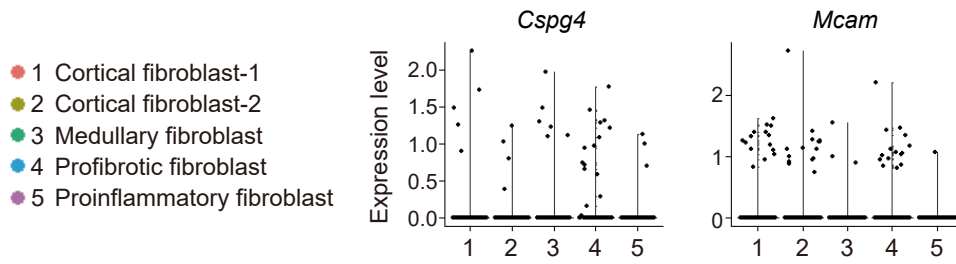
Supplemental Figure 16. *In situ* hybridization images showing high *Stat1* expression within TLTs and their surroundings. (A, B) A combination of *in situ* hybridization (*Stat1* [red]) and immunofluorescence (LTL [green], VCAM1 [gray], and DAPI [blue]) displayed high *Stat1* expression within TLTs as well as in VCAM1⁺ injured PT cells adjacent to TLTs (A) in low magnification. The area enclosed by squares in (A) are magnified in (B). Scale bars = 50 μ m.

Supplemental Figure 17



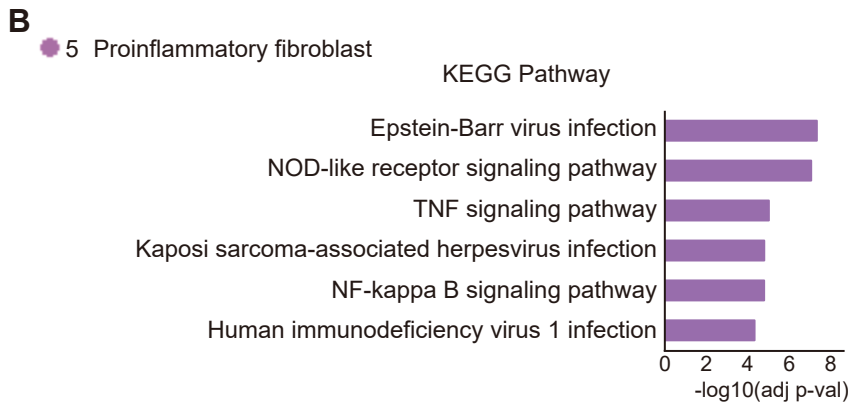
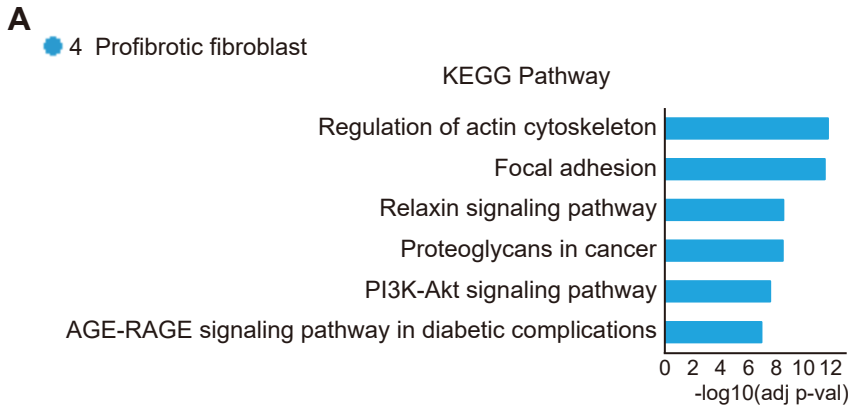
Supplemental Figure 17. Analysis of fibroblasts in the sham-treated kidney. (A) Uniform Manifold Approximation and Projection (UMAP) plots displaying reclustered fibroblast clusters in the sham-treated kidney and dot plots showing expression patterns of the selected marker genes for each cluster. (B) Violin plots showing the expression of the selected marker genes (*Dapk2*, *Bmpr1b*, and *Tnc*) across three fibroblast clusters. (C, D) Immunofluorescence staining of Tenascin-C (green), PDGFR β (red), and DAPI (blue) in the cortex, outer medulla, and inner medulla of the sham-treated kidney. Tenascin-C was stained in the PDGFR β ⁺ fibroblasts in the inner medulla in the sham-treated kidney (C). The area enclosed by a square in (C) is magnified in (D). Scale bars = 50 μ m.

Supplemental Figure 18



Supplemental Figure 18. Expression levels of pericyte markers across fibroblast subpopulations in the ischemia–reperfusion injury kidney dataset. The violin plots showed that gene expression of pericyte markers such as *Cspg4* and *Mcam* (encoding NG2 and CD146, respectively) was scarce across all clusters.

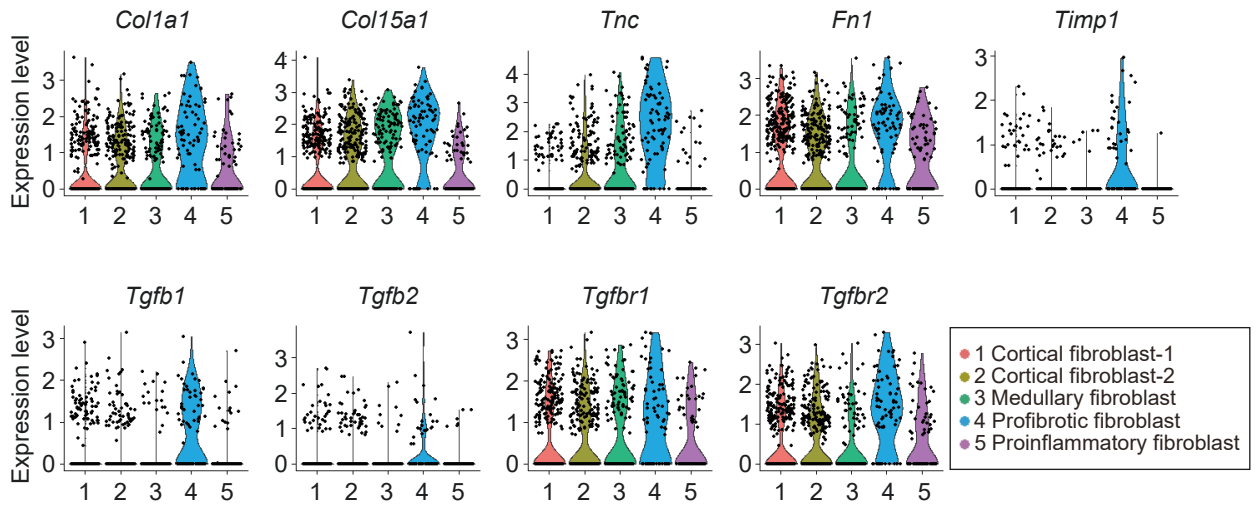
Supplemental Figure 19



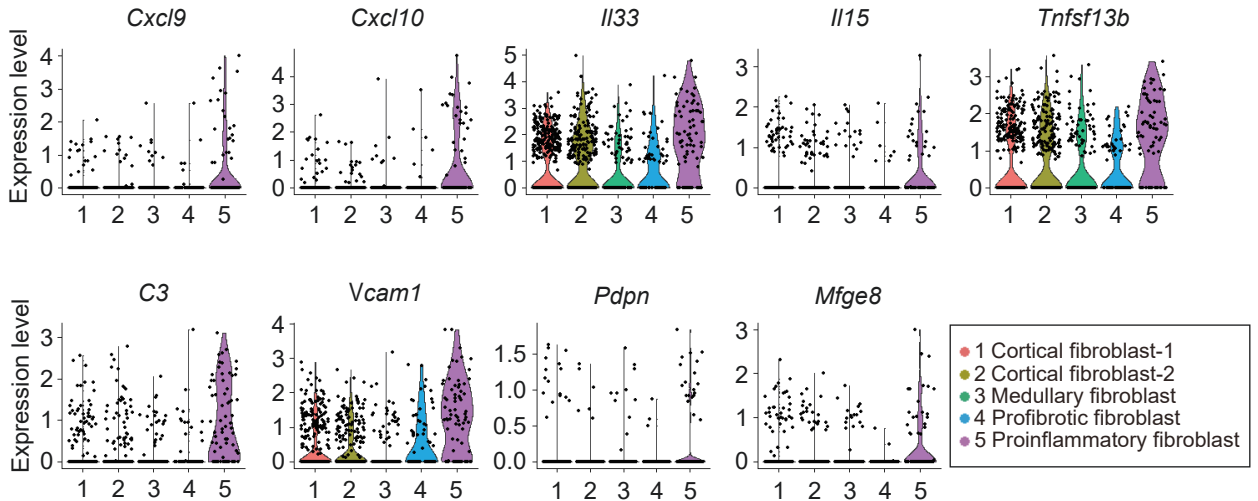
Supplemental Figure 19. KEGG pathways enriched in the fibroblast subpopulations in aged injured kidneys. (A, B) Top six KEGG pathways significantly enriched in the profibrotic (cluster 4 in Figure 5A) and proinflammatory (cluster 5 in Figure 5A) fibroblast cluster in aged injured kidneys. Significance was shown as $-\log_{10}(\text{adjusted } p\text{-value})$.

Supplemental Figure 20

A



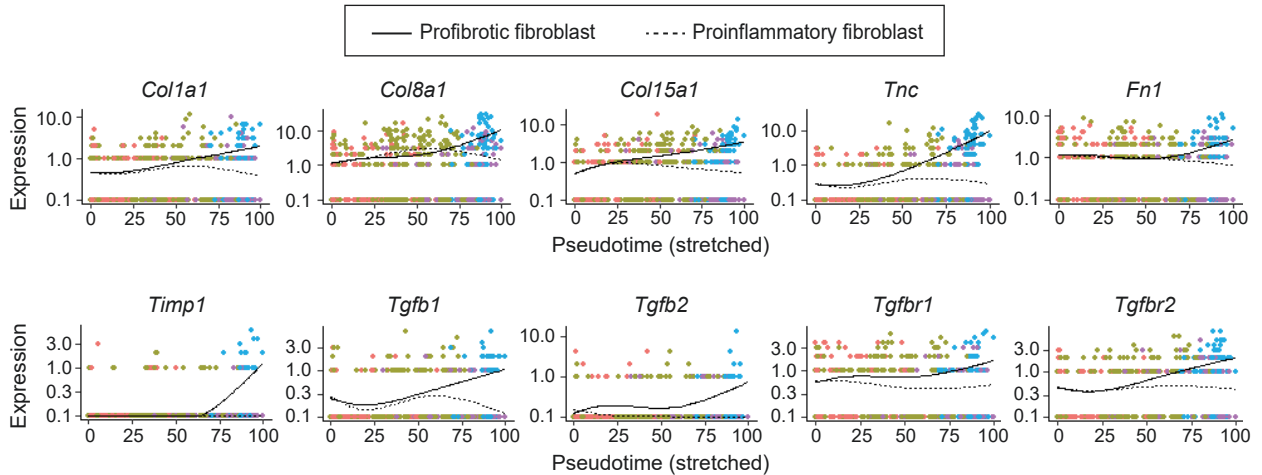
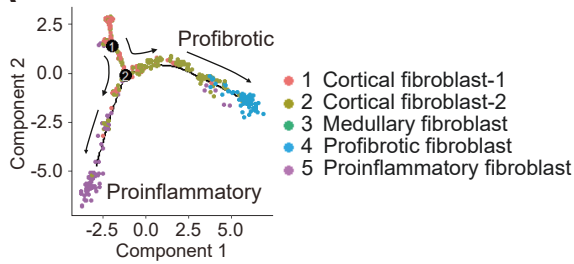
B



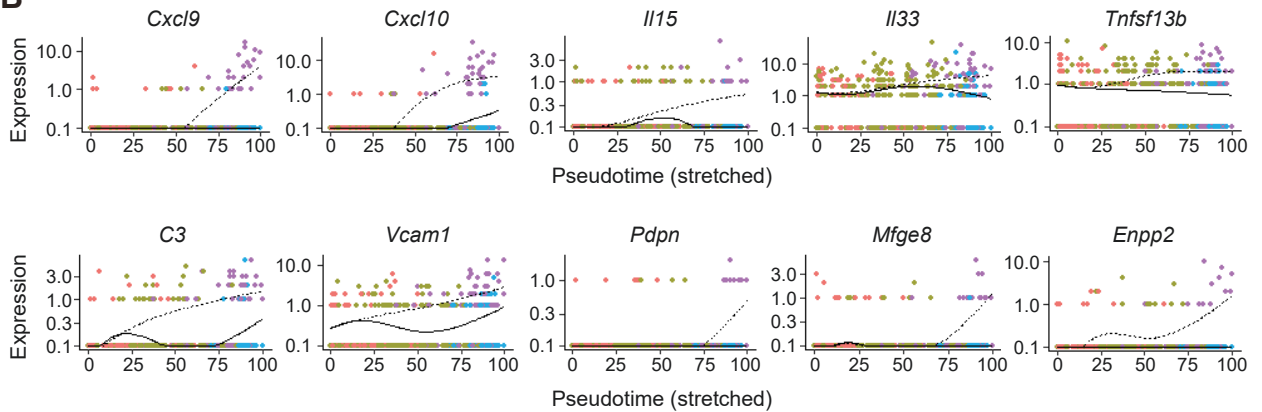
Supplemental Figure 20. Expression patterns of selected marker genes from the profibrotic and proinflammatory fibroblasts in aged injured kidneys. (A, B) Violin plots displaying expression patterns of the selected marker genes from the (A) profibrotic and (B) proinflammatory fibroblasts across the five fibroblast clusters in aged injured kidneys.

Supplemental Figure 21

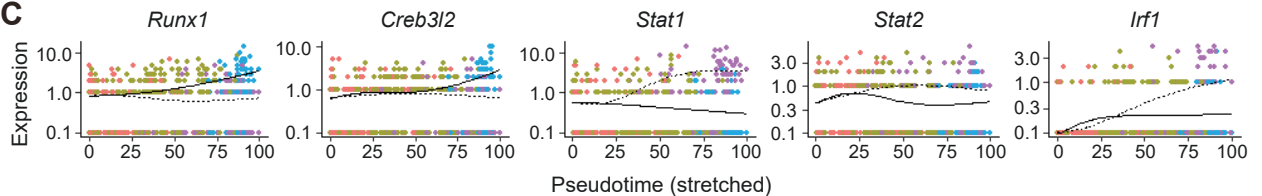
A



B



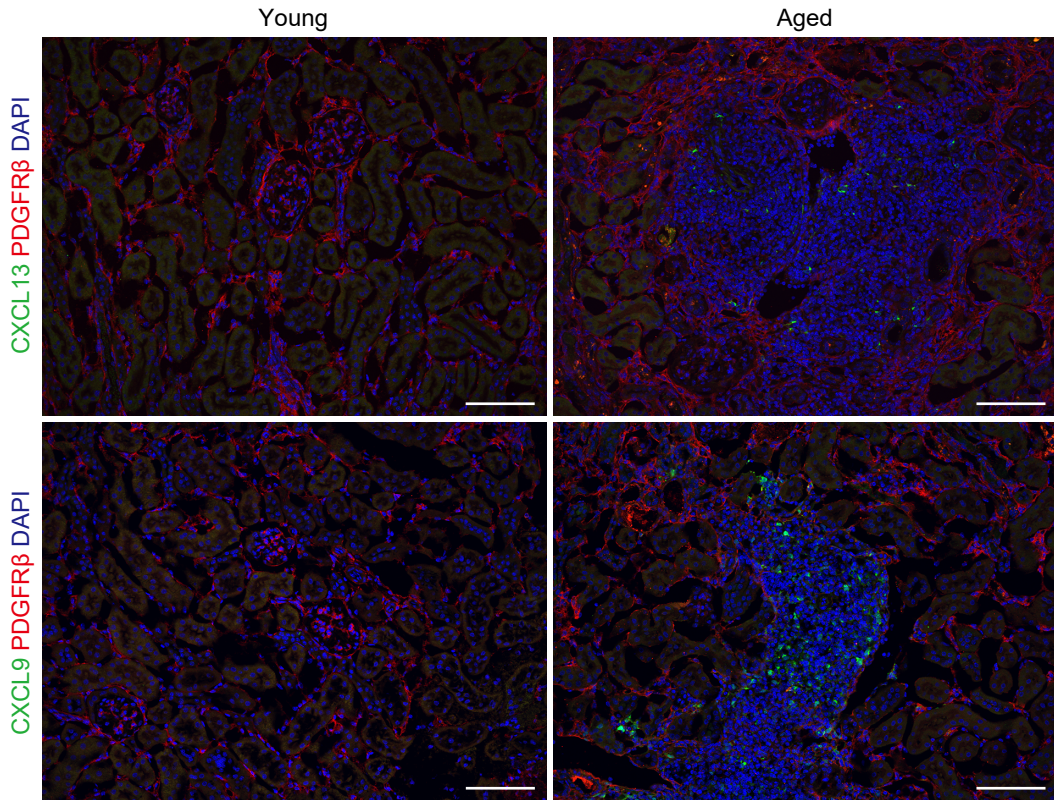
C



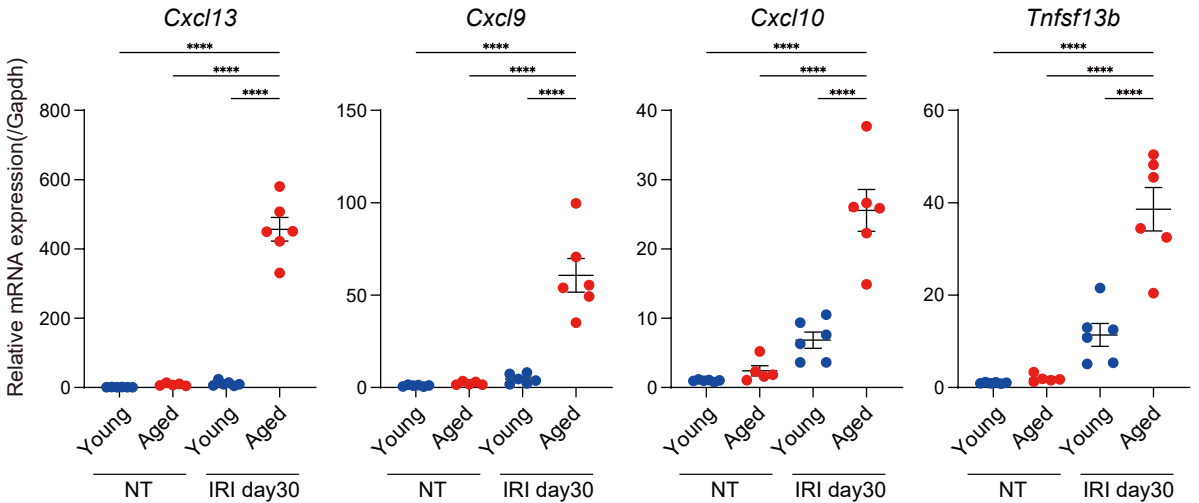
Supplemental Figure 21. Gene expression kinetics during fibroblast differentiation in aged injured kidneys was determined using pseudotime trajectory analysis. (A–C) The plots showing the gene expression level kinetics during renal fibroblast differentiation into profibrotic subtypes (solid lines) and into proinflammatory subtypes (dashed lines) along pseudotime from node number 2 in the trajectory plots in (A). The trajectory plots in (A) is the same as the plots in Figure 5G. The gene expression kinetics of (A) marker genes for the profibrotic fibroblasts, (B) marker genes for the proinflammatory fibroblasts, and (C) transcription factors activated in each fibroblast cluster are displayed.

Supplemental Figure 22

A



B



Supplemental Figure 22. Comparison of the expression of proinflammatory fibroblast markers between aged and young injured kidneys. (A) Representative immunofluorescence images staining for CXCL13 (green), CXCL9 (green), PDGFR β (red), and DAPI (blue) showed more abundant expression of these chemokines in the aged injured kidneys with TLTs 30 days after 18-min ischemia–reperfusion injury (IRI). Scale bars = 100 μ m. (B) Results of quantitative real-time PCR for young and aged non-treated (NT) and injured kidneys ($n = 5\text{--}6/\text{group}$). Relative mRNA expressions of chemokines and cytokines expressed by the proinflammatory fibroblasts were shown. The expression levels were normalized to those of *Gapdh*. Values were shown as mean \pm standard error (SE). Statistical significance was determined using a one-way analysis of variance (ANOVA) followed by the Tukey–Kramer post-hoc test (**** $p < 0.0001$).

References for Supplemental Information

1. Sato Y, Mii A, Hamazaki Y, Fujita H, Nakata H, Masuda K, et al.: Heterogeneous fibroblasts underlie age-dependent tertiary lymphoid tissues in the kidney. *JCI Insight* 1: e87680, 2016 doi: 10.1172/jci.insight.87680
2. Sato Y, Oguchi A, Fukushima Y, Masuda K, Toriu N, Taniguchi K, et al.: CD153/CD30 signaling promotes age-dependent tertiary lymphoid tissue expansion and kidney injury. *J Clin Invest* 132: e14607, 2022 doi:10.1172/JCI146071
3. Concordet JP, Hacussler M: CRISPOR: Intuitive guide selection for CRISPR/Cas9 genome editing experiments and screens. *Nucleic Acids Res* 46: W242-W245, 2018 doi:10.1093/nar/gky354
4. Kirita Y, Wu H, Uchimura K, Wilson PC, Humphreys BD: Cell profiling of mouse acute kidney injury reveals conserved cellular responses to injury. *Proc Natl Acad Sci U S A* 117: 15874–15883, 2020 doi: 10.1073/pnas.2005477117